The Aksay segment of the northern Altyn Tagh fault: Tectonic geomorphology, landscape evolution, and Holocene slip rate

A.-S. Mériaux,[1,2] P. Tapponnier,[2] F. J. Ryerson,[1] Xu Xiwei,[3] G. King,[2] J. Van der Woerd,[1,4] R. C. Finkel,[1] Li Haibing,[5,6] M. W. Caffee,[1,7] Xu Zhiqin,[5] and Chen Wenbin[3]

Received 3 June 2004; revised 12 November 2004; accepted 26 January 2005; published 28 April 2005.

[1] Millennial slip rates have been determined for the Altyn Tagh fault (ATF) at three sites near Aksay (~94°E) in northeastern Tibet by dating fluvial channels and terrace riser offsets with radiocarbon and ^{10}Be-^{26}Al surface exposure dating. Up to nine main surfaces are defined on the basis of morphology, elevation, and dating. The abandonment age of some surfaces is constrained by radiocarbon dating, which typically coincides with the youngest cosmogenic ages for a particular surface. Older surface exposure ages are taken to represent the duration of terrace emplacement. Cumulative offsets range from 20 to 260 m and fall in distinct groups, indicative of climatically modulated regional landscape formation. Most samples are younger than ~14 ka and postdate the Last Glacial Maximum. The end of the early Holocene optimum marks the boundary between the ages of the two main terrace levels at 5–6 ka. At this longitude the ATF is divided into a northern and southern branch. The northern ATF should thus yield a minimum rate for the ATF system. Slip rate estimates using the abandonment age of the overlying level for fill terraces or channels and the emplacement of the underlying level for strath terraces give 30 consistent results, yielding an average Holocene rate of 17.8 ± 3.6 mm/yr. It is ~9 mm/yr less than the long-term rate obtained near Tura at ~87°E (26.9 ± 6.9 mm/yr), in keeping with the inference of an eastward decreasing rate on the ATF, due to increased thrusting to the south. However, it remains twice the rate determined by GPS studies.

Citation: Mériaux, A.-S., et al. (2005), The Aksay segment of the northern Altyn Tagh fault: Tectonic geomorphology, landscape evolution, and Holocene slip rate, *J. Geophys. Res.*, *110*, B04404, doi:10.1029/2004JB003210.

1. Introduction

[2] Two disparate rheological models have been used to conceptualize the nature of ongoing deformation associated with the Indo-Asian collision. At one extreme both the viscous crust and lithospheric mantle deform and thicken homogeneously across broad regions [*England and Houseman*, 1986; *Holt*, 2000; *Holt et al.*, 2000] and strike-slip faulting is a minor and late consequence of the resulting gravitational flow away from maximum relief [*England and Molnar*, 1997a, 1997b; *Houseman and England*, 1986]. At the other extreme deformation is localized along the boundaries of lithospheric or crustal blocks that deform elastically on the long term [*Meyer et al.*, 1998; *Roger et al.*, 2000; *Tapponnier et al.*, 1990, 2001a, 2001b]. These opposing viewpoints lead to contrasting predictions on the current Indo-Asian velocity field, especially with respect to the role of strike-slip faulting along the boundaries of the Tibetan Plateau.

[3] Deformation of a fluid continental lithosphere predicts low slip rates (mm/yr) distributed among numerous faults [e.g., *England and Molnar*, 1997a; *Holt*, 2000; *Holt et al.*, 2000]. Conversely, localization of strain within the lithosphere predicts high slip rates (cm/yr) along a few large "lithospheric fault" zones such as the Altyn Tagh, Kunlun, Haiyuan, and Karakorum strike-slip faults [*Avouac and Tapponnier*, 1993b; *Peltzer and Saucier*, 1996]. As such, slip rate determinations on the major active faults of Asia can provide important information on the more general problem of the rheology of the continental lithosphere. As illustrated by recent discrepancies between decadal and millennial slip rates [*Bendick et al.*, 2000; *Mériaux et al.*, 2004; *Peltzer et al.*, 2001], assessing slip rates on faults is not a simple task and can be influenced by both the choice of analytical method (geodetic versus morphochronologic),

[1]Lawrence Livermore National Laboratory, Livermore, California, USA.
[2]Laboratoire de Tectonique, Mécanique de la Lithosphère, Institut de Physique du Globe de Paris, CNRS-UMR 7578, Paris, France.
[3]Institute of Geology, China Earthquake Administration, Beijing, China.
[4]Now at Institut de Physique du Globe de Strasbourg, CNRS-UMR 7516, Strasbourg, France.
[5]Institute of Geology, Ministry of Land and Resources, Beijing, China.
[6]Now at Total Exploration China, Total-Fina-Elf, Beijing, China.
[7]Now at Physics Department, Purdue University, West Lafayette, Indiana, USA.

0148-0227/05/2004JB003210$09.00

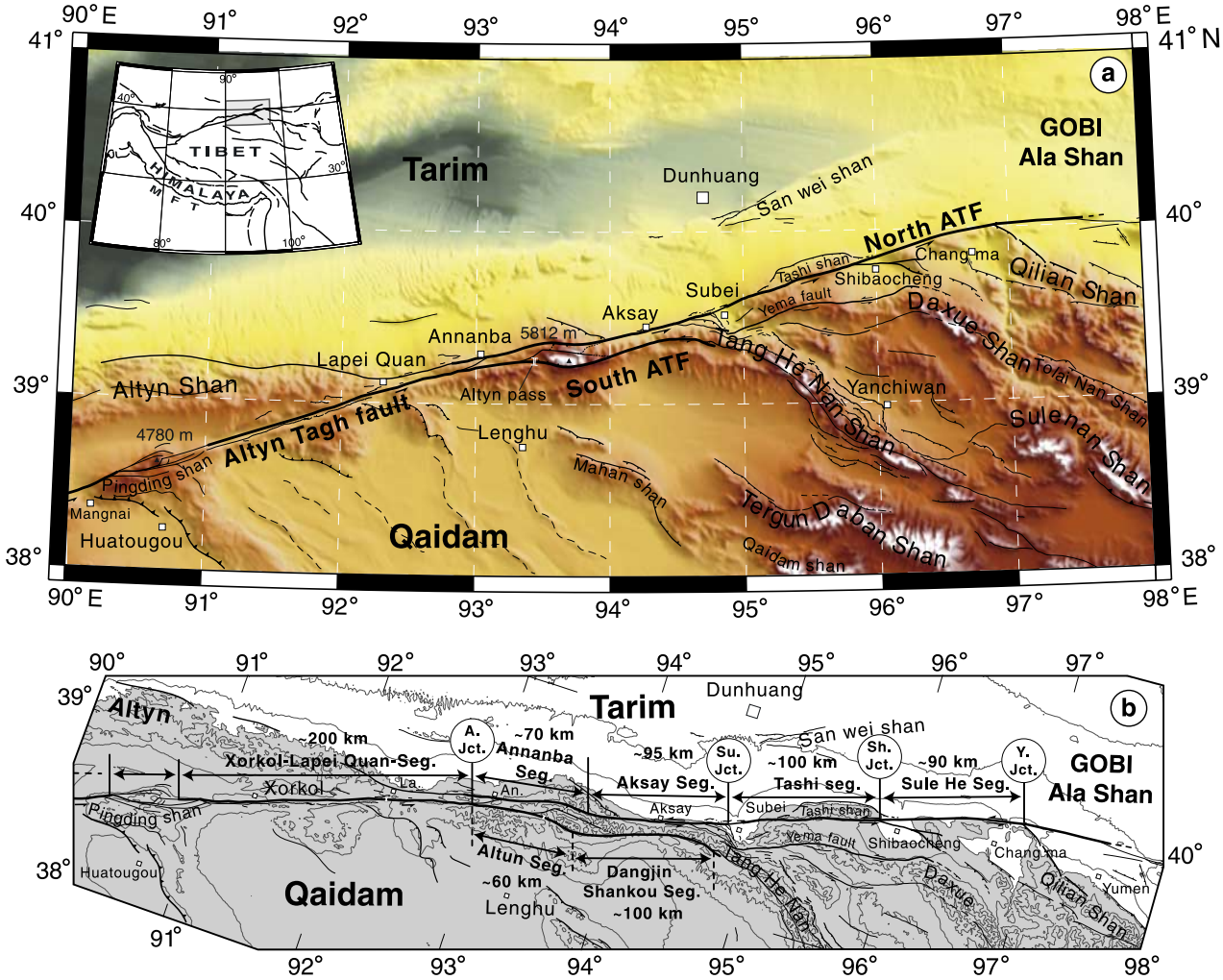

Figure 1. Neotectonic map of northern Tibet. (a) Topography and active faulting along the eastern Altyn Tagh fault system (modified from *Meyer et al.* [1998], *Tapponnier et al.* [1990], and *Van der Woerd et al.* [2001]). (b) First-order segmentation and main junctions of ATF system from Pingding Shan to Qilian Shan. A. Jct, Annanba junction; Su. Jct, Subei junction; Sh. Jct, Shibaocheng junction; and Y. Jct, Yumen junction.

the observation interval (decadal versus millennial) as well as the largely unexplored potential for variations in slip rate with time. In this connection, comparison with geologic slip rate determinations is even more speculative as rates may vary because of the large-scale fault evolution and growth [e.g., *Hubert-Ferrari et al.*, 2003; *Métivier et al.*, 1998; *Meyer et al.*, 1998].

[4] The importance of localized deformation along active strike-slip faults in accommodating Indo-Asian convergence is best illustrated by the Altyn Tagh fault system (ATF). The 2500-km-long Altyn Tagh fault system [*Tapponnier and Molnar*, 1977] follows the northern edge of the Tibetan Plateau from Muztagh Ata Tagh, near 75°E, to Yabraishan, east of 102°E (Figure 1a, inset). This left-lateral strike-slip fault zone has been interpreted to guide the northeastward extrusion of Tibet relative to the Tarim basin, with hundreds of kilometers of motion in the Tertiary [*Peltzer and Tapponnier*, 1988; *Ritts and Biffi*, 2000; *Ding et al.*, 2004]. Seismic tomography suggests that a deep shear zone extends beneath the fault to the base of the lithosphere [*Wittlinger et al.*, 1998, 2004], but the magnitude of the slip rate along the fault remains controversial [*Peltzer et al.*, 1989; *Ge et al.*, 1992; *Bendick et al.*, 2000; *Washburn et al.*, 2001, 2003; *Mériaux et al.*, 2004]. In this paper, we determine a millennial slip rate on the northeastern stretch of the Altyn Tagh fault, near Aksay (39°N, 94°E) on the basis of radiocarbon (^{14}C), and ^{10}Be and ^{26}A1 in situ cosmogenic dating of alluvial fans and fluvial terraces offset by the fault.

2. Geometry and Segmentation of the Eastern Altyn Tagh Fault Between the Altyn and Qilian Shan

[5] From 90°E to 97°E, the eastern stretch of the Altyn Tagh fault strikes N70°E overall, but has a complex geometry (Figure 1). Between the western edge of the Qaidam basin and the Qilian range, the fault system comprises three principal parallel strands [*Peltzer et al.*, 1989; *Ge et al.*, 1992; *Meyer et al.*, 1998; *Van der Woerd et*

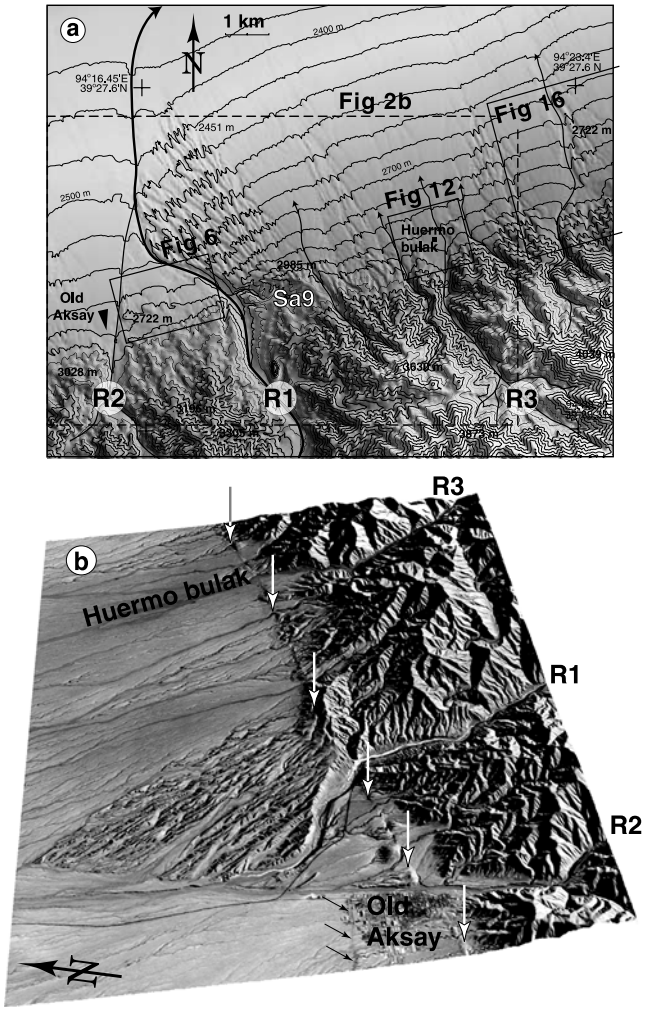

Figure 2. Northern Dangjin Shankou piedmont near Aksay. (a) Topographic contour map of DEM obtained from digitized 1/50,000 topographic map of Aksay region. (b) SPOT image (KJ: 235–271) draped over DEM.

al., 2001]. The southern strand or South Altyn Tagh fault (SATF) follows the Qaidam side of the Altyn push-up and then veers southeastward into the Tanghenan Shan. The northern strand follows the edge of the Tarim block from the Altyn to the Qilian Shan thrust fronts. East of the Qilian Shan front, the northern strand (NATF) continues with a N96°E strike north of the Hexi corridor. The central strand or Yema fault jogs southward from the NATF between Aksay and Subei and continues northeastward to the Taxue Shan thrust front.

[6] The three main strands branch off one another or merge with other faults at several consecutive triple junctions [*Meyer et al.*, 1998; *Van der Woerd et al.*, 2001] (Figure 1b). The Annanba junction, between the SATF and NATF, lies west of the Altyn push-up. The Subei junction is located near the particularly sharp, N130°E striking restraining thrust bend where the Tanghenan Shan meets the fault. Farther east, the N100°E striking Chang Ma fault splays at the Shibaocheng junction. Finally, the Yumen junction is the high-angle meeting point between the North Altyn Tagh fault and the N120°E striking Qilian range front thrust.

[7] The complexity of the fault system at this longitude appears to be intimately related to the ongoing growth of the youngest part of the Tibet plateau [*Meyer et al.*, 1998; *Tapponnier et al.*, 2001b; *Van der Woerd et al.*, 2001; *Métivier et al.*, 1998]. In this growth process, the fault progressively loses slip to the oblique thrusts that bound the major NW-SE trending mountain ranges south of the fault (Figure 1). Such complex geometry has consequences for seismic behavior and slip rates. Different slip rates are expected not only along the three principal branches, but also along segments separated by junctions. A stepwise, northeastward decrease of the slip rate is required at each thrust junction as lateral slip is transformed into horizontal shortening.

[8] On both the SATF and NATF, it is possible to identify several first-order segments, separated either by the junctions or by large restraining bends or extensional jogs [*Meyer et al.*, 1998; *Van der Woerd et al.*, 2001] (Figure 1b). From west to east, we divide the Southern Altyn Tagh fault, west of 90°30′E, into three principal segments. The 200-km-long Xorkol-Lapei Quan segment extends from the 4 km left step at the Pingding Shan pull-apart (see also [*Washburn et al.*, 2001]), to the Annanba junction (92°55′E). The Altyn segment stretches over a length of 60 km from that junction to about 93°35′E, midway along the southern front of the main southern Altyn push-up range. Next is the Dangjin Shankou segment which follows the southern edge of that range to the Tanghenan Shan pull-apart at 94°45′E, a distance of 100 km.

[9] Similarly, the northern ATF may be divided into four main segments (Figure 1b). The Annanba segment extends to about 93°40′E, midway along the northern front of the northern Altyn push-up range, a distance of 70 km. The next Aksay segment stretches 95 km from the asbestos mines of the Altyn Shan to the Tanghenan Shan thrust junction at Subei (94°45′E). The Tashi segment, between the Subei and Shibaocheng junctions (95°50′E), is ~100 km long. Finally, the Sule He segment, which follows the northern range front of Yingzui Shan between the Shibaocheng and Yumen junctions, is 90 km long.

[10] There are other active fault splays and minor pull-apart or push-up jogs along these first-order segments, but none that significantly disrupts the overall linearity of their traces. In particular, several oblique faults with significant normal slip components cut across the Pingding and Altyn push-up ranges (Figure 1b). Both ranges, whose summit peaks are 4790 and 5788 m high, respectively, appear to be former restraining jogs, now in the process of being dismembered by theses oblique normal faults that establish throughgoing connections between segments on opposite sides. Such second-order faults may break coevally with the main segments, thus marking the termination of large strike-slip event ruptures. Additionally, south of the Pingding range, of Xorkol Lake, of the Lapei Quan pass, and of the Altyn pass, oblique splays of both the NATF and SATF step southward and continue as NW-SE striking active thrusts into the Qaidam basin.

[11] The strongest segment boundaries, which we infer not to be crossed by large earthquake ruptures, are probably those at the Pingding and Altyn push-up bends and at the Tanghenan thrust junction near Subei. The last two correspond to paired segment boundaries on both the SATF and

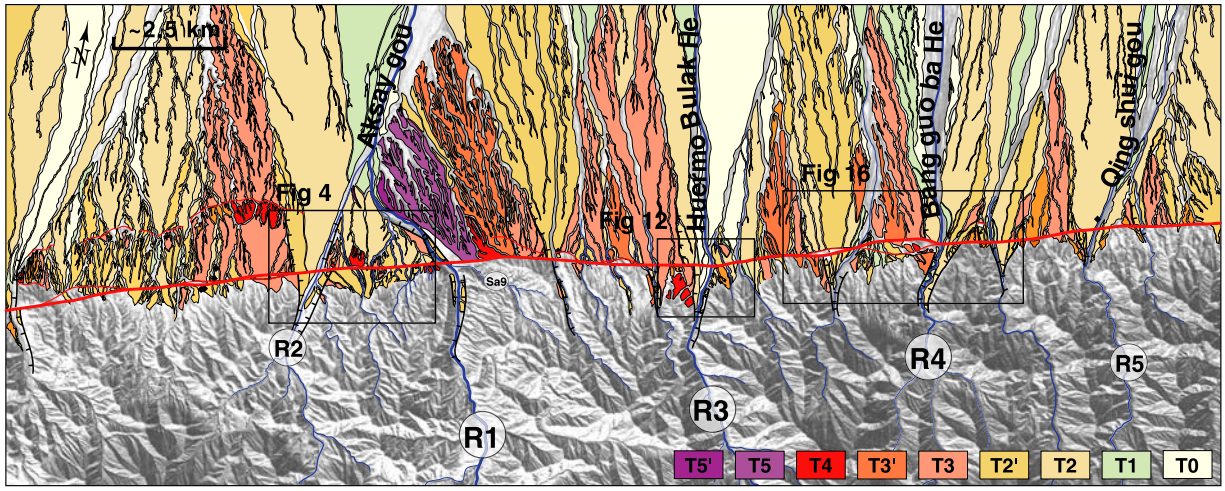

Figure 3. Geomorphic map of the northern Dangjin Shankou piedmont near Aksay overlaying unrectified Corona image (DISP 1024-1054DF048, scale is approximate). Relative positions are shown of the Aksay, Huermo Bulak, and Bang guo ba sites investigated here. Surface chronology is based on surface morphology, leveling, and age determinations in this study. The ^{14}C samples collected outside three sites are indicated by dark diamonds.

NATF (Figure 1). It is also just south of the Subei junction that the Yema fault meets with the Tanghenan thrusts. The Annanba junction, on the other hand, may not always act as rupture boundary. Large, comparably fresh mole tracks and sinistral offsets of 6–10 m similar to those seen at Gobiling [*Washburn et al.*, 2001] are in fact observed all the way from the Pingding Shan pull-apart to the Altyn pass, with a maximum of 12–14 m just east of that pass. North of the northern Altyn range, fresh mole tracks appear to stop just east of the big asbestos mine near 93°40′E. In contrast, mole tracks along either the NATF or SATF east of the Altyn push up are much more degraded and hence older. This suggests that a great earthquake ($M > 8$) could have ruptured both the Xorkol-Lapei Quan and Altyn segments of the SATF (cumulative length 265 km) and possibly also the 70 km Annanba segment of the NATF in the last few hundred years, while the Aksay and Dangjin Shankou segments on either fault branch would have been quiescent for longer times.

[12] In terms of their cumulative geomorphic signature in the field and hence qualitatively, their relative slip rates, a significant difference is clear on either side of the Altyn Shan push-up along the NATF and SATF. West of Annanba, the trace of the NATF is subdued. The same holds for the trace of the SATF east of the Altyn pass. Thus significant transfer of slip must occur from the South to the North Altyn Tagh fault across the Annanba junction and the Altyn push-up.

[13] Constraining the slip rates on each of the seven principal segments of the two faults, north of the Qaidam basin and Qilian ranges is a long-term endeavor. To begin, we have targeted the Aksay and Tashi segments of the NATF, and the Xorkol-Lapei Quan segment of the SATF, which are easily accessible. The Aksay segment, in particular, offers many opportunities to date cumulative offsets, and the sites discussed below are located along that segment, mostly east of old Aksay village and west of the Subei thrusts, on either side of the Dunhuang-Golmud road (Figures 1b, 2, and 3).

3. Geomorphology and Quaternary Geology of the Aksay Segment of NATF

[14] The Aksay segment of the fault hugs the northern edge of the Dangjin Shankou range (Figures 1–3). This range, with a basement composed mostly of Paleozoic metavolcanics and schists intruded by granites, rises to elevations above 4000 m but is below the present-day snow line. The metamorphic basement is usually in sharp fault contact with a narrow strip of deformed, steeply dipping Neogene red beds parallel to the active fault. The active fault dips 50° to 70° south and is marked by gouge zones meters to tens of meters wide. In section, it juxtaposes the Neogene sandstones with thick Quaternary fanglomerates that have accumulated in the foreland north of the range front. This huge apron of coalescent fans forms a foreland bajada that slopes northward to the dune fields ringing the Tarim basin. The bajada surface descends regularly from an elevation of 2700–2800 m to 1650 m over a distance of ~25 km (average slope 2.5°, Figures 2 and 3). Hence only half of the Dangjin Shan Kou range height rises above the debris that piled north of it.

[15] The active fault trace cuts the apexes of most of the imbricated fans forming the bajada (Figures 2 and 3). The relative ages of the fans increase as a function of height above the present streams beds and also correlate with the degree of incision by superficial seasonal rills (Figures 2 and 3). Loess and soil layers of variable thickness cover the

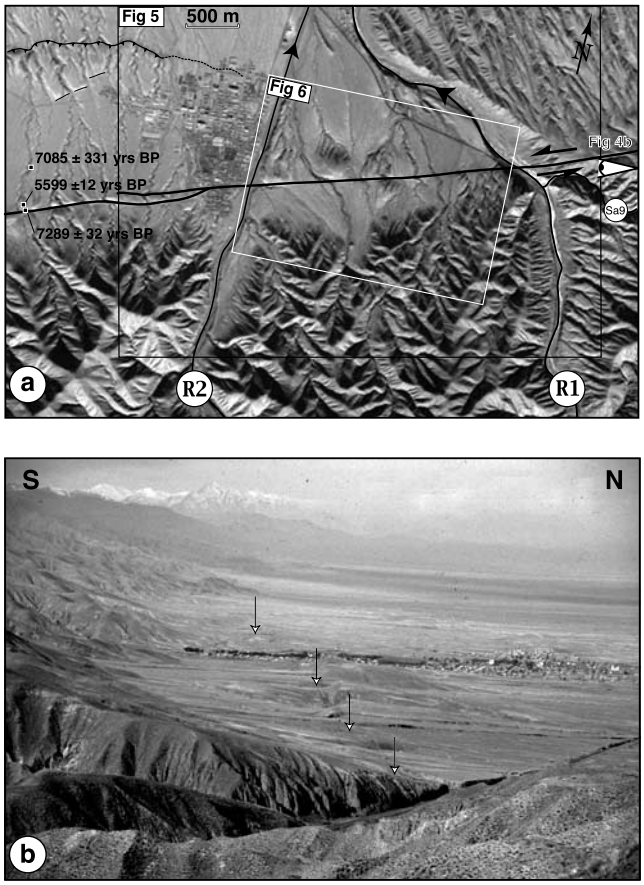

Figure 4. (a) SPOT image of Aksay city site. Locations of charcoal samples with calibrated ages, collected west of Old Aksay village, are indicated by dark squares. Boxes give locations of more detailed maps in Figures 5 and 6. Point of view of Figure 4b is indicated. (b) Northwest looking view of fault trace at Aksay city site.

ancient fans while the most recent ones have surfaces paved with cobbles and boulders. The catchments drained by the streams and rivers reaching the foreland are different. Fairly large, permanent rivers, spaced 3 to 5 km from one another reach deep into, or cross the range, and have probably been fed by glacial meltwater during periods of deglaciation [*Ballantyne*, 2002, and references within]. Other, more numerous but smaller streams are born on the range front slope, at elevations mostly below 3600 m (Figures 2 and 3). The map on Figure 3 summarizes the relative ages of the different terraces and fans within the bajada that are consistent with the geomorphic and geological criteria outlined above, and with our field mapping and surface dating, discussed below.

[16] Systematic sinistral offsets of alluvial fans, fluvial terraces, risers and channels are observed all along the fault whose principal trace is remarkably sharp and linear, with only a few kilometer long restraining or releasing swings. We selected three areas, all of them near the outlets of large rivers, to quantify the various amounts of cumulative offsets seen, and their ages: (1) Old Aksay, (2) Huermo Bulak and (3) Bang guo ba (Figure 3). In the following sections we first describe the terrace morphology, offsets and surface dating at each site, before turning to the general discussion of regional landscape evolution and slip rates.

3.1. Old Aksay

[17] The village of old Aksay (2700 m above sea level, Figures 4–6), now destroyed, lies on a bench uplifted by a small active thrust whose lobate trace runs along the base of a gentle flexure ~1.5 km north of the Altyn Tagh fault (Figures 3, 4, and 5). This thrust attests to the locally transpressive kinematics of the fault. For ~2.5 km, between the two principal, perennial tributaries of the Aksay He (R1, R2), the N73° striking fault trace, locally marked by seismic mole tracks, cuts across fans and terraces of different heights and ages. These fans and terraces have been emplaced by north flowing seasonal streams with small catchments (Sa1–Sa9) (Figures 4 and 6). Of all the streams and rivers, only the eastern Aksay river (R1) cuts across the Dangjin Shankou range (Figures 2 and 3). All the fluvial terraces and stream channels cut by the fault are left-laterally offset.

[18] In the field, using stereoscopic air photos, 1/50,000 scale topographic maps, rectified Corona and SPOT images (~3.3 and 10 m resolution, respectively), we mapped the channels, terrace surfaces and risers in detail SE of Aksay (Figure 6). On the basis of geomorphic characteristics, three groups of terraces may be distinguished (Figure 6). Older terraces (T4, T3) form isolated hills that stand above the average surface of the bajada and are deeply incised by closely spaced rills (Figures 6, 7, and 8). The main terraces (T2′, T2) form a broad, smooth and uniform surface that grades downstream into the bajada. The T2′ terrace level continues upstream and is present as isolated fluvial benches in the valleys of R1 and R2. Between these valleys, the T2′-T2 surface is at places mantled by small proximal fans. The T2′ conglomerates deposited by R2 fan out where the river flows out of the range (Figures 3–5). It is on that triangular-shaped fan, bounded to the west by a well-defined riser that the old village of Aksay was built

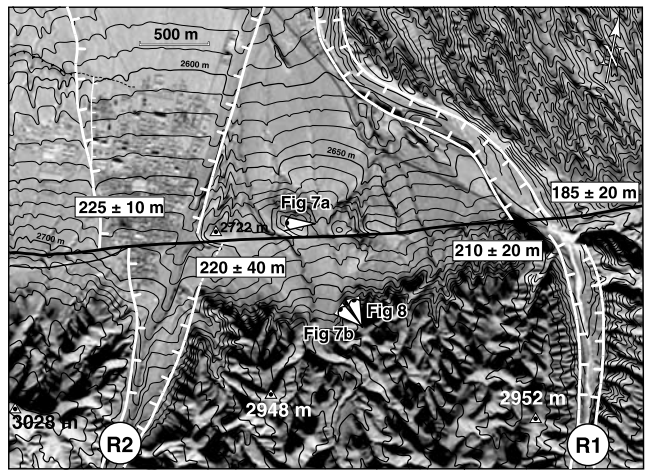

Figure 5. Topographic contour map of Aksay displayed over SPOT image. Largest left-lateral offsets at Aksay occur along the banks of rivers R1 and R2. Point of views of Figures 7a, 7b, and 8 are indicated.

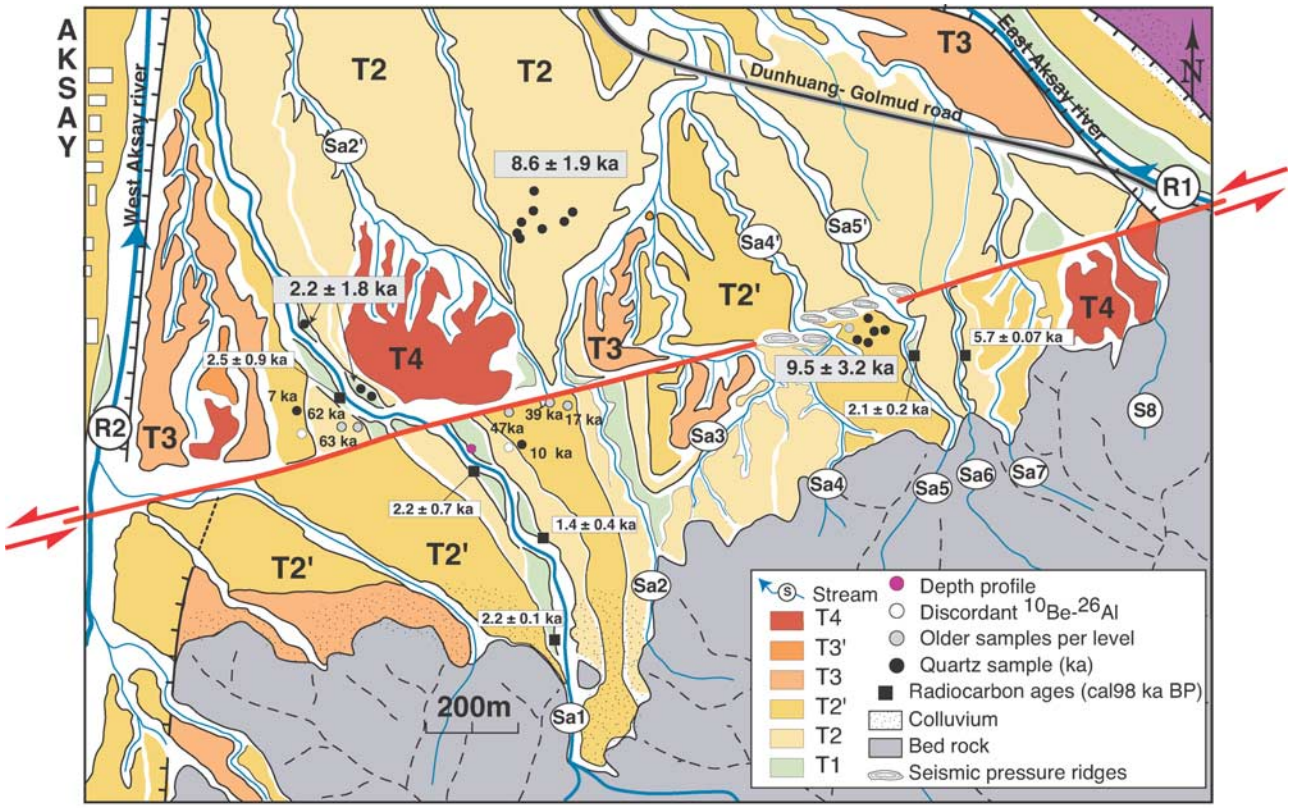

Figure 6. Geomorphic map of Aksay site showing terrace levels, offsets, and sample positions, with corresponding ages of isolated sample. The mean of sample groups are indicated with an error of 1σ in the gray boxes.

(Figures 4 and 5). The lowest set of terraces (T1) is confined within narrow channels incised by certain streams, particularly those of Sa1 and Sa2 (Figures 6, 7, and 8). North of the fault, some of the terraces may be fill terraces deposited on preexisting topography. The terrace levels that extend into the valleys south of the range front, however, are strath terraces, as indicated by bedrock abrasion along the lower surfaces of the deposits. For instance, the T2′ terrace level that caps tilted, coarse Quaternary conglomerates south of the fault and steeply dipping Neogene red beds north of it on the right bank of R1 is clearly a strath terrace.

[19] The largest offsets at Aksay are those of the risers that bound the T2′ terrace levels along the valleys of R1 and R2 (Figure 5). In the field, the clearest such offset (225 ± 10 m) is that of the riser (T3/T2′) on the west side of the R2 fan (Figures 4 and 5). This riser, which is marked by the limit of cultivated field and by the elevation contours (Figure 5), can be followed to the fault trace, both upstream and downstream, defining clear piercing points. A comparable though less well defined offset (220 ± 40 m) is apparent on the east side of the R2 channel (Figure 5). Here, a piercing point upstream cannot be as precisely defined, because the riser has been partly buried and smoothed by the more recent proximal T2 fans. Retrofitting the 225 m offset of the western riser on the images and topographic map, however, also realigns the straight, upstream and downstream segments of the eastern riser. The intersection of the fault trace with the channel of R1 is complicated by a large east bank tributary junction (Sa9, Figures 4 and 5). However, back

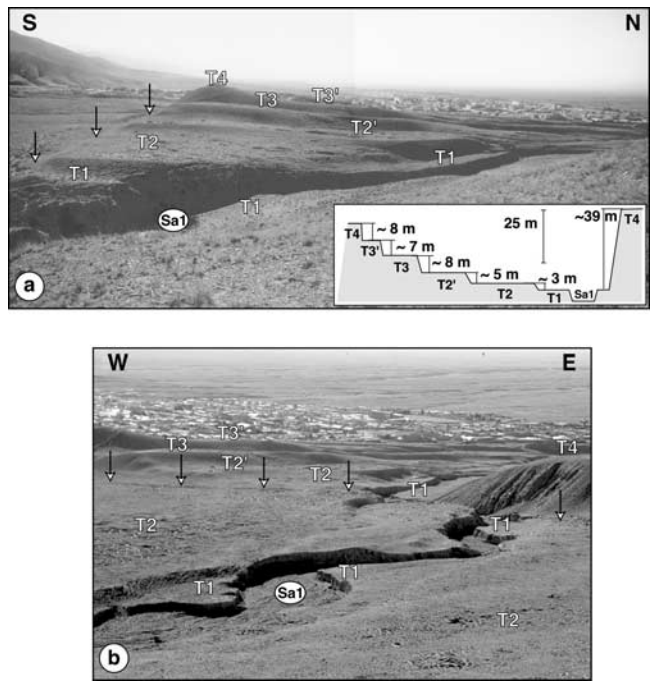

Figure 7. (a) View toward the west over flight of Quaternary terraces on west bank of stream Sa1 at Aksay city site. See Figure 5 for orientation. Inset shows simplified profile of relative terrace heights as deduced from total station measurements. (b) North looking view toward Tarim Basin, of offset of T1 and T2 risers along Sa1 stream.

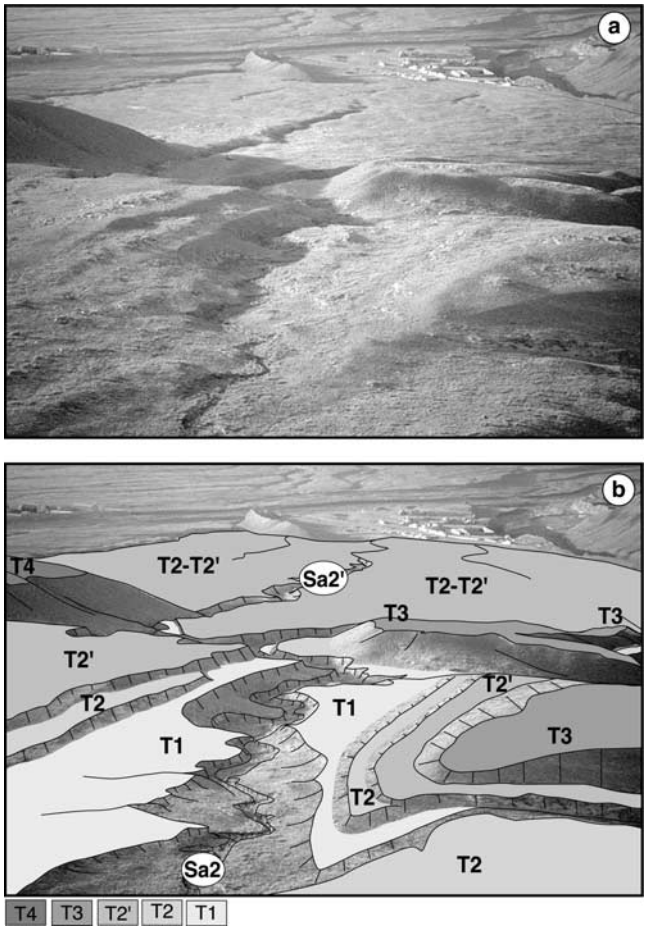

Figure 8. (a) North looking photograph of offset terrace risers along stream Sa2. (b) Geomorphic interpretation of Figure 8a. See Figure 5 for orientation.

slipping by 185 ± 20 m and 210 ± 20 m realigns the right and west bank risers, respectively (Figure 5). For either R1 or R2, the left bank riser offsets are larger and clearer than the east bank offsets. This is to be expected since upstream deposition and downstream lateral cutting by the left-laterally deviated rivers will preferentially degrade the geomorphic record on their right banks. Overall, we conclude that both river channels R1 and R2 have been offset by comparable amounts, 225 ± 10 m and 210 ± 20 m, respectively, after the T2′ terrace level was emplaced upstream from the fault.

[20] The offsets of the smaller stream channels that incise the T2′-T2 fans and terraces between R1 and R2 are for the most part smaller than 200 m, with two exceptions (Figure 6). The dog-legged channel of Sa3 is offset 175 to 215 m (195 ± 20 m). A slightly larger offset, 220 ± 20 m, realigns the channel of Sa5 upstream from the fault with that of Sa4 downstream (Sa4′, Figure 6). The upper channel of Sa5 and lower channel Sa4′ are much broader in the field and on the topographic map than their counterparts on the other side of the fault. Neither Sa4 nor Sa5 are now significantly offset by the fault. However, seismic pressure ridges are particularly well developed between Sa4 and Sa5, exhuming more shallow gravels than elsewhere, suggesting that a now buried channel of Sa5 may have followed the fault. Though none of these observations is conclusive, they suggest that recent capture may have straightened the courses of Sa4 and Sa5, erasing previous cumulative offsets.

[21] To gain a better understanding of the offsets of Sa1 and Sa2, we used a total station to measure the relative heights of the terraces and the shapes and heights of inset terrace risers between and adjacent to them (Figures 9 and 10). The uncertainties on such heights and shapes, as deduced from the total station profiles, depend on surface regularity and degree of preservation rather than on instrumental errors, which are on order of a few tens of centimeters [e.g., *Gaudemer et al.*, 1995]. We estimate these to be 2 m for the older surfaces (T3, T4) and 1 m for the younger surfaces (T1, T2). The oldest terrace surface (T4) stands as much as 56 ± 2 m above the river bed of R2, 39 ± 2 m above T2′ upstream from the fault (p17, Figure 10), and 43 ± 2 m above the bed of Sa1. The surface of T3 lies 37 ± 2 m above R2 and 20 ± 2 m above Sa1. That of T2′ is 12 ± 1 m above R2 upstream from the fault. Downstream from it, T2′ and T2 are, respectively, 12 and 8 m above Sa1. Finally, T1 stands a maximum of 5 ± 1 m above Sa1 north of the fault. The highest, best defined, fossil terrace risers are thus those between T4 and T3 (20 m), T3 and T2′ (10 m), and T2 or T2′ and T1 (4.5 m) (Figure 10). Most of them are fairly straight and can be traced all the way to the fault scarp, defining piercing points to within a few meters (Figures 6, 7, 8, and 10).

[22] Along Sa1, the alignment of the T2/T1 risers and the overall down-slope course channel cut into T2 and filled by T1, are best restored by 145 ± 10 m of back slip (Figures 7 and 11a). This cumulative sinistral offset, which postdates the abandonment of T2, is consistently constrained by the total station profiles and by retrodeformation of both the Corona image and 1/50,000 scale topographic map. A similar, though somewhat smaller offset of 135 ± 10 m is obtained by realigning the principal risers that bound the

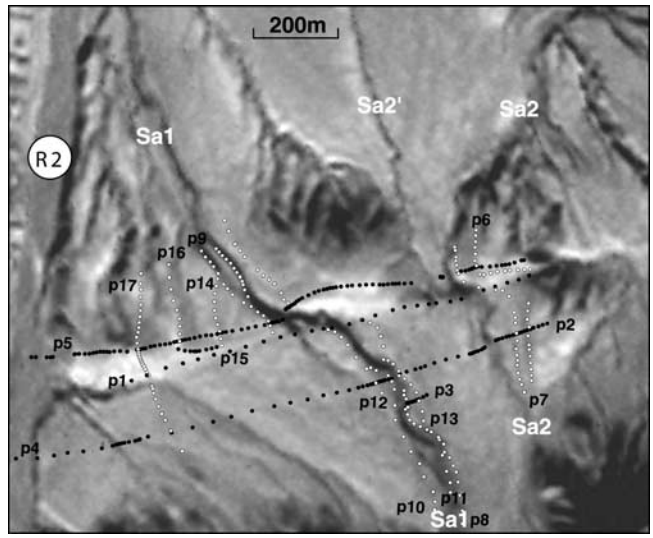

Figure 9. Positions of total station profiles at Aksay displayed on a SPOT image of the site. Positions of streams Sa1 and Sa2 (Figure 6) are also shown.

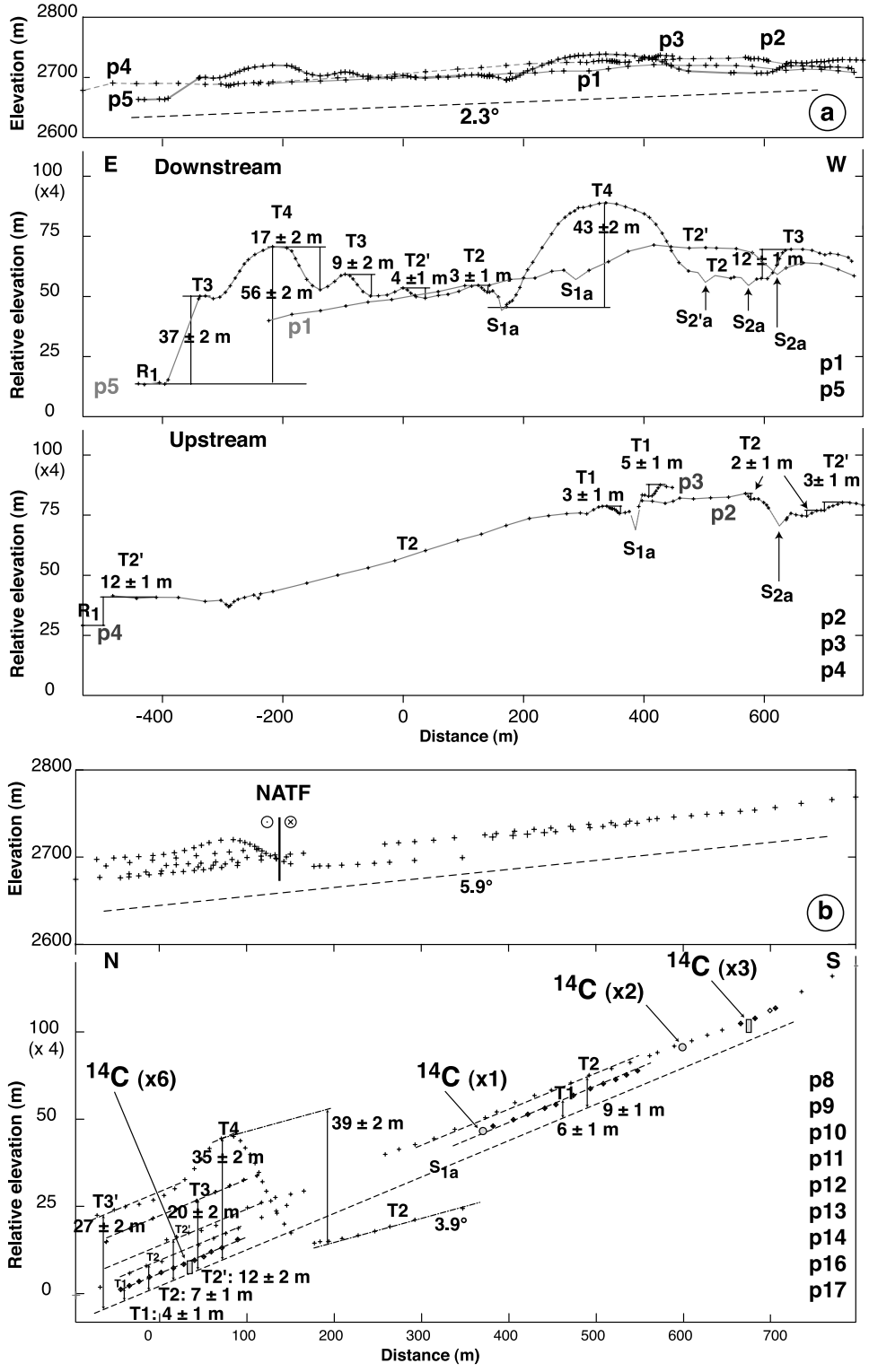

Figure 10. Leveling data from total station profiles in Figure 9. (a) N73°E projection (parallel to NATF) of along-strike profiles. (top) At 1 × 1 scale. Projection with vertical exaggeration (4X) (middle) of downstream profiles and (bottom) of upstream profiles. (b) N150°E projection (perpendicular to NATF) of across strike profiles. (top) At 1 × 1 scale. (bottom) Projection with vertical exaggeration (4X). Radiocarbon sampling sites along S1a are also indicated.

channel cut by Sa2 into T2 and T2′ on either side of the fault and filled by T1 (Figures 8 and 11b). Note also that retrofitting the upstream channel of Sa6 with the lower channel of Sa5 (Sa5′, Figure 6) yields an offset of 130 ± 15 m and that the sinistral offset of the T2′/T2 riser on the left bank of Sa1 is 165 ± 20 m. In addition, the present-day channels of both Sa1 and Sa2, which are incised into T1, show short dogleg offsets of 45 ± 5 m and 40 ± 5 m at the

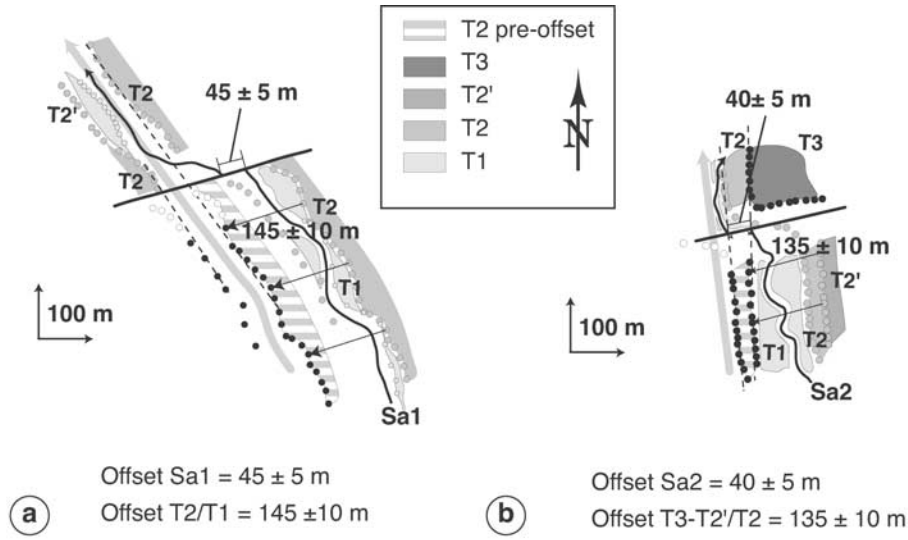

Figure 11. Reconstruction of riser offsets T2/T1 and T1/T0 from total station profiles, Corona and SPOT image retrofitting.

fault, respectively (Figures 6 and 11). Half a dozen stream channels comparable to Sa1 and Sa2 display sinistral offsets of similar sizes west of the Aksay fan (Figure 6).

3.2. Huermo Bulak

[23] The Huermo Bulak site is located 8 km east of old Aksay village (Figure 3), at the outlet of the Huermo Bulak River (R3) onto the piedmont bajada. This is the first large river outlet east of that of R1 along the Dangjin Shankou range. Locally, the fault is divided into two roughly parallel strands, ~150 m apart, that converge toward the east (Figure 12), and steeply bound a gouge zone exposed along the east facing cliff cut by the river (Figure 13). The southern strand (NATF) has the most prominent, geomorphic signature and clearest surface trace, but it is the northern strand (F2) that here marks the contact between the sheared metavolcanic bedrock and the thick Q_{2-3} piedmont fanglomerates. The river (R3), whose deeply incised valley extends southward to the highest summits of the range, has emplaced up to nine terrace levels or sublevels as it fanned out onto the bajada (Figures 12–15). The lowest terrace levels (T0, T0′) are essentially barren fanglomerates with only sparse grass. T0″ and T1 are well paved with rounded cobbles and pebbles, usually with thin soil and more grass than the lower levels (Figures 14 and 15). Patches of the surfaces of T2 and T3 are locally covered with loess (Figures 13–15). Where exposed along the river cut cliff, T2′ and T2 are strath terraces (Figure 13). The risers between the different terrace levels are usually steep and most of them reach the fault trace. Hence, even though older risers are more degraded, piercing points positions can be defined with maximum uncertainties of ~10% (Figure 12).

[24] On a profile across the flight of terrace steps on the west bank of R3, roughly parallel to the fault, the total elevation difference between the riverbed and T4 is slightly more than 50 meters, comparable to that observed in Aksay. The most extensive terrace levels near the fault are T2′-T2 and T3′-T3 (Figures 12 and 15). They coalesce downstream to form most of the bajada surface between the active fans. The riser offsets we mapped and measured on SPOT and rectified Corona images along the main trace of the NATF fall into three groups (Figures 12 and 15). The highest riser on the west side of R3, between T3 and T2, shows the largest offset, 225 ± 20 m. Also, west of R3, the left bank T2/T1 riser and the Sh1 channel, incised into T2, are offset by 105 and 95 ± 10 m, respectively (Figure 12). A comparable offset (110 ± 10 m) is observed for the T2/T1 riser on the right bank of the river Sh3, east of Huermo Bulak (Figure 12). Finally, the T1/T0″ riser on the left bank of R3 is offset by 60 ± 5 m. Somewhat smaller offsets (45 ± 5 m) of one channel incised into T2 and T1 (Sh2) east of R3, and of the T2/T1 riser along the right bank of Sh3, are also observed. Overall, the range of offsets here is roughly comparable to that documented at Aksay. In addition, even though the trace of F2 is rather faint across most of the youngest terraces, two clear offsets can be identified along it. The largest one (50 ± 5 m) is that of the T3/T2 riser west of Sh1. The other (20 ± 5 m) is that of the cliff cut into T2′-T2 along R3 right bank (Figures 12 and 14).

3.3. Bang Guo Ba

[25] Less than 2 km west of Bang guo ba, the fault divides again into two branches (NATF, F2′), that isolate a ~1-km-long push-up hill between the Bang guo ba river (R4) and the next stream to the west Sb1 (Figure 16). These two branches diverge 300 m apart then converge again to meet 2 km eastward in the valley of the Bang guo ba river (R4, Figure 16), whose headwaters reach the crest of the range. Locally transpressive motion on the fault is also clear from the presence of a north vergent thrust (F3) across the most ancient terraces (T3) of the bajada north of the fault, and of another, smaller push-up hill west of stream Sb1 (Figure 16). At the eastern junction of the two fault zones, the Bang guo ba river canyon clearly exposes the deformation of the bedrock and capping strath terraces (T2′, T2, Figure 17). The main fault strand (NATF) dips steeply

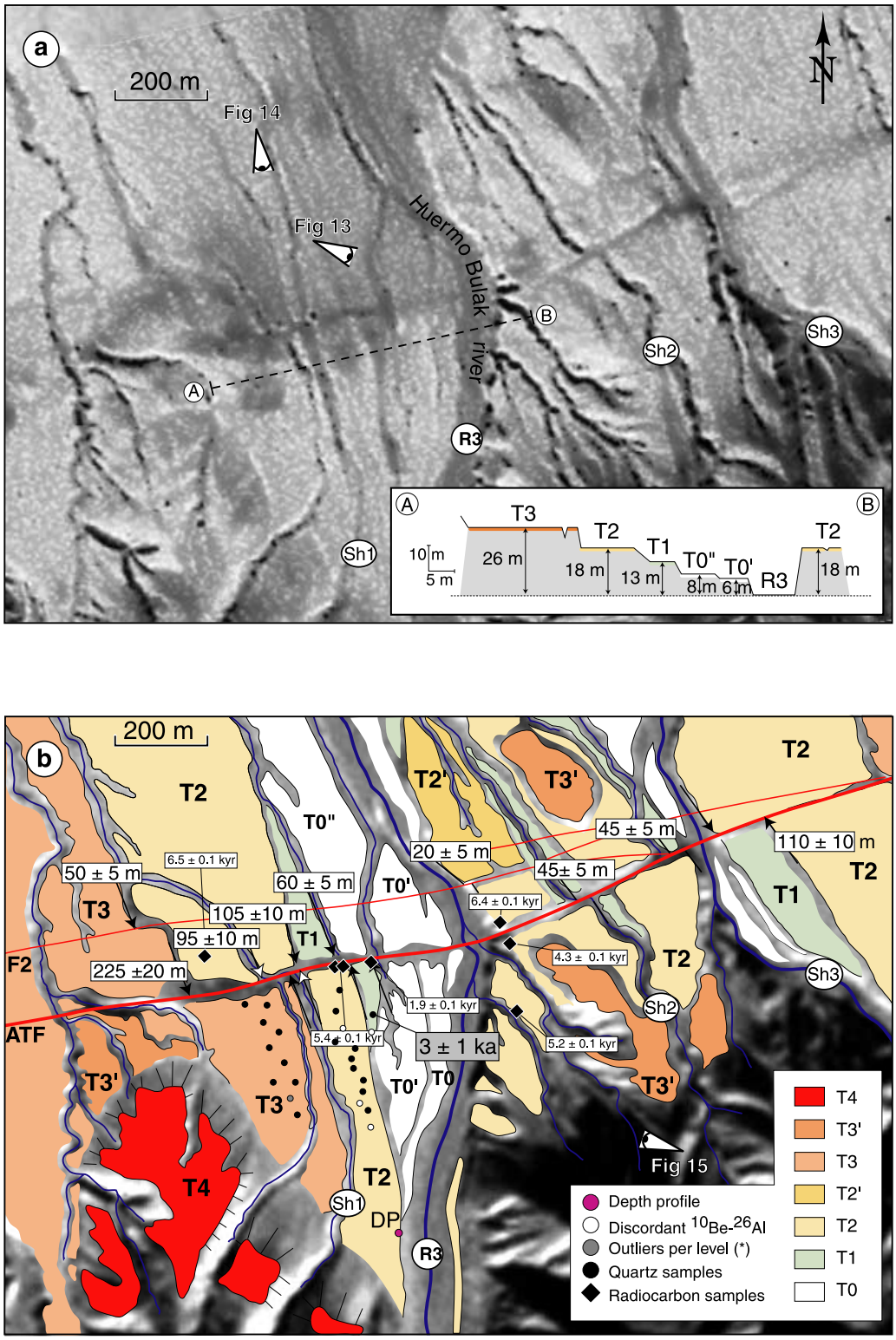

Figure 12. Huermo Bulak site. (a) SPOT image of ATF cutting across terraces at Huermo Bulak. Point of views of Figures 13 and 14 are indicated. Inset shows relative heights of terraces above active river along profile AB (Figure 12a) as deduced from altimeter measurements. (b) Geomorphic map of Huermo Bulak. Offsets of principal risers and sample positions are indicated. The average ^{10}Be model ages of T3 and T2 surfaces are 44.2 ± 10 and 8.4 ± 4.3 ka, respectively (±1σ) (dark circles, Table 3). The ^{14}C calibrated ages (years B.P.) are also indicated; some of these are weighted mean of multiple comparable samples (see Table 1 for detail). Point of view of Figure 15 is indicated.

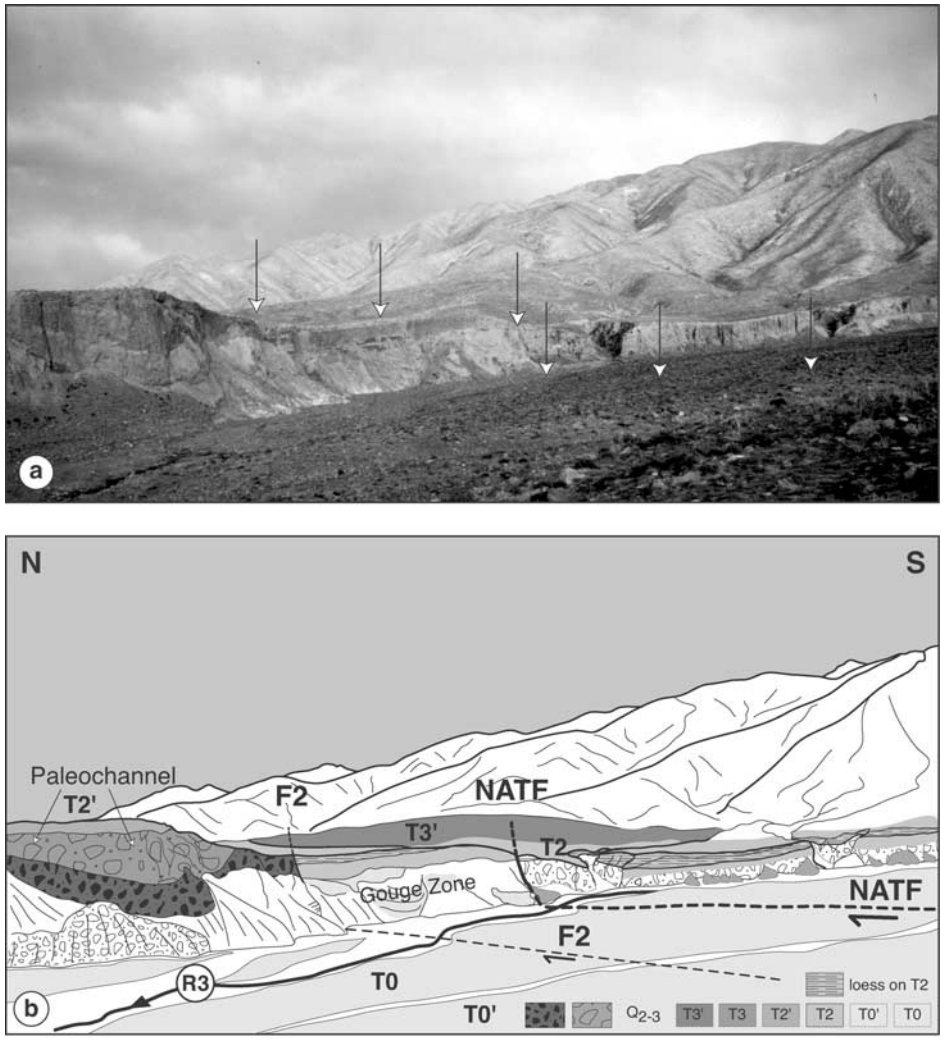

Figure 13. East looking view of Huermo Bulak river east cliff section across ATF. See Figure 12a for orientation. (b) Geomorphic interpretation of Figure 13a.

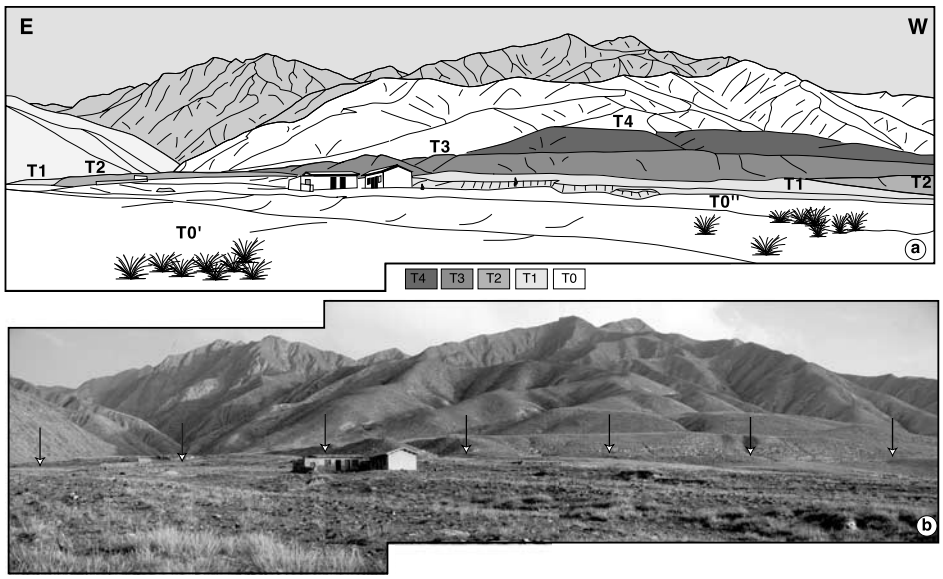

Figure 14. South looking view of terraces and range front at Huermo Bulak. See Figure 12a for orientation.

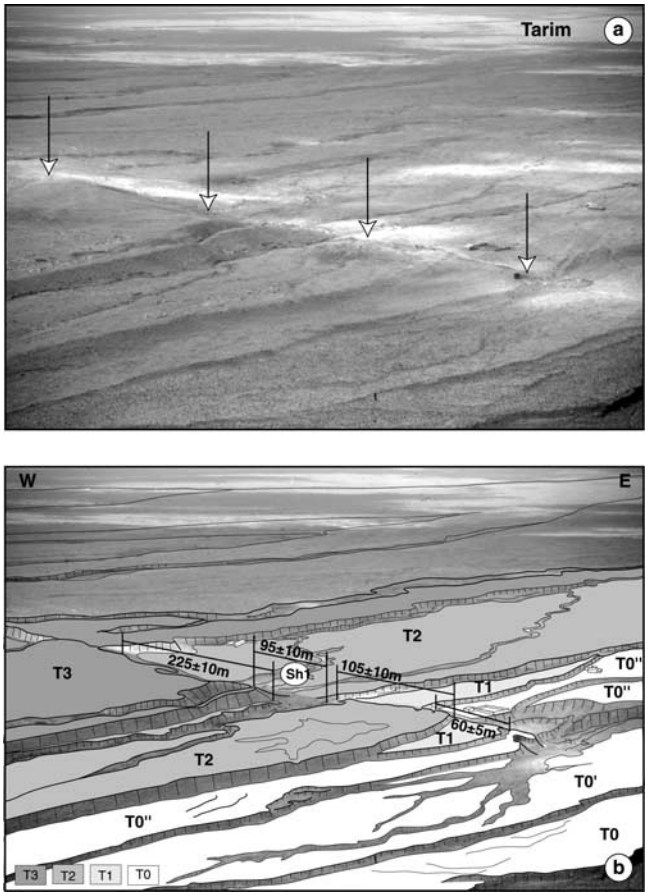

Figure 15. Northwest looking view of horizontal offset of the Huermo Bulak terrace surfaces and risers. See Figure 12b for orientation. (b) Geomorphic interpretation of Figure 15a.

southward, juxtaposing sheared, and schistosed Neogene red beds with the foreland Q_{2-3} fanglomerates. Two other large, 50° south dipping fault planes (F2′) are visible south of the main strand (Figure 17). One of them emplaces brecciated, Paleozoic metavolcanics onto the sheared red beds. All three faults cut and offset terraces and channels (Figure 17). The main terrace surface (T2′-T2) on the right bank of R4, in particular, is vertically offset a maximum of 3.7 ± 0.5 meters by the NATF strand of the fault.

[26] As at Huermo Bulak, we identify nine distinct terrace levels or sublevels around Bang guo ba (Figure 16) with the two main groups of terrace surfaces, T2′-T2 and T3′-T3, making up much of the bajada. Generally, T2′-T2 is mostly well paved with cobbles while T3′-T3 is usually mantled by reworked loess and silt (Figure 18). The terrace riser offsets along this stretch of the fault are comparable to those observed near Huermo Bulak, but long-term offsets >200 m are clearest. Three such offsets stand out particularly well. Both of the risers bounding the T3′-T3 interfluvial prong west of the R4 and north of the push-up hill are sinistrally displaced by 240 ± 20 m relative to their counterparts south of the fault (Figure 16). The T3′/T2′-T2 riser bounding the west side of the large T2′-T2 fan emplaced by stream Sb1, west of R4, is offset by as much as 260 ± 30 m. In addition, the right bank risers bounding the T2′-T2 fan apexes east of Bang guo ba are offset by 165 to 215 ± 20 m. Downstream from the fault, these risers lie in complex areas with deep, often beheaded, channels incising T3 or T2′, or following the riser base. The T3′/T2′ riser on the left bank of Sb2 is offset by 205 ± 20 m. There are three more 165 ± 20 m offsets. Two are those of the T2′/T2 riser on the left bank of Sb1, another of the T2′/T2 riser on the east bank of R4, and finally the T2′/T2 riser on the east bank of Sb1 (Figures 16 and 17). The other, most common offset values are somewhat greater than 35–40 m. The right bank cliff incised by R4 into T2, for instance, is offset 36 ± 3 m (Figure 16). Because two of these smaller offsets are of right bank cliffs subject to current lateral cutting by the rivers, they are minima. Finally, south of the T3′ prong and just east of Sb1, we mapped one 9 m and two 20 m offsets of modern channels incised into T1, and meter-high pressure ridges along the main NATF strand of the fault, attesting to the occurrence of large, surface breaking earthquakes (M > 7) on this segment of the fault.

4. Morphochronology

[27] The radiocarbon dating results for all three sites are given in Table 1, and the cosmogenic dating results for Aksay, Huermo Bulak, and Bang guo ba are presented in Tables 2, 3, and 4, respectively. A description of the dating methods is presented in Appendix A. The ^{10}Be and ^{26}Al model ages are generally concordant within 20% and are consistent with simple exposure histories. Samples with greater discordancy are presented in Tables 1–4 but are not used in the discussion. However, the ^{26}Al ages appear to be systematically younger than the ^{10}Be model ages (Tables 2, 3, and 4). We believe that this may be due to loss of volatile Al complexes during sample preparation. In general, we tend to have more confidence in the ^{10}Be ages, as they require only one measurement (^{10}Be/^{9}Be), while ^{26}Al requires measurement of both ^{26}Al/^{27}Al and ^{27}Al concentration. In this paper we will discuss only the ^{10}Be results for ''concordant'' samples which we define as $0.8 > {}^{26}Al_{age}/{}^{10}Be_{age} < 1.2$. As ^{10}Be ages are systematically older than the ^{26}Al ages, using the ^{10}Be data alone will, holding all other factors constant, yields a relative maximum age–minimum rate estimate. The samples for cosmogenic exposure dating were typically hand-sized cobbles embedded in surfaces and were mostly nearly pure quartz derived from veins and a few granites.

4.1. Old Aksay

[28] To date the principal terraces (T1, T2, T2′) in the vicinity of the fault we collected a total of 16 charcoal or bone fragments in subsurface layers and 55 quartz-rich cobbles partially embedded in the surfaces (Figures 6 and 18). We could not, however, sample the Aksay fan near the fault because of widespread surface disruption due to cultivation and building (Figures 4 and 5). Also, because of a locally 20- to 50-cm-thick loess cover between the range front and the hills north of the fault, we were only able to sample the T2 and T2′ surfaces south of the fault east of Sa1. The scarcity of quartz-rich cobbles precluded extensive subsurface sampling for cosmogenic dating. Only single subsurface cobbles were dated where possible. Organic fragments, mostly charcoals and a few bones, were

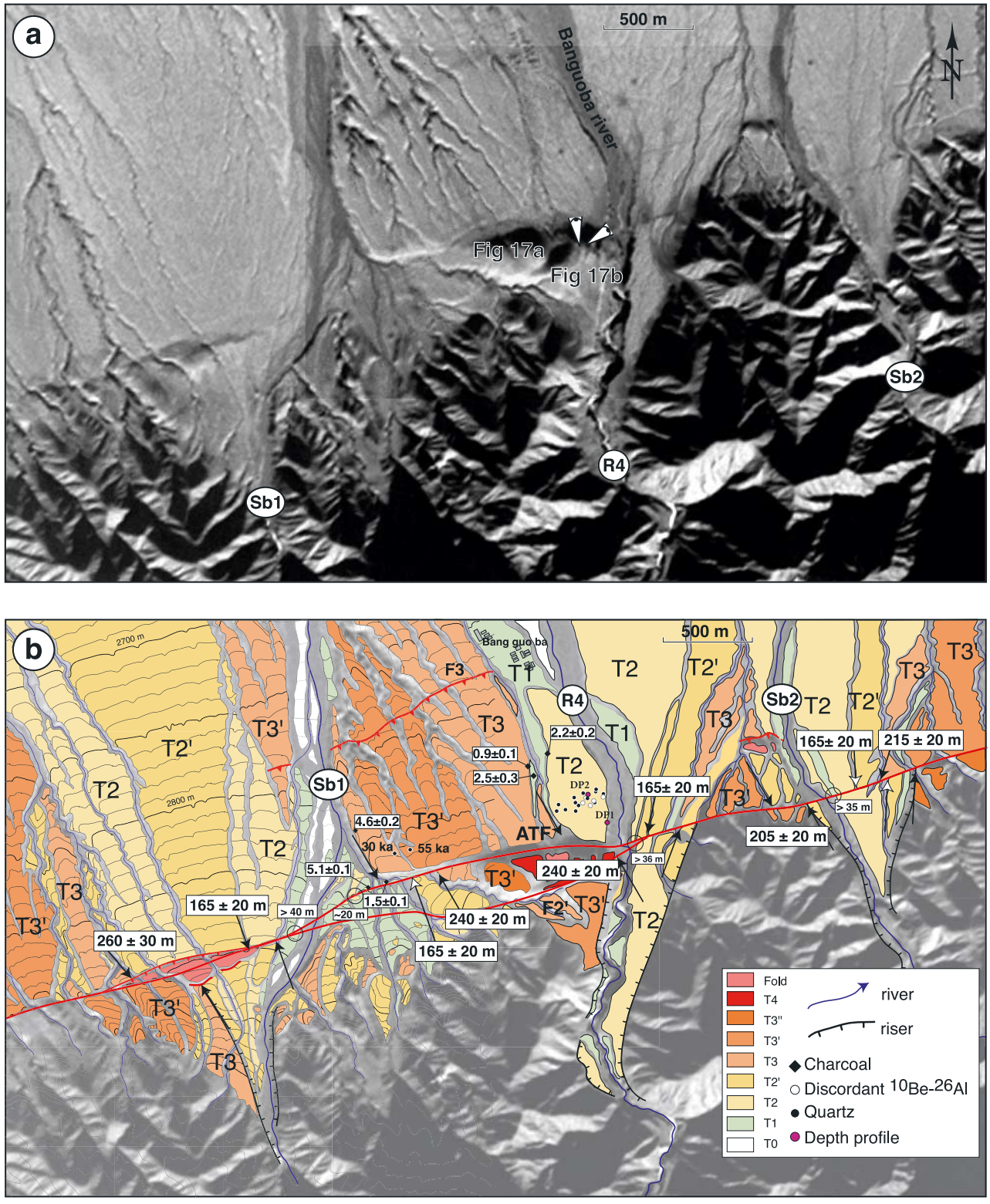

Figure 16. (a) Combined SPOT and rectified Corona image of fans along ATF near Bang guo ba. Point of views of Figures 17a and 17b are indicated. (b) Geomorphic interpretation of faulting across the fan apexes in the central part of Figure 16a. Elevation contours (from 1/50,000 topographic map) are projected on SPOT image. Offsets of principal risers and sample positions are indicated. The ^{14}C calibrated ages (ka) are also indicated. The average ^{10}Be model age of T2 is 6.2 ± 1.7 ka (±1σ) (dark circles, Table 4).

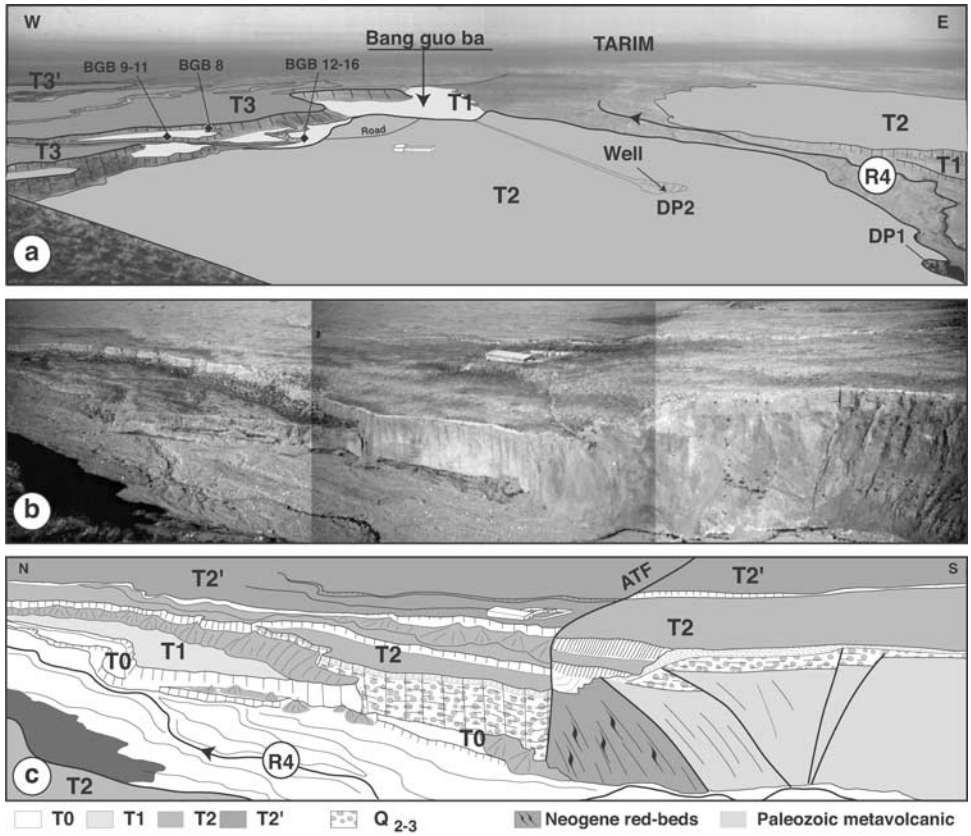

Figure 17. (a) North looking view of offset T3/T2 riser on left bank of Bang guo ba river. See Figure 16 for orientation. (b) East looking view of Bang guo ba river cut into terraces T2 and T1 and bedrock. (c) Interpretive sketch of Figure 17b. Note faulting between Paleozoic metavolcanics and Neogene red beds, as well as between Neogene and Quaternary gravels. Q2-3 are late-middle Pleistocene Quaternary deposits.

mostly retrieved from the topmost fluvial gravels of the terraces, exposed in stream-cut faces that we rejuvenated (Table 1 and Figures 6 and 19).

[29] Three exposures in the shallowest deposits of T1 on the west bank of Sa1 (Figures 6 and 7) yielded stratigraphically consistent ^{14}C ages (Table 1 and Figure 18). Several of the samples dated belong to thin, charcoal-rich lenses that often include bone fragments and probably correspond to in situ, fossil campfires (Figure 18a). On the two stream-cut sections, upstream and downstream from the fault, the oldest ages obtained for the deepest samples (1.25 and 2.8 m), are 2346 ± 9 and 2541 ± 174 years B.P., respectively (Figure 18b). Another sample found on the top surface of T1, beneath the T2/T1 riser colluvial wedge, in a 50-cm-deep pit that we dug at the base of this riser, yields an age of 2197 ± 9 years B.P. Finally, three charcoals in shallow fluvial gravels from T1, in the channel of Sa5 (Figure 6), yield ages between 2029 ± 72 years B.P. and 2243 ± 89 years B.P. (Table 1) compatible with those along Sa1. Thus we conclude that T1 was abandoned between 2.4 and 2 ka (2.2 ± 0.2 ka).

[30] The cosmogenic ^{10}Be and ^{26}Al surface exposure dating of the cobbles collected on T1, north of the fault yields a dispersed pattern with two groups of ages (Figure 19 and Table 2). This dispersion may be in part related to the fact that, where sampled, this terrace forms a narrow, discontinuous ledge only 3 to 4 m above the streambed, along the base of the highest, and presumably oldest, T4 hill, and downstream from the narrow gully incised by the stream as it crosses the fault (Figures 6, 7, and 8). That transport between adjacent surfaces and inheritance of cosmogenic nuclides plays a role in determining the distribution of surface ages is clear from the dispersion of ages among samples taken from the active stream channel which range from essentially zero age to ~60 ka (Table 2). One group of six samples on T1 (including some discordant Al/Be age ratios) shows very young ^{10}Be model ages (170–880 years) as otherwise found only in the river bed (340–600 years) (Table 2). We infer these very young samples to have been emplaced by an exceptional, recent flood, as already documented on another terrace at the foot of the Burhan Budai range [*Van der Woerd et al.*, 1998, 2000, 2002b]. Another group of five concordant samples have ages between 1.8 and 5.6 ka. The four youngest of these ^{10}Be model ages are, within error, compatible with the T1 abandonment age, ~2 ka, inferred from radiocarbon dating. Model ages older than the abandonment age can be explained by either inheritance or diachronous emplacement of the surface. Assuming zero inheritance would yield a maximum age for the beginning of emplacement; any real

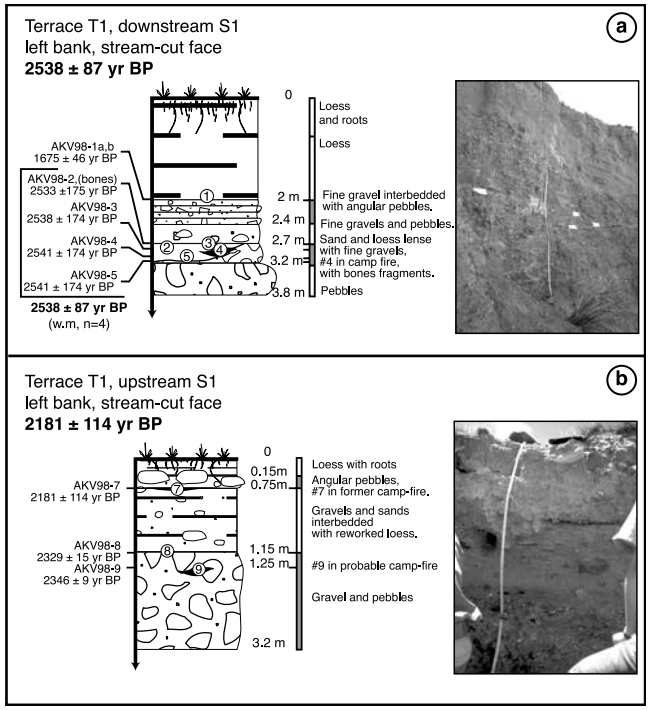

Figure 18. Photographs and sketches of left bank stream cut faces of T1 terrace from which charcoal and bone samples were retrieved at Aksay. (a) Downstream from the fault and (b) upstream from the fault.

inheritance would reduce this age estimate. Eliminating the one clear outlier (AT12-15, 34.5 ± 2.2 ka, Table 2), the five cosmogenic ages can be interpreted to indicate that the emplacement of T1 postdates 5500 years B.P. with abandonment at 2.2 ± 0.2 years B.P., implying that the streams may have occupied this surface for ~3000 years.

[31] Depth-corrected subsurface samples can be used to place a maximum age bracket on the abandonment age of a surface [*Anderson et al.*, 1996; *Hancock et al.*, 1999; *Mériaux et al.*, 2004]. Here the youngest subsurface samples from T1 are ~10.8 ka, considerably older than the surface ^{10}Be ages and^{14}C ages and thus too old to represent the age of T1. The much older subsurface samples (>300 ka, Table 2) could plausibly be explained by burial of samples derived from T2. For instance burial of a recent river cobble with a predepositional ^{10}Be concentration similar to that of AT02-4 would yield a depth-corrected age of ~300 ka if buried to a depth of 2 m.

[32] We retrieved fewer charcoal fragments from the shallowest gravel layers of T2 than from those of T1. The only one found near Sa1, on the east bank upstream from the fault (Figure 6), at the base of loess capping gravels, yields an age of 1378 ± 39 years B.P. (AKV98-6), 300 years younger than the youngest age obtained for the shallowest charcoal on T1 (Table 1) and hence inconsistent with the abandonment age of T1. Clearly, this yields no constraint on the depositional history of the stratigraphically older T2 surface. Four other samples farther east and west along the fault (Figures 3, 4, and 6 and Table 1) on the other hand, yield mutually consistent ages that are compatible with the abandonment of T2 prior to the emplacement of T1. Sample AKV98-13, collected from a thin sand and gravel layer, on the right bank of Sa6 south of the fault, has an age of 5673 ± 70 years B.P. (Figure 6). West of Aksay, three other charcoals (AK00-5,6,7) in similar shallow fluvial deposits north of the fault, on either bank of a stream with a catchment comparable to that of Sa1 (Figure 4), have ages ranging from 5599 ± 12 years B.P. to 7289 ± 32 years B.P. (Table 1). Taken together, these four ages thus appear to indicate that the T2 terrace surface was abandoned 6.5 ± 0.8 ka, with small differences depending upon location.

[33] Cosmogenic exposure dating of the 24 cobbles collected on loess and soil cover free patches of the T2 and T2′ surfaces, upstream and downstream from the fault (Figures 6 and 19), yields a somewhat simpler picture than that found on T1 (Table 2). All the ages are older than 6.2 ± 0.5 ka (AK98-36) and the majority of the samples (17) yield concordant ages younger than 22 ka with a distinct cluster of 15 ages between 6.2 and 13.9 ka (Figure 19). As on T1, the lower bound in the distribution of cosmogenic ages agrees with the radiocarbon age, 6.5 ± 0.8 ka, and as such, we infer that T2 was abandoned prior to 5500–6500 years and to the beginning of T1 emplacement. If abandonment of T2′-T2 occurred at 6.5 ka, then older ages must again reflect either diachronous emplacement of T2′-T2, inheritance due to predepositional exposure, or derivation from older surfaces nearby. Two samples with ages of 16.8 and 21.1 ka (AK2U-2 and AK98-35, respectively) and four samples that range between 38.9 ± 2.7 and 62.7 ± 4.2 ka (Table 2 and Figure 19) clearly stand out as outliers to the 6.2–13.9 ka cluster. We infer that these cobbles may have been derived from higher terrace levels. Indeed, all of them come from areas of the T2′-T2 surface that lie near the base of the T4-T3 hills, suggesting that T4 might be as old as 63 ka. Similarly, the apparently old samples from the streambed of Sa1 contain reworked cobbles that appear to have originated in the three main terrace levels upstream (T1, T2′-T2, and T4) (Table 2).

[34] The surface exposure ages obtained thus confirm the conclusion from radiocarbon dating that the T2′-T2 terraces, the most extensive terrace level at Aksay and in the foreland bajada north of the Dangjin Shankou range, was abandoned around 6.5 ka, but also that its emplacement started with the strong post Last Glacial Maximum (LGM) warming around 13.9 ka, and lasted until the end of the humid, early Holocene optimum (EHO), in agreement with climatic forcing, as documented elsewhere in northern Tibet [*Gasse et al.*, 1991; *Van der Woerd et al.*, 1998; *Lasserre et al.*, 1999; *Van der Woerd et al.*, 2000, 2002b; *Ritz et al.*, 2003; *Brown et al.*, 2003; *Barnard et al.*, 2004a, 2004b; *Mériaux et al.*, 2004]. Unfortunately, we do not have sufficient data or precision to confidently separate the ages of T2 and T2′.

4.2. Huermo Bulak

[35] At six spots near the fault, we found abundant charcoal, much of it in clusters suggestive of campfires, or in thin layers of peat (Figure 12). A total of 17 distinct fragments were ^{14}C dated, most of them in the topmost layers of T2, on either side of the Huermo Bulak river (Table 1). The T2 charcoals found on the east bank of the river were collected at depths between 1 and 3 m in steep, gully cut exposures that we cleared. All of them lay in silt and clay layers beneath thin gravel horizons. The oldest

Table 1. Radiocarbon Results From the Aksay Segment of the ATF

Sample	Depth, cm	Description	Material	^{13}C	Fraction Modern	$\delta^{14}C$	^{14}C Age, years	Calibrated Age, cal years B.P.[a]
			Aksay					
AKV98-1B	215	T1 left bank downstream Sa1	charcoal	−25	0.7997 ± 0.0033	−200.3 ± 3.3	1800 ± 40	1723 ± 90
AKV98-1A	215		charcoal	−25	0.8042 ± 0.0036	−195.8 ± 3.6	1750 ± 40	1659 ± 53
								1675 ± 46[b]
AKV98-3	265	T1 left bank downstream Sa1	charcoal	−25	0.736 ± 0.0029	−264 ± 2.9	2460 ± 40	2538 ± 174
AKV98-4	280		charcoal	−25	0.7351 ± 0.003	−264.9 ± 3	2470 ± 40	2541 ± 174
AKV98-2B	282		bone	−20	0.7376 ± 0.0033	−262.4 ± 3.34	2440 ± 40	2533 ± 175
								2538 ± 87[b]
AKV98-5	285	T1 left bank downstream Sa1	charcoal	−25	0.735 ± 0.003	−265 ± 3	2470 ± 40	2541 ± 174
AKV98-7	75	T1 left bank upstream Sa1	charcoal, fire place	−25	0.7647 ± 0.0032	−235.3 ± 3.2	2150 ± 40	2181 ± 114
AKV98-8	110		charcoal	−25	0.7523 ± 0.0031	−247.7 ± 3.1	2290 ± 40	2329 ± 15
AKV98-9	125		charcoal, fire place	−25	0.7469 ± 0.0036	−253.1 ± 3.6	2340 ± 40	2346 ± 9
GK410-1	100	T1 left bank colluvial edge	charcoal	−25	0.7622 ± 0.0043	−237.8 ± 4.3	2180 ± 50	2213 ± 93
GK410-1b	100	upstream, Sa1	charcoal	−25	0.7666 ± 0.0043	−233.4 ± 4.3	2140 ± 50	2171 ± 124
								2197 ± 74[b]
AKV98-10	80	T1 right bank of Sa5	charcoal	−25	0.7686 ± 0.0059	−231.4 ± 5.9	2110 ± 70	2143 ± 149
AKV98-12	100		bone	−20	0.7739 ± 0.0031	−226.1 ± 3.1	2060 ± 40	2029 ± 72
AKV98-11	110		charcoal	−25	0.7573 ± 0.0034	−242.7 ± 3.4	2230 ± 40	2243 ± 89
AKV98-6	30	T2 right bank upstream Sa1	charcoal	−25	0.8275 ± 0.0034	−172.5 ± 3.4	1520 ± 40	1378 ± 39
AKV98-13	20	T2 right bank of Sa6	charcoal	−25	0.5398 ± 0.0045	−460.2 ± 4.5	4950 ± 70	5673 ± 70
			West of Aksay					
AK00-5	110	T2′	charcoal	−25	0.4524 ± 0.0018	−547.6 ± 1.8	6370 ± 40	7289 ± 32
AK00-6	70	T2, colluvial edge	charcoal	−25	0.546 ± 0.0021	−454 ± 2.1	4860 ± 40	5599 ± 12
AK00-7	160	T2′	charcoal	−25	0.462 ± 0.0133	−538 ± 13.3	6200 ± 240	7085 ± 331
AK00-13	145	T1	charcoal, peat level	−25	0.7765 ± 0.0042	−223.5 ± 4.2	2030 ± 50	1975 ± 50
AK00-15	145		charcoal, peat level	−25	0.7732 ± 0.0037	−226.8 ± 3.7	2070 ± 40	2051 ± 60
			Huermo Bulak					
EAK00-9	57	T1 left bank upstream R3	charcoal, peat level	−25	0.7784 ± 0.0035	−221.6 ± 3.5	2010 ± 40	1947 ± 49
EAK00-2	130	T2 right bank upstream R3	charcoal	−25	0.568 ± 0.0025	−432 ± 2.5	4540 ± 40	5186 ± 121
AKS1A1	290	T2 right bank upstream R3	charcoal	−25	0.6202 ± 0.0033	−379.75 ± 3.27	3840 ± 50	4251 ± 99
AKS1A2	290		charcoal	−25	0.6221 ± 0.0032	−377.92 ± 3.2	3810 ± 50	4175 ± 81
AKS1B1	290		charcoal	−25	0.6143 ± 0.0035	−385.7 ± 3.48	3910 ± 50	4335 ± 82
								4353 ± 50[b]
AKS2	520	T2 right bank downstream R3	charcoal	−25	0.5144 ± 0.003	−485.59 ± 2.95	5340 ± 50	6129 ± 131
AKS9	100		charcoal	−25	0.4942 ± 0.0026	−505.81 ± 2.56	5660 ± 50	6425 ± 66
								6365 ± 59[b]
BIAS	58	T2 left bank upstream R3	charcoal	−25	0.9485 ± 0.0087	−51.5 ± 8.7	420 ± 80	427 ± 98
A1GK bis	63	shelter dug	charcoal	−25	0.9272 ± 0.012	−72.77 ± 12.03	610 ± 110	595 ± 71
A1GK	63	peat levels	charcoal	−25	0.9915 ± 0.0055	−8.5 ± 5.5	70 ± 50	145 ± 114
D1TP	74		charcoal	−25	0.9843 ± 0.0054	−15.69 ± 5.45	130 ± 50	226 ± 75
A2GK	112		charcoal	−25	0.9217 ± 0.0044	−78.3 ± 4.4	660 ± 40	611 ± 50
A3GK	128		charcoal	−25	0.9032 ± 0.0071	−96.8 ± 7.1	820 ± 70	732 ± 58
B4PT	140		charcoal	−25	0.8961 ± 0.0044	−103.9 ± 4.4	880 ± 40	814 ± 79
A4GK	145		charcoal	−25	0.9061 ± 0.005	−93.9 ± 5	790 ± 50	704 ± 33
C5TP	175		charcoal	−25	0.5564 ± 0.0031	−443.63 ± 3.11	4710 ± 50	5451 ± 126
GK510	100	T2 downstream west of Sh1	charcoal	−25	0.49 ± 0.0037	−510 ± 3.7	5730 ± 70	6525 ± 111
			East Side of the Aksay Fan, West Huermo Bulak					
PTB97	100	T2′-T2 fan	charcoal, fire place	−25	0.5421 ± 0.0031	−457.9 ± 3.1	4920 ± 50	5652 ± 53
PTH97	130		charcoal, fire place	−25	0.6413 ± 0.0036	−358.7 ± 3.6	3570 ± 50	3848 ± 73
			Bang Guo Ba					
BGB98-1	140	T1, right bank of Sb1	charcoal	−25	0.8198 ± 0.0034	−180.2 ± 3.4	1600 ± 40	1476 ± 59
BGB98-2	120		charcoal	−25	0.8183 ± 0.0043	−181.7 ± 4.3	1610 ± 50	1482 ± 65
BGB98-3	60		charcoal	−25	0.8213 ± 0.0047	−178.7 ± 4.7	1580 ± 50	1471 ± 60
								1476 ± 35[b]
BGB98-9	25	T1 channel incised T2	charcoal	−25	0.9213 ± 0.0041	−78.7 ± 4.1	660 ± 40	611 ± 50
BGB98-10	40	peat levels	charcoal	−25	0.8894 ± 0.0056	−110.6 ± 5.6	940 ± 60	843 ± 112
BGB98-11	60		charcoal	−25	0.7435 ± 0.0223	−256.5 ± 22.3	2380 ± 250	2438 ± 317
BGB00-5	130		charcoal	−25	0.806 ± 0.0031	−194 ± 3.1	1730 ± 40	1634 ± 69
BGB00-6	150		charcoal	−25	0.74 ± 0.0033	−260 ± 3.3	2420 ± 40	2528 ± 174
BGB98-13	35	T1	charcoal	−25	0.9106 ± 0.0044	−89.4 ± 4.4	750 ± 40	678 ± 16
BGB98-14	105		charcoal	−25	0.7766 ± 0.0042	−223.4 ± 4.2	2030 ± 50	1984 ± 59
BGB98-15	140		charcoal	−25	0.768 ± 0.0131	−232 ± 13.1	2120 ± 140	2125 ± 200
BGB98-16	140		charcoal	−25	0.8099 ± 0.0038	−190.1 ± 3.8	1690 ± 40	1612 ± 75
BGB98-4	90	T2, right bank of Sb1	charcoal	−25	0.6301 ± 0.003	−369.9 ± 3	3710 ± 40	4061 ± 81
BGB98-5	115		charcoal	−25	0.5583 ± 0.0023	−441.7 ± 2.3	4680 ± 40	5393 ± 73
BGB98-6	115		charcoal	−25	0.5363 ± 0.0024	−463.7 ± 2.4	5010 ± 40	5760 ± 100
BGB98-7	50	T3, right bank of Sb1 in loess cap	charcoal	−25	0.6016 ± 0.0027	−398.4 ± 2.7	4080 ± 40	4617 ± 167
BGB98-8	25		charcoal	−25	0.886 ± 0.0039	−114 ± 3.9	970 ± 40	865 ± 68

Table 1. (continued)

Sample	Depth, cm	Description	Material	^{13}C	Fraction Modern	$\delta^{14}C$	^{14}C Age, years	Calibrated Age, cal years B.P.[a]
BGB98-12	30	T2, loess cap	charcoal	−25	0.8941 ± 0.004	−105.9 ± 4	900 ± 40	827 ± 84
			Qing Shui gou					
AKG98-6	38	T1	charcoal	−25	0.7806 ± 0.0038	−219.4 ± 3.8	1990 ± 40	1940 ± 52
AKG98-4	40		charcoal	−25	0.9708 ± 0.008	−29.2 ± 8	240 ± 70	288 ± 137
AKG98-5	40		charcoal	−25	0.8573 ± 0.0066	−142.7 ± 6.6	1240 ± 70	1165 ± 101
AKG98-3	70		charcoal	−25	0.777 ± 0.0036	−223 ± 3.6	2030 ± 40	1980 ± 52
AKG98-2	230		charcoal	−25	0.7898 ± 0.0058	−210.2 ± 5.8	1900 ± 60	1817 ± 78

[a] *Stuiver et al.* [1998].
[b] Weighted mean.

sample, AKS-9, is 6425 ± 66 years B.P., and the youngest, AKS1A2, 4175 ± 81 years B.P. (Table 1 and Figure 20). On the west bank of the river, a 6525 ± 111 years B.P. age (GK510) was obtained for a charcoal in silts ∼1 m beneath the modern soil on the surface of T2 north of the main fault trace (Table 1 and Figure 20). A younger age of 5451 ± 126 years B.P. was obtained for the deepest charcoal (also ∼1 m below the soil) found in a shepherd shelter dug into silts south of the fault scarp. Thin peat layers above yielded the youngest ^{14}C ages at Huermo Bulak (820−145 years B.P., Table 1). Finally, one charcoal (EAK00-9) found in laminated silts at a depth of ∼60 cm below the surface of T1, south of the fault, on the left bank of the river, yielded a calibrated age of 1947 ± 49 years B.P. (Table 1 and Figure 20).

[36] Twenty-three quartz cobbles were collected for cosmogenic dating on well-paved patches of the T1 (2 samples), T2 (11 samples), and T3 (10 samples) terraces surfaces south of the fault. Nine subsurface T2 samples were also collected from a depth profile upstream from the fault, by rejuvenating the T2/T0 riser (Figure 20). All but six of the cobbles yielded concordant ^{10}Be and $^{26}A1$ surface exposure and depth-corrected model ages (Table 4 and Figure 20). The only cobble with concordant ^{26}Al and ^{10}Be ages on T1 has an ^{10}Be model age of 3.2 ± 0.3 ka (AKE1-2), older than the 1.9 ka ^{14}C age found in the silts that locally cover the terrace surface near the fault scarp. The relative ages are consistent with the abandonment/emplacement scenario observed at Aksay.

[37] Concordant ^{26}Al and ^{10}Be age surface cobbles on T2 have ^{10}Be model ages between 5.2 ± 0.8 and 13.9 ± 1.0 ka. The younger T2 ^{10}Be model ages are in good agreement with the ^{14}C constraints and the distribution of ages is virtually identical to that of the T2 surface at Aksay. The youngest depth-corrected age (DAK3-100, ∼9.5.ka) approaches the age of the youngest surface samples and place a maximum bound on the age of the surface. The remaining samples skew to much older depth-corrected ages and could plausibly have been derived from remnant patches of T3 or even older terraces (T4) farther upstream (Table 4). The T3 surface is clearly older than T2. With the exception of two younger samples (AT23.2, 6.1 ± 0.5 ka and AT23.5, 26.5 ± 1.8 ka), which may have been carried and deposited upon the terrace surface by the rills that incise the basement beneath T4 (Figure 12), all the other cobbles (8) have exposure ages between 37.9 ± 2.8 and 60.6 ± 4.5 ka. These cobbles display a somewhat bimodal age distribution, with five younger samples between 37.9 and 43.3 ka, and three older samples between 50.7 and 60.6 ka (Table 4).

[38] Although our sampling at Huermo Bulak was less extensive than at Aksay, the combined ^{14}C and ^{10}Be-^{26}Al results we obtain imply similar histories of emplacement and abandonment of the similar terrace levels (Figure 20). In fact, the emplacement and abandonment of T1 and of T2 appear to have been coeval at both sites. Though based on only two samples at Huermo Bulak, the inference that T1 was emplaced mostly between 4 and 2 ka, as at Aksay (5.5 to 2.2 ka) is plausible. For T2, the evidence is stronger, and, as at Aksay, the T2 terrace was probably abandoned after 6.5 ± 0.9 ka, on the basis of the self-consistency of the youngest exposure ages of surface cobbles and ^{14}C ages of charcoal in subsurface layers. The oldest ^{10}Be ages on T2, 13.9 ka, suggest an onset of emplacement coeval with that at Aksay. Finally, the T3 terrace level dated at Huermo Bulak clearly predates the emplacement of T2 and the LGM. Further sampling would be needed to assess its exact relationship with climate change, but the results at hand are consistent with emplacement during the warm and humid interstadials at 35 and 55 ka that bound the 45 ka glacial maximum coeval with marine isotope stage 3 [*Thompson et al.*, 1997].

4.3. Bang Guo Ba

[39] We retrieved relatively shallow (∼50−100 cm deep) charcoal fragments from silt layers beneath modern soils in two areas only, none unfortunately beneath gravel layers on T2 or T3′. Ten charcoals found in a north flowing channel incised into T3 and T2 and following mostly the base of the T3 riser west of the Bang guo ba river were dated (Table 1 and Figure 16). The oldest calibrated ages are 2438 ± 317 years B.P. (BGB98-11) and 2528 ± 174 years B.P. (BGB00-6), comparable to the age of T1 at the other sites, and consistent with the observation that this channel is incised in T2 (Figures 17a and 21). Other charcoals were found south of the 20-m-high riser bounding the southwest corner of the T3′ prong, east of Sb1. Three of them (BGB98-1,2,3) from a stream-cut face in T1 along the fault, yielded nearly identical ages (1476 ± 35 years B.P., Table 1). Three others, deeper within a seismic pressure ridge, provided older ages, ranging from 5.8 to 4 ka, implying exhumation by folding of T2 deposits buried beneath T1. Finally, one small charcoal piece found atop a reddish paleosoil capping gravels 1.5 m below the surface of T3′ yielded an age of 4.6 ± 0.2 ka (Table 1), a value unfortunately too young to bear on the age of that terrace (Figure 16).

Table 2. Cosmogenic Age Determinations at Old Aksay

Sample	Measured ^{10}Be,[a] 10^6 atoms/gSiO2	Measured ^{26}Al,[a] 10^6 atoms/gSiO2	Depth,[b] cm	Model Age,[c] kyr		Average, kyr	Ratio ^{26}Al/^{10}Be
				^{10}Be	^{26}Al		
			River Bed Sa1				
AT02-1	0.09 ± 0.01	0.55 ± 0.03	0(1)	2.36 ± 0.24	2.49 ± 0.19	2.43 ± 0.31	1.06 ± 0.10
AT02-2	0.15 ± 0.01	0.92 ± 0.05	0(1)	4.13 ± 0.38	4.19 ± 0.35	4.16 ± 0.52	1.01 ± 0.09
AT02-3	2.20 ± 0.05	12.64 ± 0.31	0(1)	60.94 ± 3.97	59.19 ± 3.96	60.07 ± 5.61	0.97 ± 0.03
AT02-4	0.45 ± 0.01	2.54 ± 0.07	0(1)	12.31 ± 0.80	11.64 ± 0.77	11.97 ± 1.11	0.95 ± 0.03
AT02-5	0.20 ± 0.01	1.12 ± 0.04	0(1)	5.54 ± 0.42	5.13 ± 0.35	5.33 ± 0.55	0.93 ± 0.05
AT02-6	0.01 ± 0.005	0.05 ± 0.01	0(1)	0.34 ± 0.13	0.24 ± 0.05		0.70 ± 0.29
AT02-7	0.36 ± 0.01	2.16 ± 0.06	0(1)	9.91 ± 0.69	9.87 ± 0.65	9.89 ± 0.95	1.00 ± 0.04
AT02-8	0.16 ± 0.01	0.94 ± 0.03	0(1)	4.35 ± 0.35	4.31 ± 0.30	4.33 ± 0.46	0.99 ± 0.06
AT02-9	<0.02	0.10 ± 0.02	0(1)	<0.57	0.44 ± 0.07		
AT02-10	<0.02	0.07 ± 0.01	0(1)	<0.60	0.33 ± 0.05		
			T1 Downstream (East of Sa1)				
A T12-1	0.03 ± 0.02	0.20 ± 0.03	0(1)	0.88 ± 0.53	0.91 ± 0.15	0.89 ± 0.56	1.03 ± 0.64
A T12-2	0.02 ± 0.01	0.14 ± 0.01	0(1)	0.65 ± 0.32	0.65 ± 0.07	0.65 ± 0.33	0.99 ± 0.49
A T12-3	0.20 ± 0.01	1.13 ± 0.06	0(1)	5.55 ± 0.49	5.13 ± 0.43	5.34 ± 0.65	0.92 ± 0.08
A T12-4	0.02 ± 0.01	0.13 ± 0.02	0(1)	0.50 ± 0.31	0.61 ± 0.08		1.21 ± 0.74
A T12-5	0.01 ± 0.004	0.03 ± 0.01	0(1)	0.24 ± 0.11	0.15 ± 0.04		0.63 ± 0.31
A T12-6	0.03 ± 0.005	0.11 ± 0.02	0(1)	0.75 ± 0.13	0.51 ± 0.09		0.69 ± 0.16
A T12-9	0.17 ± 0.01	0.77 ± 0.04	0(1)	4.64 ± 0.36	3.49 ± 0.27		0.75 ± 0.05
A T12-10	0.01 ± 0.005	0.07 ± 0.01	0(1)	0.17 ± 0.13	0.33 ± 0.06		1.92 ± 1.47
A T12-11	0.07 ± 0.004	0.37 ± 0.03	0(1)	1.79 ± 0.15	1.66 ± 0.15	1.72 ± 0.22	0.93 ± 0.09
A T12-12	0.08 ± 0.004	0.39 ± 0.02	0(1)	2.09 ± 0.17	1.79 ± 0.15	1.94 ± 0.23	0.86 ± 0.07
A T12-13	0.08 ± 0.004	0.43 ± 0.02	0(1)	2.10 ± 0.17	1.96 ± 0.16	2.03 ± 0.23	0.93 ± 0.07
A T12-14	0.27 ± 0.03	1.16 ± 0.05	0(1)	7.26 ± 0.98	5.27 ± 0.39		0.73 ± 0.09
A T12-15	1.26 ± 0.03	7.45 ± 0.26	0(1)	34.52 ± 2.22	34.27 ± 2.41	34.39 ± 3.28	0.99 ± 0.04
A T12-16	0.51 ± 0.01	4.89 ± 0.14	0(1)	13.86 ± 0.91	22.34 ± 1.50		1.61 ± 0.06
			T1 Upstream (East of Sa1)				
AR-1-10	0.07 ± 0.03	0.28 ± 0.03	0(1)	2.00 ± 0.87	1.24 ± 0.16		0.62 ± 0.28
AR-1-11	0.25 ± 0.01	1.16 ± 0.19	0(1)	6.82 ± 0.54	5.20 ± 0.93		0.76 ± 0.13
AR-1-12	0.09 ± 0.01	0.64 ± 0.06	0(1)	2.51 ± 0.24	2.84 ± 0.32	2.67 ± 0.39	1.13 ± 0.14
AR-1-1	0.34 ± 0.01	2.22 ± 0.08	10(0.84)	10.85 ± 0.72	11.80 ± 0.80	11.33 ± 1.07	1.09 ± 0.05
AR-1-3	0.11 ± 0.01	0.55 ± 0.10	82.5(0.27)	10.83 ± 0.72	9.20 ± 0.71	10.02 ± 1.02	0.85 ± 0.09
AR-1-9	0.42 ± 0.03	2.38 ± 0.30	230(0.03)	348.6 ± 35.0	333.6 ± 46.4	341.1 ± 58.5	0.96 ± 0.03
AR-1-13	0.16 ± 0.01	0.95 ± 0.09	300(0.01)	342.0 ± 42.3	348.3 ± 69.3	345.2 ± 80.8	1.02 ± 0.02
			T2 Downstream (West of Sa2)				
AK1D-1	0.43 ± 0.02	2.48 ± 0.16	0(1)	11.85 ± 0.86	11.46 ± 1.03	11.66 ± 1.35	0.97 ± 0.07
AK1D-2	1.78 ± 0.03	1.98 ± 0.09	0(1)	49.64 ± 3.17	9.14 ± 0.69		0.18 ± 0.01
AK1D-3	0.24 ± 0.01	1.20 ± 0.12	0(1)	6.68 ± 0.51	5.50 ± 0.64	6.09 ± 0.85	0.82 ± 0.09
AK1D-4	0.34 ± 0.01	2.10 ± 0.06	0(1)	9.26 ± 0.61	9.54 ± 0.63	9.40 ± 0.88	1.03 ± 0.04
AK1D-6	0.39 ± 0.01	2.23 ± 0.07	0(1)	10.83 ± 0.76	10.28 ± 0.69	10.56 ± 1.03	0.95 ± 0.04
AK1D-7	0.26 ± 0.01	1.52 ± 0.05	0(1)	7.01 ± 0.51	6.88 ± 0.48	6.95 ± 0.70	0.98 ± 0.05
AK1D-8	0.29 ± 0.01	1.61 ± 0.08	0(1)	8.11 ± 0.55	7.43 ± 0.58	7.77 ± 0.80	0.92 ± 0.05
AK1D-9	0.27 ± 0.01	1.69 ± 0.18	0(1)	7.57 ± 0.58	7.78 ± 0.95	7.68 ± 1.10	1.03 ± 0.12
AK1D-10	0.28 ± 0.01	1.88 ± 0.10	0(1)	7.53 ± 0.51	8.53 ± 0.70	8.03 ± 0.85	1.13 ± 0.07
			T2 and T2′ Downstream (West of Sa1)				
AK2D-1	3.01 ± 0.08	22.74 ± 1.17	0(1)	82.29 ± 5.56	107.03 ± 8.90		1.30 ± 0.08
AK2D-2	0.25 ± 0.01	1.67 ± 0.15	0(1)	6.91 ± 0.46	7.59 ± 0.84	7.25 ± 0.94	1.10 ± 0.11
AK2D-3	2.28 ± 0.06	14.25 ± 0.64	0(1)	61.84 ± 4.15	65.73 ± 5.08	63.78 ± 6.53	1.06 ± 0.06
AK2D-4	2.31 ± 0.06	13.21 ± 0.42	0(1)	62.72 ± 4.21	60.78 ± 4.25	61.75 ± 5.98	0.97 ± 0.04
			T2 Upstream (West of Sa5)				
AK98-33	0.30 ± 0.01	1.47 ± 0.10	0(1)	8.04 ± 0.56	6.70 ± 0.62	7.37 ± 0.85	0.83 ± 0.06
AK98-34	0.43 ± 0.02	2.22 ± 0.10	0(1)	11.85 ± 0.91	10.13 ± 0.76	10.99 ± 1.18	0.85 ± 0.06
AK98-35	0.77 ± 0.04	4.29 ± 0.15	0(1)	21.12 ± 1.72	19.63 ± 1.37	20.37 ± 2.19	0.93 ± 0.06
AK98-36	0.23 ± 0.01	1.14 ± 0.05	0(1)	6.23 ± 0.46	5.17 ± 0.38	5.70 ± 0.60	0.83 ± 0.05
AK98-37	0.28 ± 0.01	1.61 ± 0.07	0(1)	7.62 ± 0.53	7.31 ± 0.54	7.47 ± 0.76	0.96 ± 0.05
AK98-38	0.51 ± 0.01	2.48 ± 0.10	0(1)	13.85 ± 0.93	11.32 ± 0.81	12.58 ± 1.23	0.82 ± 0.04
			T2 Upstream (West of Sa2)				
AK2U-1	1.44 ± 0.05	8.66 ± 0.28	0(1)	38.86 ± 2.69	39.44 ± 2.74	39.15 ± 3.84	1.01 ± 0.05
AK2U-2	0.62 ± 0.01	3.77 ± 0.12	0(1)	16.80 ± 1.07	16.98 ± 1.17	16.89 ± 1.58	1.01 ± 0.04

Table 2. (continued)

Sample	Measured ^{10}Be,[a] 10^6 atoms/gSiO2	Measured ^{26}Al,[a] 10^6 atoms/gSiO2	Depth,[b] cm	Model Age,[c] kyr ^{10}Be	Model Age,[c] kyr ^{26}Al	Average, kyr	Ratio ^{26}Al/^{10}Be
AK2U-3	1.74 ± 0.07	10.77 ± 0.49	0(1)	47.18 ± 3.38	49.26 ± 3.81	48.22 ± 5.09	1.04 ± 0.06
AK2U-5	0.36 ± 0.02	2.33 ± 0.12	0(1)	9.54 ± 0.72	10.44 ± 0.82	9.99 ± 1.08	1.09 ± 0.07
AK2U-6	0.12 ± 0.02	0.56 ± 0.05	0(1)	3.30 ± 0.61	2.51 ± 0.26		0.76 ± 0.15

[a]Propagated analytical uncertainties include error blank, carrier and counting statistics.
[b]Depth correction beneath flat surface, between brackets, has been calculated considering attenuation of flux coming from all azimuthal directions, where intensity of flux at depth is $I(x) = I(0)\exp(-\mu L(x))$, attenuation is $\mu = \rho/\Lambda$, and distance through matter is $L(x) = x/\sin(\theta)$, θ being inclination of incoming radiation. A density $\rho = 2.1$ g/cm^3 and attenuation length $\Lambda = 175$ g/cm^2 have been used.
[c]Zero erosion model ages are calculated with propagated analytical uncertainties including 6% uncertainty on production rate [*Stone*, 2000], and 3.3 and 2.8% uncertainties for decay constants of ^{10}Be and ^{26}Al, respectively [*Gosse and Phillips*, 2001], as well as uncertainty of 10% on density and attenuation length for depth samples.

[40] Eighteen embedded quartz cobbles were collected from the smooth, well-paved surface of T2 south of Bang guo ba, and two from the crest of the T3′ spur to the west. In addition, seven subsurface samples were collected from the rejuvenated T2/T0 riser on the west bank of the Bang guo ba river, and from an irrigation trench freshly dug into T2 (Figures 16 and 17). Fourteen of the surface samples yielded concordant ^{10}Be and ^{26}A1 model ages (Table 5 and Figure 21). If we eliminate the two oldest ^{10}Be ages (AT11-I and AT11-N) for which we do not have ^{26}Al

Table 3. Cosmogenic Age Determinations at Huermo Bulak

Sample	Measured ^{10}Be,[a] 10^6 atoms/g SiO_2	Measured ^{26}Al,[a] 10^6 atoms/g SiO_2	Depth,[b] cm	Model Age,[c] kyr ^{10}Be	Model Age,[c] kyr ^{26}Al	Average, kyr	Ratio ^{26}Al/^{10}Be
			T1				
AKE1-1	0.87 ± 0.02	7.02 ± 0.83	0(1.00)	20.81 ± 1.36	28.11 ± 3.77		1.35 ± 0.16
AKE1-2	0.13 ± 0.01	0.94 ± 0.06	0(1.00)	3.21 ± 0.26	3.73 ± 0.34	3.47 ± 0.42	1.16 ± 0.10
			T2				
AT13.1	0.38 ± 0.01	2.13 ± 0.08	0(1.00)	9.15 ± 0.64	8.61 ± 0.61	8.88 ± 0.88	0.94 ± 0.05
AT13.2	0.22 ± 0.03	1.22 ± 0.07	0(1.00)	5.22 ± 0.75	4.87 ± 0.40	5.04 ± 0.84	0.93 ± 0.13
AT13.3	0.25 ± 0.04	NM	0(1.00)	5.90 ± 0.91			
AT13.4	0.58 ± 0.02	3.07 ± 0.12	0(1.00)	13.89 ± 0.99	12.25 ± 0.87	13.07 ± 1.32	0.88 ± 0.05
AT13.5	0.28 ± 0.01	1.55 ± 0.08	0(1.00)	6.67 ± 0.53	6.18 ± 0.50	6.42 ± 0.73	0.93 ± 0.07
AT13.6	0.22 ± 0.02	1.47 ± 0.07	0(1.00)	5.20 ± 0.58	5.84 ± 0.46	5.52 ± 0.75	1.12 ± 0.12
AT13.8	0.19 ± 0.01	1.65 ± 0.08	0(1.00)	4.42 ± 0.40	6.57 ± 0.52		1.48 ± 0.13
AT13.9	0.56 ± 0.02	3.10 ± 0.13	0(1.00)	13.28 ± 0.95	12.31 ± 0.90	12.80 ± 1.31	0.93 ± 0.05
AT13.10	0.09 ± 0.03	NM	0(1.00)	2.21 ± 0.62			
AKE1′-1	0.30 ± 0.01	1.92 ± 0.18	0(1.00)	7.15 ± 0.49	7.69 ± 0.86	7.42 ± 0.97	1.08 ± 0.11
AKE1′-3	0.27 ± 0.01	1.60 ± 0.11	0(1.00)	6.53 ± 0.47	6.41 ± 0.58	6.47 ± 0.75	0.98 ± 0.08
			T2 Depth Profile				
DAK3-50	0.28 ± 0.02	1.44 ± 0.13	50(0.44)	14.90 ± 0.97	12.72 ± 0.92	13.81 ± 1.34	0.85 ± 0.06
DAK3-95B	0.33 ± 0.12	0.42 ± 0.58	95(0.22)	34.76 ± 3.61	7.32 ± 2.33		0.21 ± 0.15
DAK3-100	0.08 ± 0.01	0.52 ± 0.04	100(0.21)	9.46 ± 0.66	9.73 ± 0.63	9.59 ± 0.92	1.03 ± 0.08
DAK3-115	0.34 ± 0.01	1.86 ± 0.07	115(0.17)	48.08 ± 3.16	43.75 ± 2.94	45.91 ± 4.32	0.91 ± 0.02
DAK3-120	0.12 ± 0.02	0.74 ± 0.14	120(0.15)	18.25 ± 1.32	18.71 ± 1.34	18.48 ± 1.88	1.03 ± 0.11
DAK3-130	0.44 ± 0.02	2.10 ± 0.25	130(0.13)	76.79 ± 5.24	61.74 ± 4.44	69.26 ± 6.87	0.80 ± 0.04
DAK3-160	0.08 ± 0.01	0.40 ± 0.05	160(0.09)	20.37 ± 1.43	17.85 ± 1.27	19.11 ± 1.91	0.88 ± 0.05
DAK3-200	0.03 ± 0.003	0.30 ± 0.07	200(0.05)	13.31 ± 1.00	24.22 ± 1.88		1.82 ± 0.11
DAK3-230	0.15 ± 0.01	0.87 ± 0.07	230(0.03)	111.03 ± 9.4	105.76 ± 9.7	108.40 ± 13.6	0.95 ± 0.02
			T3				
AT23.1	1.73 ± 0.07	9.12 ± 0.37	0(1.00)	41.25 ± 2.97	36.66 ± 2.69	38.96 ± 4.01	0.89 ± 0.05
AT23.2	0.26 ± 0.02	1.52 ± 0.06	0(1.00)	6.10 ± 0.54	5.98 ± 0.44	6.04 ± 0.70	0.98 ± 0.08
AT23.3	1.76 ± 0.06	10.00 ± 0.40	0(1.00)	42.01 ± 2.97	40.27 ± 2.96	41.14 ± 4.20	0.96 ± 0.05
AT23.4	1.71 ± 0.05	8.78 ± 0.38	0(1.00)	40.95 ± 2.77	35.24 ± 2.64	38.09 ± 3.84	0.86 ± 0.04
AT23.5	1.11 ± 0.03	6.34 ± 0.18	0(1.00)	26.52 ± 1.79	25.40 ± 1.71	25.96 ± 2.47	0.96 ± 0.04
AT23.6	1.58 ± 0.06	8.93 ± 0.25	0(1.00)	37.90 ± 2.75	36.10 ± 2.43	37.00 ± 3.67	0.95 ± 0.05
AT23.7	2.26 ± 0.08	12.80 ± 0.55	0(1.00)	54.68 ± 3.88	52.29 ± 3.97	53.48 ± 5.56	0.96 ± 0.05
AT23.8	1.80 ± 0.05	10.02 ± 0.27	0(1.00)	43.33 ± 2.86	40.73 ± 2.73	42.03 ± 3.95	0.94 ± 0.03
AT23.9	2.09 ± 0.05	11.60 ± 0.34	0(1.00)	50.66 ± 3.35	47.42 ± 3.25	49.04 ± 4.67	0.94 ± 0.04
AT23.10	2.49 ± 0.10	12.40 ± 0.35	0(1.00)	60.57 ± 4.45	50.81 ± 3.45	55.69 ± 5.57	0.84 ± 0.04

[a]Propagated analytical uncertainties include error blank, carrier and counting statistics. NM indicates no measure.
[b]Depth correction beneath flat surface, between brackets, has been calculated considering attenuation of flux coming from all azimuthal directions, where intensity of flux at depth is $I(x) = I(0).\exp(-\mu L(x))$, attenuation is $\mu = \rho/\Lambda$, and distance through matter is $L(x) = x/\sin(\theta)$, θ being inclination of incoming radiation. A density $\rho = 2.1$ g/cm^3 and attenuation length $\Lambda = 175$ g/cm^2 have been used.
[c]Zero erosion model ages are calculated with propagated analytical uncertainties including 6% uncertainty on production rate [*Stone*, 2000] and 3.3 and 2.8% uncertainties for decay constants of ^{10}Be and ^{26}Al, respectively [*Gosse and Phillips*, 2001], as well as uncertainty of 10% on density and attenuation length for depth samples.

Table 4. Cosmogenic Age Determinations at Bang Guo Ba

Sample	Measured ^{10}Be,[a] 10^6 atoms/g SiO_2	Measured ^{26}Al,[a] 10^6 atoms/g SiO_2	Depth,[b] cm	Model Age,[c] kyr		Average, kyr	Ratio ^{26}Al/^{10}Be
				^{10}Be	^{26}Al		
			T2				
A T11-A	0.25 ± 0.02	1.29 ± 0.05	0(1.00)	6.12 ± 0.54	5.18 ± 0.38	5.65 ± 0.65	0.85 ± 0.07
A T11-E	0.43 ± 0.05	2.37 ± 0.12	0(1.00)	10.23 ± 1.34	9.53 ± 0.76	9.88 ± 1.52	0.93 ± 0.12
A T11-F	0.27 ± 0.02	1.51 ± 0.19	0(1.00)	6.47 ± 0.53	6.03 ± 0.86	6.25 ± 1.03	0.93 ± 0.13
A T11-H	0.21 ± 0.02	1.13 ± 0.07	0(1.00)	5.15 ± 0.49	4.51 ± 0.39	4.83 ± 0.62	0.88 ± 0.08
A T11-I	1.68 ± 0.37	N.M	0(1.00)	40.59 ± 9.38			
A T11-N	1.20 ± 0.27	N.M	0(1.00)	29.07 ± 6.72			
AT11-C	0.22 ± 0.01	1.32 ± 0.20	0(1.00)	5.30 ± 0.43	5.30 ± 0.88	5.30 ± 0.98	1.00 ± 0.16
AT11-G	0.20 ± 0.01	1.28 ± 0.15	0(1.00)	4.80 ± 0.35	5.14 ± 0.68	4.97 ± 0.75	1.07 ± 0.13
AT11-J	0.31 ± 0.01	1.77 ± 0.11	0(1.00)	7.55 ± 0.52	7.10 ± 0.62	7.32 ± 0.82	0.94 ± 0.07
AT11-L	0.37 ± 0.04	1.15 ± 0.14	0(1.00)	8.80 ± 1.08	4.60 ± 0.63		0.52 ± 0.08
BGB-7	0.20 ± 0.01	1.59 ± 0.06	0(1.00)	4.97 ± 0.35	6.49 ± 0.47		1.31 ± 0.07
BGB-8	0.32 ± 0.01	1.51 ± 0.71	0(1.00)	7.98 ± 0.50	6.34 ± 0.48	7.16 ± 0.71	0.80 ± 0.37
BGB-9	0.22 ± 0.005	1.27 ± 0.05	0(1.00)	5.24 ± 0.33	5.08 ± 0.38	5.16 ± 0.50	0.97 ± 0.05
BGB-10	0.16 ± 0.004	0.88 ± 0.04	0(1.00)	4.15 ± 0.27	3.70 ± 0.29	3.93 ± 0.39	0.89 ± 0.05
BGB-11	0.30 ± 0.01	1.65 ± 0.07	0(1.00)	7.16 ± 0.45	6.60 ± 0.48	6.88 ± 0.66	0.92 ± 0.04
BGB-12	0.32 ± 0.01	1.86 ± 0.07	0(1.00)	7.80 ± 0.49	7.49 ± 0.53	7.65 ± 0.72	0.96 ± 0.04
BGB-13	0.17 ± 0.01	0.99 ± 0.06	0(1.00)	4.12 ± 0.28	4.12 ± 0.34	4.12 ± 0.44	1.00 ± 0.06
BGB-14	0.20 ± 0.01	1.14 ± 0.05	0(1.00)	4.97 ± 0.36	4.61 ± 0.34	4.79 ± 0.49	0.93 ± 0.05
			T2 Depth Profile				
BGB-15	0.17 ± 0.005	0.97 ± 0.04	80(0.28)	14.37 ± 0.89	14.07 ± 0.89	14.22 ± 1.26	0.98 ± 0.03
BGB-16	0.05 ± 0.003	0.34 ± 0.05	140(0.12)	11.47 ± 0.77	11.77 ± 0.82	11.62 ± 1.12	1.03 ± 0.06
BGB-17	0.10 ± 0.003	0.60 ± 0.03	150(0.10)	25.52 ± 1.75	24.14 ± 1.68	24.83 ± 2.43	0.95 ± 0.02
AR11-3	0.16 ± 0.01	0.93 ± 0.04	170(0.07)	51.70 ± 3.74	49.59 ± 3.69	50.64 ± 5.25	0.96 ± 0.02
BGB-18	0.19 ± 0.01	1.09 ± 0.04	210(0.04)	109.39 ± 8.87	104.14 ± 9.07	106.76 ± 12.71	0.95 ± 0.01
AR11-2	0.11 ± 0.01	0.12 ± 0.02	240(0.03)	96.81 ± 8.36	17.35 ± 1.44		0.18 ± 0.01
AR11-1	0.02 ± 0.01	0.48 ± 0.05	340(0.01)	59.23 ± 6.42	273.96 ± 52.62		4.63 ± 0.25
			T3				
BGB-2	2.30 ± 0.10	1.28 ± 0.51	0(1.00)	55.84 ± 4.20	52.56 ± 3.88	54.20 ± 5.71	0.94 ± 0.06
BGB-4	1.24 ± 0.02	0.72 ± 0.27	0(1.00)	29.83 ± 1.89	29.21 ± 2.09	29.53 ± 2.83	0.98 ± 0.04

[a]Propagated analytical uncertainties include error blank, carrier and counting statistics. N.M means no measure.

[b]Depth correction beneath flat surface, between brackets, has been calculated considering attenuation of flux coming from all azimuthal directions, where intensity of flux at depth is $I(x) = I(0).\exp(-\mu L(x))$, attenuation is $\mu = \rho/\Lambda$, and distance through matter is $L(x) = x/\sin(\theta)$, θ being inclination of incoming radiation. A density $\rho = 2.1$ g/cm^3 and attenuation length $\Lambda = 175$ g/cm^2 have been used.

[c]Zero erosion model ages are calculated with propagated analytical uncertainties including 6% uncertainty on production rate [*Stone*, 2000], and 3.3 and 2.8% uncertainties for decay constants of ^{10}Be and ^{26}Al, respectively [*Gosse and Phillips*, 2001], as well as uncertainty of 10% on density and attenuation length for depth samples.

results, as outliers, the remaining ^{10}Be ages yield an average age of 6.2 ± 1.7 ka (± 1σ) with minimum and maximum ages of 4.1 ± 0.3 and 10.2 ± 1.3 ka (Figure 21). The depth profile is reminiscent of that at Huermo Bulak, with two ages (11.5 ± 0.8 and 14.4 ± 0.9 ka) close to the oldest exposure age found on the T2 surface (10.2 ± 1.3 ka) and older ages, which likely represent older materials wrested upstream from T3′-T3. The two ages (55.8 and 29.8 ka) found on T3′ are consistent with those of samples from the T3′ terrace at Huermo Bulak (Figure 16). Thus, even though the average ^{10}Be age of T2 is somewhat younger (by ~2 kyr) than the corresponding surfaces at Aksay and Huermo Bulak, surface and depth samples together imply that the emplacement history of the T2 surface at Bang guo ba is similar to that at Huermo Bulak and Aksay and occurred between 14 and 6 ka. With two samples only, T3′ is permissibly coeval with T3-T3′ at Huermo Bulak.

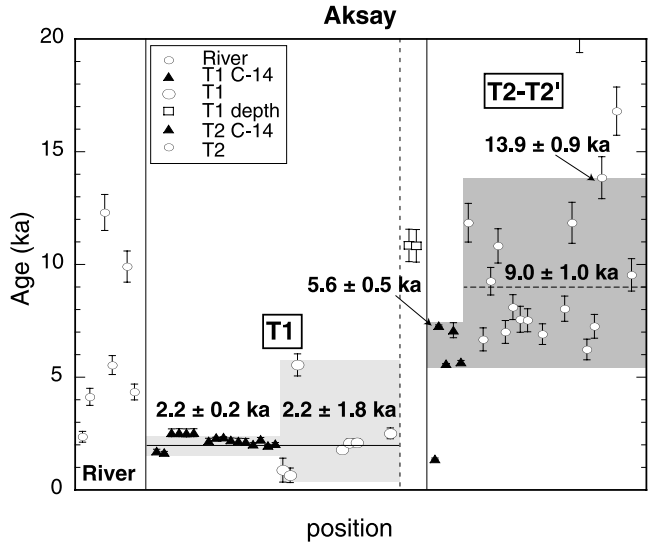

Figure 19. Radiocarbon and surface/subsurface ^{10}Be dating results from Aksay. To improve the resolution in areas of interest, the plot is restricted to ages ≤ 20 ka. Some data plot off scale (see Table 2).

5. Discussion

5.1. Landscape Evolution

[41] It is generally appreciated that incision, deposition and abandonment of fluvial/alluvial terraces is influenced

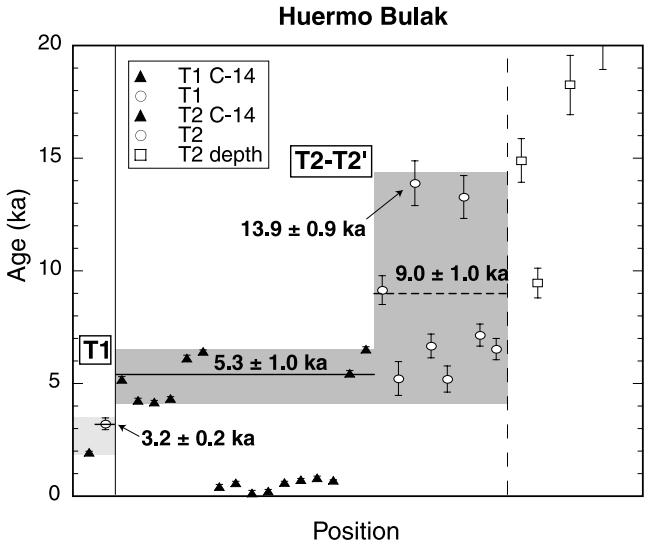

Figure 20. Radiocarbon and surface/subsurface ^{10}Be dating results from Huermo Bulak. Same restriction as in Figure 19 (see Table 3).

by climate change [*Bull*, 1991]. This is especially true in regions that have experienced recent glacial activity in which the coupling of glacial erosion and precipitation modulates the availability of sedimentary material and hydrologic activity. Under such conditions regionally correlative deposition, incision, and abandonment is expected, and should be reflected in the distribution of terrace ages. Similarly, when combined with active strike-slip faulting along the piedmont, clustering of regionally correlative cumulative offsets of terrace risers should be observed. Such regionally correlative terraces ages are best observed in the age populations for T2 at all three sites, and for T1 at Aksay and Bang guo ba (Figure 22). The majority of the surface ages for T2′-T2 (with the exception of a cluster of <1 ka ages at Huermo Bulak) fall between 4 and 14 ka, with the youngest ages constrained by ^{14}C dates. Similarly, T1 ages at Aksay and Bang guo ba are typically <3 ka. The overall distribution of T2′-T2 ages implies virtually continuous deposition since ~14 ka, punctuated by a change in regional hydrologic conditions that caused the abandonment of the T2 surface at ~5 ka. This decrease in fluvial power appears to coincide with the end of the so-called early Holocene optimum (EHO, 9–5 ka), a globally warm and wet period locally documented by fauna and flora records in the detailed analysis of one lake sediment core in northern Tibet (Sumxi Co. [*Gasse et al.*, 1991]). The synchronous emplacement and abandonment of terraces along the Aksay-Bang guo ba stretch of the ATF strongly suggests that their emplacement and abandonment was modulated by variations in global climate.

[42] One shortcoming of our data is the inability to quantitatively separate the emplacement-abandonment chronologies of T2 and T2′, largely due to the absence of datable radiocarbon samples from T2′. In this connection, however, *Van der Woerd et al.* [2001] have dated the terraces uplifted on the hanging wall of the northeast directed Tanghenan Shan thrusts near Subei, 40 km eastward at the end of the Aksay segment of the NATF. Because of rapid incision driven by fast tectonic uplift (4–7 mm/yr) on this active thrust [*Van der Woerd et al.*, 2001], the terrace levels at Subei are well-defined surfaces, with clear vertical separation at very distinct elevations, and are perched ~3 times higher above the active channels than the terraces at Aksay. The much more modest incision rates near Aksay (~1 mm/yr) relative to Subei result in less vertical separation of terrace levels. The ^{14}C ages of the two principal, high-level terraces dated at Subei cluster between 8330 ± 220 and 9485 ± 485 calibrated years B.P. (9 ± 1 ka) and 4410 ± 60 and 4725 ± 35 calibrated years B.P. (4.6 ± 0.3 ka) constraining the abandonment of these terrace surfaces (Figure 23). The 4.6 ka Subei age cluster corresponds roughly with the youngest ^{14}C ages from T2 at Huermo Bulak and Bang guo ba (Figure 23 and Table 1) supporting a regionally contemporaneous abandonment of that surface. Radiocarbon ages corresponding to the 9 ± 1 ka Subei ages have not been observed on the Aksay-Bang guo ba stretch of the fault, but the T2′-T2 ^{10}Be ages clearly encompass this range of ages (Figure 23). The enhanced temporal resolution at Subei thus suggests that the T2′ surface along the Aksay-Bang guo ba stretch of the NATF may have also been abandoned between 8 and 10 ka. The 2–2.5 ka ^{14}C age cluster found in the T1 channels at Aksay and Bang guo ba has no equivalent at Subei because comparably small channels were not sampled. Younger ages between 1700 and 1000 and 600–700 years B.P., however, are typical of low-level terraces (<1.5 m high) in the modern flood channels of streams at Subei (site 3 [*Van der Woerd et al.*, 2001]).

[43] Taken together the distribution of surfaces ages supports the interpretation that a major phase of terrace emplacement along the Dangjin Shankou piedmont was generally concurrent with the warm pluvial following the end of stage 2 (LGM), although fluvial response appears to have been somewhat delayed relative to the Guliya ice core paleotemperature record [*Thompson et al.*, 1997]

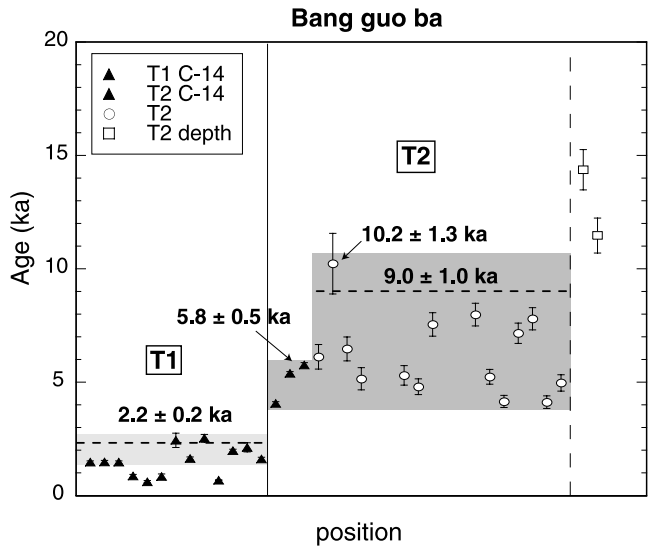

Figure 21. Radiocarbon and surface/subsurface ^{10}Be dating results from Bang guo ba. Same restriction as in Figures 19 and 20 (see Table 4).

Table 5. Offset, Age, and Slip Rate Estimates for Aksay, Huermo Bulak, and Bang Guo Ba[a]

		Strath Abandonment		Strath Emplacement		Fill Abandonment	
Feature	Offset, m	Age, ka	Rate, mm/yr	Age, ka	Rate, mm/yr	Age, ka	Rate, mm/yr
			Aksay				
T3/T2′ riser (R2 left bank)	225 ± 10	9.0 ± 1.0	25.0 ± 3.0	13.9 ± 0.9	**16.2 ± 1.3**	34.5 ± 2.2	6.5 ± 0.5
T3/T2′ riser (R2 right bank)	220 ± 40	9.0 ± 1.0	24.5 ± 5.2	13.9 ± 0.9	**15.8 ± 3.1**	34.5 ± 2.3	6.4 ± 1.2
Riser (R1 left bank)	210 ± 20	9.0 ± 1.0	23.3 ± 3.4	13.9 ± 0.9	**15.1 ± 1.7**	34.5 ± 2.4	6.1 ± 0.7
Riser (R1 right bank)	185 ± 20	9.0 ± 1.0	20.6 ± 3.2	13.9 ± 0.9	**13.3 ± 1.7**	34.5 ± 2.5	5.4 ± 0.7
T2/T1 (Sa1)	145 ± 10	2.2 ± 0.2	65.6 ± 7.5	5.6 ± 0.5	25.9 ± 2.9	6.5 ± 0.8	**22.3 ± 3.1**
T3-T2′/T2 (Sa2)	135 ± 10	6.5 ± 0.8	20.8 ± 3.0	9.0 ± 1.0	**15.0 ± 2.0**	9.0 ± 1.0	**15.0 ± 2.0**
T2′/T2 (Sa1)	165 ± 20	6.5 ± 0.8	25.4 ± 4.4	9.0 ± 1.0	**18.3 ± 3.0**	9.0 ± 1.0	**18.3 ± 3.0**
Sa3	195 ± 20					9.0 ± 1.0	**21.7 ± 3.3**
Sa5-Sa4′	220 ± 20					9.0 ± 1.0	**24.4 ± 3.5**
Sa6-Sa5′	130 ± 10					9.0 ± 1.0	**14.4 ± 2.0**
Sa1	45 ± 5					2.2 ± 0.2	**20.5 ± 2.9**
Sa2	40 ± 5					2.2 ± 0.2	**18.2 ± 2.8**
			Huermo Bulak				
T3/T2′-T2 (west of R3)	225 ± 20	5.3 ± 1.0	42.5 ± 8.9	13.9 ± 1.0	**16.2 ± 1.9**	37.9 ± 2.8	5.9 ± 0.7
Alternative		9.0 ± 1.0	25.0 ± 3.6				
T3/T2′-T2 (F2)	50 + 5					37.9 ± 2.8	1.3 ± 0.2
Combined ATF-F2	275 ± 25	5.3 ± 1.0	51.9 ± 10.9	13.9 ± 1.0	**19.8 ± 2.3**	37.9 ± 2.8	7.3 ± 0.8
ATF-F2 (alternative)	275 ± 50	9.0 ± 1.0	30.6 ± 4.4				
T2/T1	105 ± 10	2.2 ± 0.2	47.7 ± 6.3	3.2 ± 0.3	32.8 ± 4.4	5.3 ± 1.0	**19.8 ± 4.2**
	20 ± 5					5.3 ± 1.0	3.8 ± 1.2
Combined ATF-F2, T2/T1	125 ± 15	2.2 ± 0.2	56.8 ± 8.6	3.2 ± 0.3	39.1 ± 5.9	5.3 ± 1.0	**23.6 ± 5.3**
T2/T1 (east of Sh3)	110 ± 10	2.2 ± 0.2	50.0 ± 6.4	3.2 ± 0.3	34.3 ± 3.8	5.3 ± 1.0	**20.8 ± 4.3**
T1/T0″ (west of R3)	60 ± 5					2.2 ± 0.2	27.3 ± 3.4
Alternative							
Sh1	95 ± 10					5.3 ± 1.0	**17.9 ± 3.9**
Sh2	45 ± 5					2.2 ± 0.2	**20.5 ± 2.9**
T2/T0 (west of Sh3)	45 ± 5					2.2 ± 0.2	**20.5 ± 2.9**
T3′ (between R3 and Sh3)	800 ± 80					37.9 ± 2.8	**21.1 ± 2.6**
			Bang Guo Ba				
T3′/T2′ (west of Sb1)	260 ± 30	9.0 ± 1.0	28.9 ± 7.4	13.9 ± 0.9	**18.7 ± 4.5**	29.2 ± 2.1	8.9 ± 2.2
T2′/T2 (west of Sb1)	165 ± 20	5.8 ± 0.1	28.4 ± 3.5	9.0 ± 1.0	**18.3 ± 3.0**	9.0 ± 1.0	**18.3 ± 3.0**
T3 edge (east of Sb1)	240 ± 20	5.8 ± 0.1	41.1 ± 3.5	10.2 ± 1.3	23.5 ± 3.6	29.2 ± 2.1	8.2 ± 0.9
Alternative				13.9 ± 0.9	**17.3 ± 1.8**		
T3 edge (east of R4)	240 ± 20	5.8 ± 0.1	41.1 ± 3.5	10.2 ± 1.3	23.5 ± 3.6	29.2 ± 2.1	8.2 ± 0.9
Alternative				13.9 ± 0.9	**17.3 ± 1.8**		
T2′/T2 (east of R4)	165 ± 20	5.8 ± 0.1	28.4 ± 3.5	9.0 ± 1.0	**18.3 ± 3.0**	9.0 ± 1.0	**18.3 ± 3.0**
T3/T2′ (east of Sb2)	215 ± 20	10.2 ± 1.3	21.1 ± 3.3	13.9 ± 0.9	**15.5 ± 1.8**	29.2 ± 2.1	7.4 ± 0.9
Alternative		9.0 ± 1.0	23.9 ± 3.5				
T3/T2′ (west of Sb2)	205 ± 20	10.2 ± 1.3	20.1 ± 3.2	13.9 ± 0.9	**14.7 ± 1.7**	29.2 ± 2.1	7.0 ± 0.9
Alternative		9.0 ± 1.0	22.8 ± 3.4				
T2′/T2 (west of Sb2)	165 ± 20	5.8 ± 0.1	28.4 ± 3.5	9.0 ± 1.0	**18.3 ± 3.0**	9.0 ± 1.0	**18.3 ± 3.0**
Channel into T2 (right bank R4)	36 ± 3					5.8 ± 0.1	6.2 ± 0.5
Channel into T1 (east of Sb1)	20 ± 2					1.5 ± 0.1	**13.1 ± 1.6**
Averages			33.2 ± 13.3		20.8 ± 7.1		14.2 ± 7.1

[a]Errors on individual sample ages are obtained by propagating the standard deviation from the ^{10}Be concentration distribution for a population of samples and the 6% uncertainty on production rate [*Stone*, 2000], and 3.3 and 2.8% uncertainties for decay constants of ^{10}Be and ^{26}Al, respectively [*Gosse and Phillips*, 2001]. Error is 1σ for the population of ^{14}C samples averaged at Aksay and Huermo bulak. Errors on the slip rate are obtained by propagating the error on the offset and age in quadrature. Error is 1σ for the average of the different slip rate models. Bold values are selected values plotted in Figure 28 (see text for details).

(Figures 23 and 24) and may not have been strictly coeval from valley to valley (Figures 19, 20, and 21). The bulk of the ages demonstrates that the T2′-T2 terrace complex was emplaced between ~14 and 5 ka. It is plausible that T2′ emplacement took place between 14 and 9 ± 1 ka, followed by the incision and the beginning of T2 emplacement at 9 ± 1 ka. The emplacement of T2 took place during the height of the pluvial and of the fluvial discharge, apparently coinciding with the EHO. At the end of this period, reduction in precipitation and bed load may have led to an inability to maintain a broad river bed resulting in channeled flow, increased incision and abandonment of T2.

[44] The regional nature of post-LGM terrace emplacement is not restricted to the Aksay segment of the NATF. Terrace abandonment in roughly the same time period has been observed elsewhere along the northern border of Tibet, near Tura [*Mériaux et al.*, 2004] and within the Karakax Valley [*Ryerson et al.*, 1999], indicative of the broad extent of this climatic modulation of landscape evolution. The majority of surface ages (both cosmogenic and ^{14}C) determined in this and in previous work by our group along the Kunlun fault [*Van der Woerd et al.*, 1998, 2000, 2002b] and along the central segment of the ATF near Tura [*Mériaux et al.*, 2004] postdate the LGM (18.5 ka) as recorded in

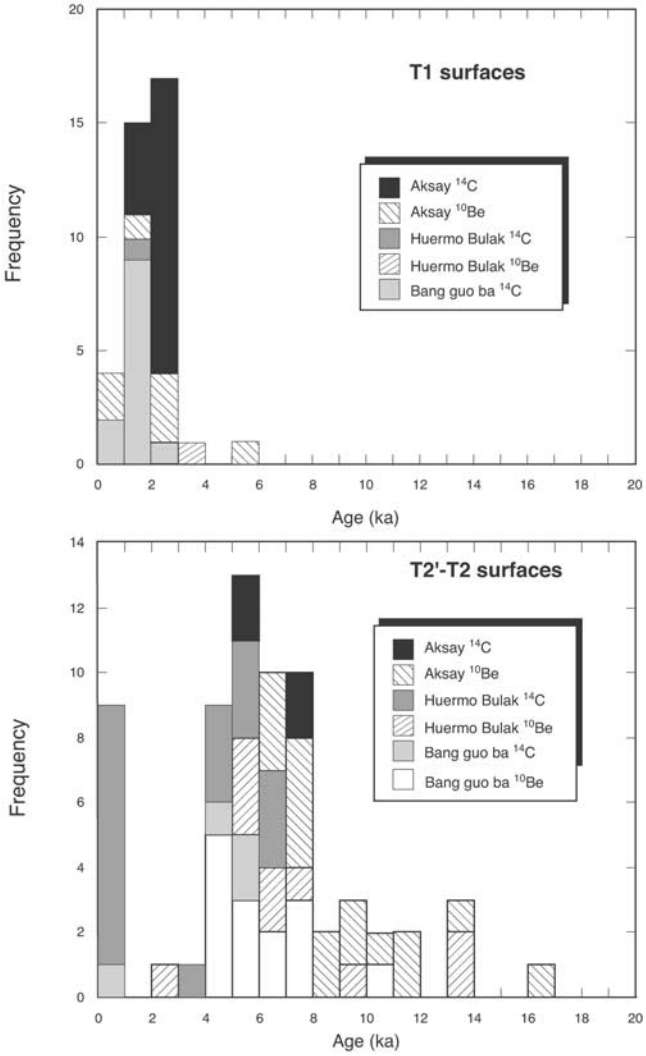

Figure 22. Histogram of radiocarbon and ^{10}Be surface ages on (a) T1 and (b) T2 at Aksay, Huermo Bulak, and Bang guo ba sites.

particular by the Guliya δ^{18}O record (Figure 24). In all cases, the terrace ages were obtained for slip rate determinations, and are intended to constrain the ages of well-preserved offsets. As the best preserved offsets are often the youngest, there is possibly a sampling bias in our data set. Nevertheless, at most places, we sampled most of the visible well-preserved terraces and the preponderance of post-LGM surface ages is overwhelming, in conflict with the suggestion that terrace deposition takes place during glacial maxima due to high sediment supply as a result of active glacial erosion [e.g., *Molnar et al.*, 1994]. Rather, our large data set, together with data from others studies in northern Tibet [*Barnard et al.*, 2004a, 2004b; *Brown et al.*, 2003; *Lasserre et al.*, 1999; *Ritz et al.*, 2003], show that terrace emplacement postdates glacial maxima and is favored by high stream power that can efficiently flush accumulated glacial debris in these short, steep catchments [e.g., *Ballantyne*, 2002].

[45] Although we walked much of the 25 km stretch of the fault from the hills west of Aksay to its junction with the southernmost Taughenan Shan thrust, near Qing shui gou (Figure 3), we measured offsets only near the places we sampled to date the terraces. The more than 30 sinistral offsets plotted in Figure 25 are thus only a fraction of those that might be documented in the course of a more exhaustive study. Nevertheless, even within this small population, distinct groups of offsets are more frequent than others, as expected in a piedmont where sedimentation is punctuated by discrete climatic events [e.g., *Peltzer et al.*, 1988, 1989; *Bull*, 1991; *Avouac et al.*, 1993]. The two clearest peaks in the offset distribution are those corresponding to the narrow, usually cliff-bounded, active stream channels (35–60 m), and to the outer limits of the T2′-T2 fans (200–275 m, Figure 25). Offsets between 90 and 165 m are less numerous and less well expressed in the morphology, although there are examples at Huermo Bulak (90–110 m), Aksay (130–145 m), and Bang guo ba (165 m). To a first order, these differences in offset frequency and prominence are readily accounted for by the overall chronology of terrace emplacement and its correlation with climate change (Figure 24). The prominence of the large (200–275 m) offsets likely results from the fact that the T2′-T2 fans postdate the LGM, while higher-level terraces (T3–T4) predate it. The small offsets (35–60 m) of the active streams ought to be tied up with the current regime of fluvial incision, which likely characterized the latter half of the Holocene. Finally the more modestly expressed intermediate offsets (90–165 m) appear to be associated with risers and/or channels cut into the T2 and T2′ surfaces whose distinction is rarely straightforward.

5.2. A Holocene Slip Rate for the Aksay Segment of the ATF

[46] Millennial slip rates on strike-slip faults can be obtained by combining the horizontal geomorphic offsets, of stream channels and terrace risers, and the surface dating

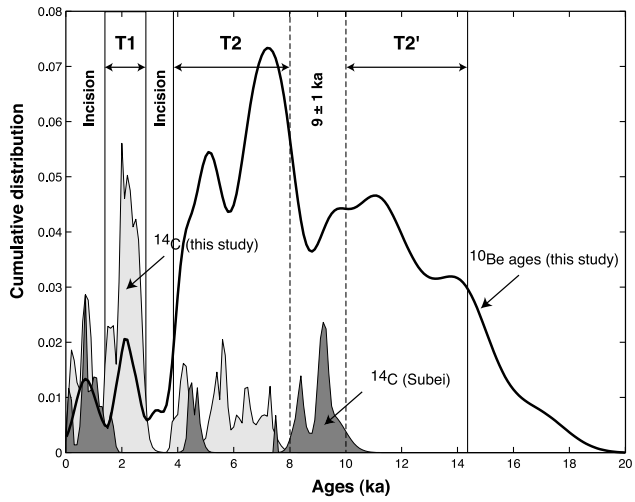

Figure 23. Cumulative distribution of cosmogenic ^{10}Be from the three study sites compared with radiocarbon dates at these sites and at Subei [from *Van der Woerd et al.*, 2001]. Cumulative probability curve is calculated by assessing a Gaussian probability function to each model ages at three sites (Tables 2, 3, and 4) [*Gaudemer et al.*, 1995].

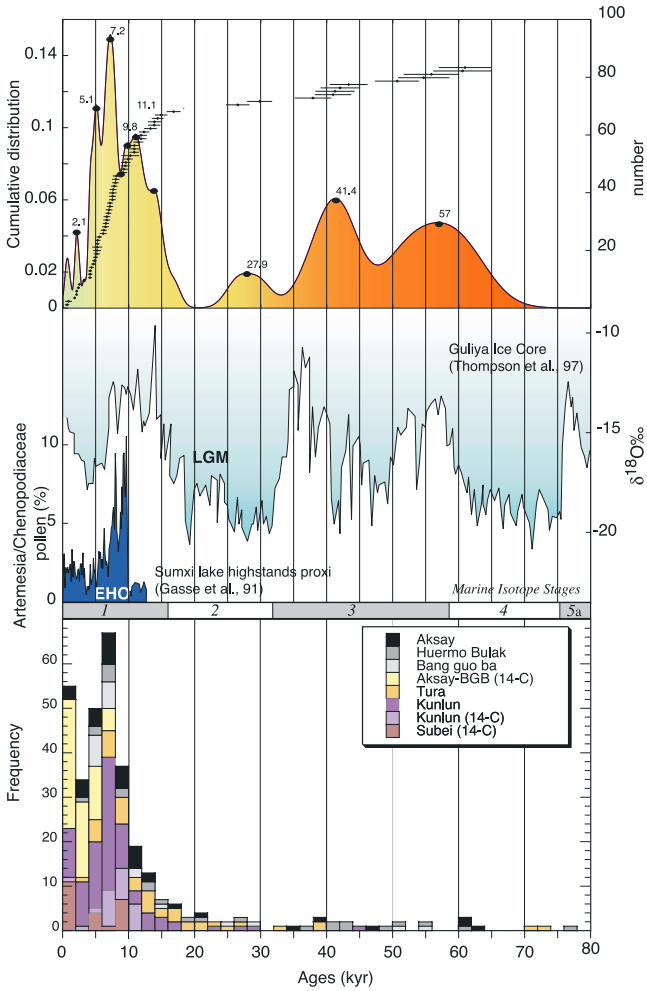

Figure 24. Comparison between SPECMAP marine isotopes ages, $\delta^{18}O$ results from Guliya ice cap (middle frame right axis) [*Thompson et al.*, 1997], regional moisture indicator Artemesia Chenopodiace pollen ratio (middle frame left axis) (from Sumxi Co lake in western Tibet [*Gasse et al.*, 1991]), cumulative distribution of ^{10}Be model ages at Aksay, Huermo Bulak, and Bang guo ba, without outliers at each site (top left axis), Sorted model ages are also plotted with their analytical errors (top right axis) and histogram of surfaces ages (bottom) from this study, Cherchen He near Tura [*Mériaux et al.*, 2004], Kunlun fault [*Van der Woerd et al.*, 2000, 2002b, 1998], and Subei [*Van der Woerd et al.*, 2001].

that constrains the ages of the offsets [e.g., *Sieh and Jahns*, 1984; *Weldon and Sieh*, 1985; *Ritz et al.*, 1995; *Siame et al.*, 1997; *Van der Woerd et al.*, 1998; *Brown et al.*, 2002; *Lasserre et al.*, 2002; *Mériaux et al.*, 2004]. While both the offset measurements and geochronology have uncertainty, the major challenge in determining a geomorphic slip rate is the association of a particular age determination with an observed offset which can potentially lead to much larger errors.

[47] The interpretational framework for determining slip rates based on terrace riser and fluvial channel offsets is illustrated in Figure 26. Here an alluvial surface, T3, deposited atop an active strike-slip fault is subsequently incised and a younger terrace, T2, is emplaced along the active streambed. Ideally, as long as the stream flows at the T2 level, the resulting T3/T2 riser may be continually refreshed by lateral cutting on the sides of the river bed. In this case, T3/T2 only becomes a passive offset marker only when T2 is abandoned because of a new episode of incision, which in turn leads to the formation of the underlying T1 terrace and the T2/T1 riser. The abandonment age of a terrace is typically defined by its youngest surface exposure age and/or the shallowest radiocarbon dates [cf. *Mériaux et al.*, 2004]. Coupling the abandonment of T2 with the overlying riser offset (T3/T2) yields a maximum bracket on the slip rate. We refer to this approximation as the "strath abandonment model," which is relevant to a scenario in which occupation of a terrace level is of short duration and no offset of the riser is accumulated prior to abandonment. In the case where a strath terrace has been occupied by a stream system for a period that is long relative to the earthquake recurrence interval and permanent riser offset is accumulated prior to abandonment, the offset should be linked with the emplacement age of the terrace surface. This may be especially true for surfaces such as those discussed above that were constructed by high energy, ephemeral braided streams where deposition is likely diachronous, with a finite time interval between the initiation of emplacement and abandonment. The emplacement age can be approximated by the oldest exposure age in the surface age distribution, once obvious outliers have been rejected. This "strath emplacement model" yields a relative minimum rate estimate.

[48] Both "strath" models associate the age of the riser with the age of the underlying terrace, but use different

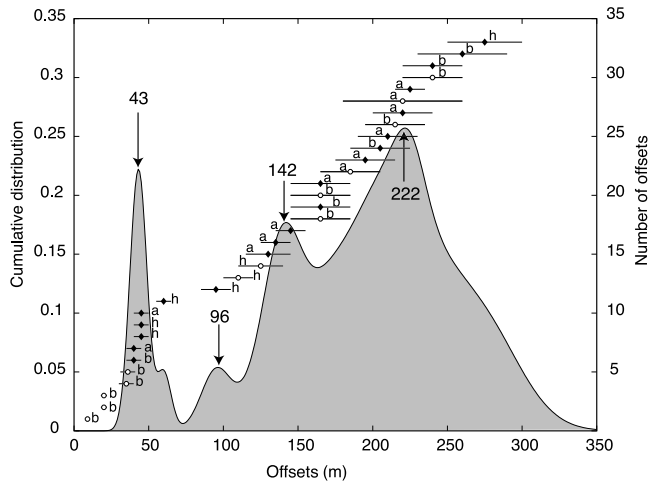

Figure 25. Measured sorted offsets along the Aksay-Bang guo ba stretch of the northern Altyn Tagh fault ranging from 9 ± 1 to 275 ± 25 m (Table 5, exception of no dated 9 ± 1 m offset at Bang guo ba). Location of each measurement is indicated (a, Aksay; h, Huermo Bulak; and b, Bang guo ba). Minimum bound offsets (open symbols) are not included in cumulative distribution in gray. Cumulative probability curve is calculated by assessing a Gaussian probability function to each offset at three sites [*Gaudemer et al.*, 1995].

extremes in the age distribution to bound the rate. An absolute lower bound on the slip rate is obtained by linking a riser offset with the abandonment age of the overlying terrace. This ''fill abandonment model'' is appropriate when the underlying terrace is emplaced, filling a preexisting topography that may include a riser that is already offset by the fault. The age of the underlying terrace would therefore provide an erroneously young age for the riser offset. However, as the riser cannot be older than the terrace into which it was incised, the abandonment age of the upper terrace then yields an minimum approximation of the slip rate. As the chronology of the emplacement/abandonment of terraces can be difficult to assess, one might also use the age of emplacement of the upper surface to characterize the ''fill emplacement model'' as an absolute minimum bound for the rate. However, as it is unlikely that a surface can be emplaced and incised to produce risers and stream channels simultaneously, the fill emplacement model doesn't have any real physical significance and constitutes a virtual, as opposed to real, assessment of the slip rate. The appropriateness of strath as opposed to ''fill'' approximations is based on the geomorphic characterization of the terraces in the field. The fill approximation is useful in determining an absolute minimum rate regardless of the nature of the terraces. Similarly, a ''fill channel model'' is also more generally useful in determining minimum rates from stream channel offsets, such as Sa1 in Figure 6, as the stream channel cannot be older than the surface it incises.

[49] Cosmogenic ages of cobbles from a single terrace often show considerable scatter. This scatter has been generally attributed to factors such as bioturbation and cryoturbation of the surface, postabandonment surface contamination and predepositional exposure or inheritance. The time interval between the initiation of emplacement and abandonment may also add to this scatter. We suspect it to be a general and overlooked factor of cosmogenic exposure age dispersion. The interpretation of such dispersion is always difficult, and there are only a limited number of explicit constraints that can be applied. For instance, comparison with radiocarbon dates from the same location has been used to help constrain the age of abandonment [*Mériaux et al.*, 2004] although radiocarbon dates may also display diachroneity. Subsurface sampling of amalgamated samples has been used to constrain predepositional exposure [*Anderson et al.*, 1996; *Hancock et al.*, 1999; *Repka et al.*, 1997]. The method makes use of the fact that the concentration of a cosmogenic nuclide in a statistically significant sample will be the sum of (1) the average predepositional exposure inventory and (2) that accumulated locally by exposure in the surface of interest. As the concentration of the later component decreases exponentially with depth because production is attenuated by shielding, cosmogenic nuclide concentrations in deep, totally shielded samples reflect only the predepositional exposure inventory. This average inherited component can then be subtracted to yield the exposure concentration and real surface exposure age. It is important to note that the exposure concentration and age obtained in this method is implicitly the abandonment age. The method cannot distinguish predepositional exposure inherited during storage and transport from that accumulated locally prior to abandonment. It therefore yields a minimum age for the surface and, without sampling multiple depth profiles on a particular surface, provides no information on the duration of emplacement. In fact, a finite emplacement interval would result in an overestimate of inheritance. Hence information on emplacement ages must be gleaned from the distribution of single surface cobble ages in concert with subsurface sampling, radiocarbon dating and others techniques. The distribution of cosmogenic ages from individual surface cobbles may be used to define upper and lower brackets on the slip rate, as described above. A depth profile, or the depth-corrected ages of single subsurface cobbles, may be used to more explicitly constrain this estimate. If we assume that all the age dispersion is due to diachronous deposition not inheritance, then the cobble ages, regardless of the interpretational model, provide the maximum age estimate and the corresponding minimum model-dependent rate.

[50] As discussed above, the chronology of terrace formation along the northern Dangjin Shankou piedmont is reasonably consistent among the three sites studied in detail. Terraces T4 and T3 were deposited and abandoned prior to the LGM. On the basis of the youngest T3 ^{10}Be model ages at Huermo Bulak (AT23.5) and Bang guo ba (BGB-4) we infer that T3 was abandoned at ~29 ka. Deposition of the T2′-T2 terraces began following the LGM at ~14 ka, as indicated by the oldest ^{10}Be ages at Aksay and Huermo Bulak. The oldest T2′-T2 surface age at Bang guo ba is 10.2 ka, suggesting that it may be younger than the correlative surfaces at Aksay and Huermo Bulak corresponding chiefly to T2 or that our sampling did not include samples of similar age. The effect of both alternatives upon the derived slip rates is considered below. While T2 and T2′ can be distinguished in the field, our dating cannot resolve the timing of T2′ abandonment and the beginning of T2 emplacement. We infer, on the basis of correlations with the terraces at Subei [*Van der Woerd et al.*, 2001], that T2′ may have been abandoned at 9.0 ± 1.0 ka (Figure 23). As such, scenarios in which T2′ abandonment and T2 emplacement begin at this time are also considered below. Radiocarbon and ^{10}Be constraints indicate that T2 was abandoned between 5.5 and 6.5 ka. Since the surface dating cannot clearly resolve the time interval between the abandonment of T2 and the onset of T1 emplacement, we use as an alternative, the older available ^{10}Be age on T1, which is also younger than the abandonment age of T2 determined at each site. Finally, T1 appears to have been abandoned at approximately 2.2 ka. Using the various emplacement-abandonment models described above, these overall age constraints, specific to each of the sites, have been combined with the observed offsets to obtain slip rate estimates (Table 5).

[51] The two strath models and the fill abandonment models are illustrated with histogram plots in Figure 27. Overall, the slip rates derived from the fill model*s* are lower than those obtained with strath models (Table 5). Similarly, the emplacement estimates are lower than the abandonment models. The average slip rate estimates are 14.2 ± 7.1 mm/yr for the fill abandonment model, and 20.8 ± 7.1 mm/yr for the strath emplacement model. For the strath abandonment model the average is 33.2 ± 13.4 mm/yr. The actual slip rate should be bounded by the fill abandonment and strath emplacement models. Other scenarios in which T2 and T2′ abandonment are not distinguished or in which the

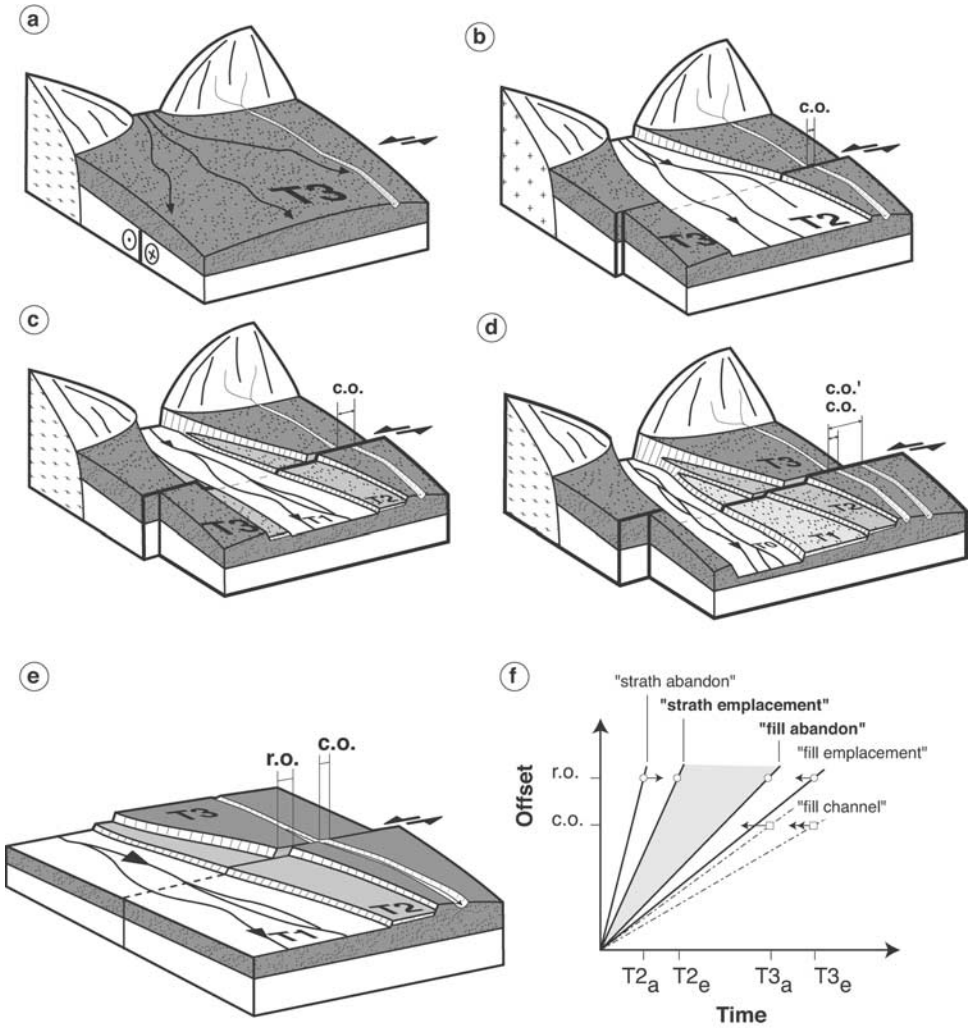

Figure 26. Block diagrams showing schematic sequence of terrace emplacement and river entrenchment disrupted by strike-slip faulting (modified from *Van der Woerd et al.* [2002b]). (a) A large fan (T3) is emplaced at a time of large sedimentary discharge covers fault trace. (b) Following the discharge in Figure 26a, the river incises the T3 surface and occupies younger T2 streambed. A channel incising T3 is offset (c.o.), while the riser T3/T2, refreshed by the active T2 stream, is not offset. (c) During a new episode of entrenchment, T2 is abandoned, and riser T3/T2, now a passive marker, begins to record lateral displacement. If T3/T2 was continually refreshed while the river occupied T2, the abandonment age of T2 can be associated with the T3/T2 riser offset to obtain a slip rate (strath abandonment model). The abandonment age is taken as the youngest surface cosmogenic age or the age of the shallowest radiocarbon date. If offset accumulated prior to abandonment, then the age of T2 emplacement may be a better constraint (strath emplacement model). The onset of emplacement can be approximated by the oldest surface exposure age (once outliers have been eliminated). In the case of strath terraces, a lower bound on the slip rate may be obtained by associating the T3/T2 offset with the abandonment age of T2, as no riser can predate the surface into which it is incised. (d) Successive episodes of terrace beveling and entrenchment of river due to climatic changes lead to the formation of several terraces whose risers are offset differently. (e) Block diagram shows the riser offset (r.o.) and channel offset (c.o.) used in the slip rate diagram in Figure 26f. (f) Different slip rate models are shown for the riser and channel offsets derived from the different age constraints for these offsets and geomorphic evidences (i.e., fill or strath terrace).

beginning of emplacement of the T2′ terrace at Ban guo ba began at 10.2 ka produce only small changes in these rates (Table 6), and the rates above appear to be the best and most conservative estimate. However, since the fill model is clearly a better approximation for fill terraces than for strath terraces and vice versa, these different models must be assessed case by case depending on the type of offset and surface considered. A selection of the different slip rate estimates based on the appropriate geomorphic evidence in each case is listed in bold (Table 5 and Figure 28).

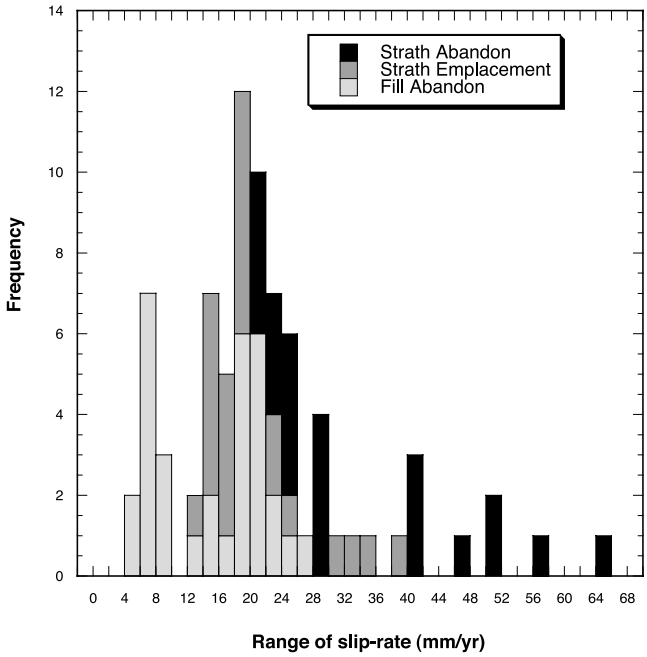

Figure 27. Cumulative histogram of rates along the Aksay-Bang guo ba stretch of the ATF. The data shown are those determined using an age of 13.9 ka for the onset of T2 emplacement at Bang guo ba, as opposed to the younger estimate derived from the oldest ^{10}Be age on that surface, 10.2 ka. The presented rates also assume that the temporal boundary between the abandonment of T2′ and the onset of T2 emplacement was 9.0 ± 1.0 ka, based on the correlative radiocarbon dated surfaces at Subei. Comparison of rates determined from the fill abandonment, strath emplacement, and strath abandonment models. The strath abandonment estimates are unrealistically high for the fill terrace and are not allowed by the overall Indo-Asian deformation budget. The fill emplacement estimates are lower bounds for the strath terraces.

[52] At the Aksay site, the 225 ± 10 m offset of the western T3/T2′ riser of the old Aksay fan must postdate the formation of that riser (Figure 5). Assuming this riser to have been cut by R2 in the early stages of emplacement of T2′-T2 (13.9 ± 0.9 ka), we obtain a Holocene slip rate of 16.2 ± 1.3 mm/yr (Table 5). Similarly, the 210 ± 20 m offset of the outer riser along the west side of R1 would yield a rate of 15.1 ± 1.7 mm/yr. The corresponding east bank offsets for both R1 and R2 (185 ± 20 and 220 ± 20 m, yield lower rates (13.3 ± 1.7 and 15.8 ± 3.1 mm/yr), as expected from the tendency of the right banks to be more degraded by left lateral motion. The strath abandonment model for these offsets yields slip rates of 25.0 ± 3.0, 23.3 ± 3.4, 20.6 ± 3.2 and 24.4 ± 5.2 mm/yr (Table 5), assuming that T2′ was abandoned 9.0 ± 1.0 ka. The 195 ± 20 m offset of the Sa3 channel (Figure 6), which incises both T2 and T2′, yields a minimum rate of 14.0 ± 1.7 ka using the emplacement age of T2′ at 13.9 ± 0.9 ka. Similarly, the 220 ± 20 m offset of Sa5-Sa4′, which postdates the emplacement of T2′, results in a rate of 15.8 ± 1.8 mm/yr. The 145 ± 10 m offset of the T1-filled channel of Sa1 postdates the abandonment of T2 at 6.5 ± 0.8 ka (Figures 6–11), which yields a rate of 22.3 ± 3.1 mm/yr. Here, the strath abandonment model using the age of T1 at 2.2 ± 0.2 ka would yield an unrealistically high rate of 65.6 ± 7.5 mm/yr, as expected since T1 is a fill terrace. The 135 ± 10 m offset of the channel Sa2 postdates the abandonment of T2 at 6.5 ± 0.8 ka, yielding a rate of 20.8 ± 3 ka. The differences in the emplacement/abandonment models is well illustrated by the rate obtained from the 165 ± 20 m T2′/T2 offset on the left bank of Sa1 (Figure 6). The models associating the offset with the abandonment of T2′ at 9.0 ± 1.0 ka or alternatively with the emplacement age of T2′ at 13.9 ± 0.9 ka, yield rates of 18.3 ± 3.0 mm/yr and 11.9 ± 1.6 mm/yr, respectively. Since we assume T2′ abandonment and T2 emplacement to be the same the strath emplacement model also yields 18.3 ± 3.0 mm/yr. The strath abandonment model, using the 6.5 ± 0.8 ka abandonment age of T2, yields a rate of 25.4 ± 4.4 mm/yr. Finally, the smaller, 45 ± 5 m and 40 ± 5 m dogleg offsets of the present-day channels of both Sa1 and Sa2 postdate the incision of those channels into T1, hence the abandonment of its surface 2.2 ± 0.2 ka. This implies a late Holocene slip rates of 20.5 ± 2.9 and 18.2 ± 2.8 mm/yr, respectively. At a more speculative level, if the minimum separation (1350 ± 100 m) between the easternmost T4 hill north of the fault and the remaining, high T4 surfaces south of the fault on the left bank of R1 (Figure 6) had accrued in ∼65,000 years (inferred maximum age of T4), the corresponding slip rate since the end of marine isotope stage 4 would be on order of 21 mm/yr.

[53] At Huermo Bulak. the largest offsets of the T3/T2′-T2 riser by the ATF and F2 (225 ± 20 and 50 ± 5 m, respectively, Figures 12 and 15) must postdate the abandonment of T3 (37.9 ± 2.8 ka). This yields conservative

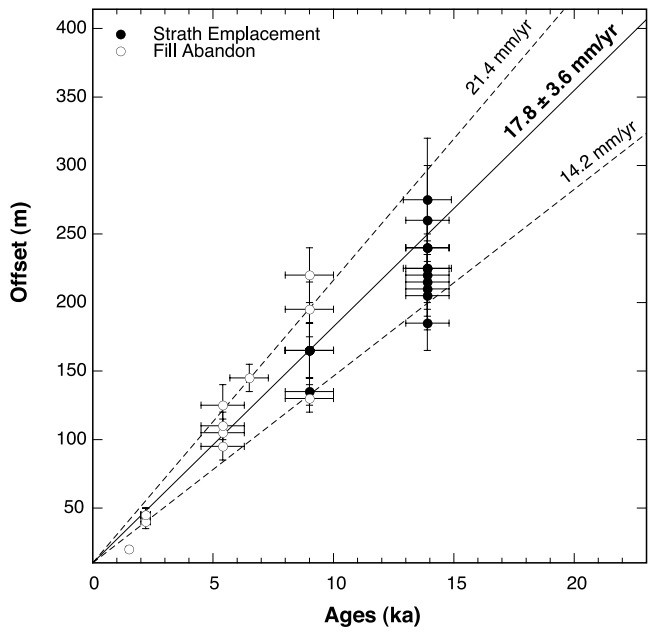

Figure 28. Summary of Holocene left-slip rate deduced from cosmogenic and ^{14}C dating of alluvial fans at three sites along the Aksay segment of the North Altyn Tagh fault. Rates derived from the fill abandonment models and strath emplacement models yield an average rate of 17.8 ± 3.6 mm/yr (±1σ) (bold values in Table 5).

Table 6. Comparison of Slip Rates From Different Offset-Age Models and T2′-T2 Ages

	Offset-Age Model								
T2′-T2 Age, ka	T2 Emplacement at Bang Guo Ba, ka	Strath Abandonment		Strath Emplacement		Fill Abandonment		All Rates	
		Rate, mm/yr	N	Rate, mm/yr	N	Rate, mm/yr	N	Rate, mm/yr	N
9.0 ± 1.0	10.2 ± 1.3	34.4 ± 13.4	21	22.0 ± 7.1	21	14.2 ± 7.1	34	23.5 ± 10.2	76
9.0 ± 1.0	13.9 ± 0.9	34.4 ± 13.4	21	20.5 ± 7.4	21	14.2 ± 7.1	34	23.0 ± 10.3	76
Unresolved	10.2 ± 1.3	40.1 ± 12.7	15	22.1 ± 7.5	13	12.9 ± 7.7	22	25.0 ± 13.8	50
Unresolved	13.9 ± 0.9	40.1 ± 12.7	15	20.3 ± 7.8	13	12.9 ± 7.7	22	24.4 ± 14.1	50

lower bounds on their slip rates (5.9 ± 0.7 and 1.3 ± 0.2 mm/yr, Table 5). The total slip rate across the two strands of the fault must therefore be greater than 7.3 ± 0.8 mm/yr. Since T2 and T2′ are strath terraces, the age of T3/T2′-T2 the riser should in fact be that of the emplacement of T2′-T2, which started here at 13.9 ± 1.0 ka. The total slip rates for the ATF and F2 is thus 19.8 ± 2.3 mm/yr for this strath emplacement scenario (Table 5). If we associate this offset with the abandonment of T2′ at 9.0 ± 1.0 ka or with the abandonment of T2 at 5.3 ± 1.0 ka, we obtain higher rates of 30.6 ± 4.4 mm/yr and 51.9 ± 10.9 mm/yr, respectively. The latter estimate, which is greater than the rate of Indo-Asian convergence is clearly unrealistic. The 105 ± 10 m offset of the T2/T1 riser by the ATF and 20 ± 5 m offset of the right bank cliff by F2 postdate the abandonment of T2 (5.3 ± 1.0 ka: the average of eight radiocarbon dates between 4.18 and 6.5 ka, Table 1). This would provide fill abandonment rate of 19.8 ± 4.2 and 3.8 ± 1.2 mm/yr, respectively (23.6 ± 5.3 mm/yr in total, Table 5). The abandonment age of the underlying T1 surface would again yield a rate in excess of 50 mm/yr for this offset and the loosely constrained emplacement age of T1 would yield a rate of 32.8 ± 4.4 mm/yr. The Sh1 (95 ± 10 m) and Sh2 (45 ± 5 m) offsets yield rates of 17.9 ± 3.9 and 20.5 ± 2.9 mm/yr, respectively, when associated with the ages of the surfaces they incise (T2 and T1). Finally, another loosely constrained rate of 27.3 ± 3.4 mm/yr may be derived from the 60 ± 5 m offset of the T1/T0″ riser by the NATF strand, assuming that T1 at Huermo Bulak was abandoned at the same time as T1 at Aksay. Overall, the total slip rates obtained at Huermo Bulak across the two strands of the North Altyn Tagh fault are compatible with those determined at Aksay. There is also another, more speculative, longer-term constraint on the slip rate. The T3′ hill isolated between the Huermo Bulak River and Sh3 north of the fault may have been displaced ~800 ± 80 m from the T3′ ridge east of the latter stream south of the fault (Figures 3 and 12). This would account for the peculiar, almond shape of this T3′ "island," which would have crossed the entire floodplain of Sh3 since 37.9–60.6 ka (the youngest and oldest samples on the T3 surface, respectively; Table 3). These ages would yield a cumulative rate of 21.1–13.2 mm/yr across the NATF and F2 strands.

[54] At Bang guo ba, the largest offset (260 ± 30 m) is that of the T3/T2′ riser on the west side of Sb1 (Figure 16). It must postdate the abandonment of T3 which is taken to have the age of the youngest ^{10}Be age, 29.2 ± 2.1 ka. This yields a minimum rate of 8.9 ± 2.1 mm/yr. The strath emplacement model of T2′ at 13.9 ± 0.9 ka yields a rate of 18.7 ± 4.5 mm/yr. Similarly, the Bang guo ba T3′-T3 prong is offset by 240 ± 20 m on either side (Figure 16), yielding a minimum rate of 8.2 ± 0.9 mm/yr with a T3 abandonment age of 29.2 ± 2.1 ka (Table 5). Since T2 and T2′ are strath terraces, the onset of emplacement of T2′ is a more appropriate age constraint. The oldest T2′–T2 ^{10}Be age at Bang guo ba being 10.2 ± 1.3 ka (AT11-E, Table 4), a rate of 23.5 ± 3.6 mm/yr is obtained. Using the emplacement age of T2′ at Aksay and Huermo Bulak, which appears to have begun at ~14 ka, would provide a more conservative rate of 17.3 ± 1.8 mm/yr (Table 5). A maximum rate of 41.1 ± 3.5 mm/yr is obtained from the abandonment of T2 (5.8 ± 0.1 ka, oldest radiocarbon age on T2, Table 5). The 215 ± 20 m offset of the T3/T2′ riser must postdate the formation of that riser. Assuming again that the emplacement of T2′ started at 13.9 ± 0.9 ka, the strath emplacement model would yield a rate of 15.5 ± 1.8 mm/yr while the strath abandonment model would result in 21.1 ± 3.2 mm/yr using the oldest ^{10}Be age on T2 (10.2 ± 1.3 ka). A minimum bound of 7.0 ± 0.9 mm/yr is obtained using the abandonment age of T3 at 29.2 ± 2.1 ka. For the three 165 ± 20 m offsets involving the T2′/T2 riser, rates from the strath emplacement and *fill abandonment* models depend upon the timing of T2′ abandonment and the onset of T2 emplacement. If, as discussed above, the abandonment of T2′ and beginning of T2 emplacement took place at 9.0 ± 1.0 ka, then the rate for both models is 18.3 ± 3.0 mm/yr. A maximum rate of 28.4 ± 3.5 mm/yr is obtained from the abandonment of T2 at 5.8 ± 0.1 ka. The 20 ± 2 m offsets of risers cut into T1 at Bang guo ba and the three concordant ^{14}C ages found in its deposits (1475 ± 60 years B.P.) are consistent with a minimum slip rate of 13.6 ± 1.5 mm/yr. Since T2 is at the same elevation on either bank of the Bang guo ba river, its abandonment age (taken as the oldest ^{14}C sample, BGB98-6, 5.76 ± 0.1 ka B.P.) and the 36 ± 3 m offset of the right bank cliff yield a conservative lower bound on the slip rate (6.3 ± 0.5 mm/yr, Figure 17). More likely, however, the age of this offset is close to that of the T1 or T0″ terrace ledges (2 ka?) preserved downstream from the fault (Figure 16), which would imply a slip rate comparable to those constrained with more abundant measurements at Aksay or Huermo Bulak (~18 mm/yr). In any case, efficient right bank lateral cutting by the river at the base of the cliff insures that the rate derived from the age of T2 is a minimum.

[55] Overall, the rates determined via the strath abandonment model are much higher than those from either the strath emplacement or fill channel models (Figure 27 and Table 5). Strath emplacement model estimates in excess of 40 mm/yr are observed where the underlying level is a fill terrace or where the emplacement/abandonment timing of the underlying level is unresolved (Table 5). Such maximum slip rate estimates greatly exceed estimates of the slip

rate derived from all other studies near this longitude [*Bendick et al.*, 2000; *Chen et al.*, 2000; *Ge et al.*, 1992; *Meyer et al.*, 1998, 1996; *Van der Woerd et al.*, 2002b]. Moreover, these implausibly high values are incompatible with Asian deformation budgets [e.g., *Avouac and Tapponnier*, 1993; *England and Molnar*, 1997a; *Peltzer and Saucier*, 1996] whether based on NUVEL-1 [*DeMets et al.*, 1990] or more recent GPS studies [*Wang et al.*, 2001]. They are informative, however, because they illustrate the caution one should exercise in pairing terrace ages and offsets to constrain rates. Clearly, the fill abandonment estimates are more relevant. The rates determined from the strath emplacement or fill abandonment models are in reasonable agreement (bold numbers in Table 5 and Figure 28). For instance, for the population of selected rates obtained by assuming that (1) T2′ was abandoned and T2 emplacement began at 9.0 ± 1.0 ka and (2) the beginning of T2′ emplacement at Bang guo ba began at 13.9 ± 1.0 ka, the average rate from the fill abandonment model is 19.0 ± 4.6 compared to 16.8 ± 1.8 mm/yr from the strath emplacement model. Overall, selected fill abandonment and strath emplacement estimates yield an average rate of 17.8 ± 3.6 mm/yr (±1σ, Figure 28).

6. Conclusions

[56] The Aksay-Bang guo ba Holocene rate, 17.8 ± 3.6 mm/yr, is fully consistent with the long-term slip rate determined on the central ATF obtained near Tura (∼37.6°N, 86.6°E) [*Mériaux et al.*, 2004] and at Subei (∼39.5°N, 94.9°E) [*Van der Woerd et al.*, 2001]. Near Tura, fluvial and glacial features have been dated to obtain a rate of 26.9 ± 6.9 mm/yr integrated over the last ∼120,000 years for offsets as large as ∼3.5 km [*Mériaux et al.*, 2004]. Near Subei, north of the junction with the Tanghenan Shan thrust, the northern Altyn Tagh fault cuts a perched, narrow terrace tongue (Lou Zhao Wan) emplaced by the Tanghe river [*Van der Woerd et al.*, 2001]. The minimum offset (113 ± 7 m) and maximum ^{14}C age (14690 ± 200 years B.P.) of that terrace preclude a rate smaller than 7.5 ± 0.2 mm/yr, with the most likely value of the slip rate being between 9 and 13 mm/yr. To obtain the rate at Aksay, the shortening rate on the Tanghenan thrust (4 to 7 mm/yr [*Van der Woerd et al.*, 2001]) which merges almost orthogonally with the NATF south of the Tang He, must be added to the left-slip rate at Lou Zhao Wan, yielding a minimum of 11.5 mm/yr and likely values between 13 and 20 mm/yr. Together, these three rate determinations support the inference of a northeastward decrease in the ATF slip rate, as proposed by *Meyer et al.* [1998].

[57] The millennial slip rate presented here is consistent with the higher range of geologic estimates of the rate along the eastern ATF. Near Subei for instance, magnetostratigraphic and structural data constrain rotation and folding to postdate ∼20 Ma, and much of the fast shortening across thrusts connected to the ATF may be younger than 6 Ma [*Gilder et al.*, 2001; *Van der Woerd et al.*, 2001]. Paleomagnetic constraints from sites along the ATF, Qaidam and Tarim basins indicate that 500 ± 130 km of displacement has accumulated along the ATF since 24 Ma, yielding a rate of ∼20 mm/yr [*Chen et al.*, 2002]. Similarly, West of Mangnai (∼90.16°E, Figure 1), *Yue et al.* [2001] tentatively reconstructed the offsets of the Xorkol basin (91°–92°E) north of the ATF and of its inferred Oligocene-post-early Miocene source region to the south, obtaining values of ∼380 and 300 km, implying a long-term slip rates of 12–16 mm/yr, in rough agreement with the late Pleistocene-Holocene rate we find at Aksay. More recently, however, on the basis of dating of detrital zircons from Miocene conglomerates in the Xorkol basin and their presumed source rocks in the Qilian Shan and northern Qaidam regions south of the fault, these authors reduced their slip rate estimate to ∼10 mm/yr (165 km/16.4 Ma) [*Yue et al.*, 2004]. Some of the disparity between long-term geologic rates determined from stratigraphic and paleomagnetic methods could be resolved if the age constraints represented maximum ages. In this connection, on the basis of detailed oil company well logs, *Métivier et al.* [1998] have linked sedimentation patterns in the Qaidam and Hexi Corridor to the eastward propagation of the ATF and concluded that the eastern terminus of the ATF did not reach the longitude of the eastern Qaidam Basin until ∼10 Ma. Uplift along the ATF and active thrusting in the Qilian Shan then closed the Qaidam to sediment discharge, producing a sharp increase in sedimentation rate within this Basin in the lower Pliocene. This would imply that a much younger age might be associated with Yue *et al*'s offsets, making the 10–16 mm/yr geological rate they propose a minimum.

[58] To first order, our morphological slip rate at Aksay is compatible with the loosely constrained 1–2 cm/yr rate inferred from the trenches studies on the Xorkol-Lapei Quan segment of the Altyn Tagh fault [*Washburn et al.*, 2003, 2001] (Figure 1). On the other hand, neither the results derived from our quantitative study of geomorphic offsets between Aksay and Bang guo ba, nor those obtained, near Subei or Tura are easy to reconcile with kinematic evidence emerging from GPS studies. Among ongoing studies by several groups [e.g., *Chen et al.*, 2000; *Wang et al.*, 2001], the two that bear the closest relevance to the area of interest here and are based on the densest number of stations, are that by *Bendick et al.* [2000] and *Shen et al.* [2001a, 2001b]. The results of the former, local study, derived from two epoch surveys of a profile across the fault at 90°E suggest a decadal slip rate, ∼400 km west of Aksay, on order of 9 ± 3 mm/yr. The latter study, based on a regional array of stations encompassing the south central edge of the Tarim basin and the Qiman-Qaidam-Qilian Shan region, also points to a current sinistral slip rate as small as 9 ± 2 mm/yr. Both values lie outside the most likely range of 14–21 mm/yr suggested by our multimillennial data. This discrepancy is aggravated by the fact that our measurements concern only the northern branch of the Altyn Tagh fault and that the GPS rates include the sum of slip on both the NATF and SATF, whose trace south of the Dangjin Shankou range at the longitude of Aksay is well expressed in the late Quaternary morphology, even if not as prominent as that of the NATF. Thus, to the 17.8 ± 3.6 mm/yr Aksay-Bang guo ba rate, one should surely add a few millimeters per year for full comparison with GPS results.

[59] At this stage, we are at a loss to offer a satisfactory explanation for the discrepancy between GPS and morphochronology. Significant errors on the ages of the offset features seem unlikely because we obtained numerous concordant ages with different techniques (^{14}C, ^{10}Be, and

^{26}Al cosmogenic exposure ages) all of them consistent with climate change. Similarly, systematic mistakes in our mapping is unlikely considering the combined used of total station profiles, topographic maps, SPOT and Corona satellite images and field mapping analysis. We note on the other hand that outside *Bendick et al.*'s [2000] profile, there are still very few GPS stations along the ATF and that they rarely face one another across the fault [*Shen et al.*, 2001a, 2001b]. Also, the occurrence, in 1997 and 2001, of two great earthquakes (Manyi and Kokoxili events) on the Kunlun fault [*Lin et al.*, 2002; *Peltzer et al.*, 1999; *Van der Woerd et al.*, 2002a; *Xu et al.*, 2002], only a few hundreds kilometers south of the Altyn Tagh, makes matters more complicated [*Wallace et al.*, 2003]. Surely, more measurement epochs, denser station arrays, and an increasing number of continuous GPS stations will improve the determination of regional GPS motions and constrain better the reference frames in which they are analyzed. Perhaps such improvement will lead to GPS decadal rates in better agreement with the geomorphically derived millennial rates we find. If not, then the possibility that slip rates on large, interacting fault systems vary on decadal, centennial or even millennial timescales, due to elastic strain storage in the continental lithosphere, should seriously be considered, as already suggested westward on the ATF [*Mériaux et al.*, 2004] and elsewhere, notably in California [*Peltzer et al.*, 2001]. For now, we simply take our results to indicate that the Altyn Tagh fault system near Aksay slips at a long-term rate of at least 14 and at most 21 mm/yr, absorbing the largest share of India's convergence relative to stable Asia after the Himalaya Frontal Thrust, even as far as 94°E longitude. If borne out by further results, this rate would indicate that the Altyn Tagh fault is little different from a plate boundary and that viscous, diffuse flow of the lower crust and lithospheric upper mantle is not the most appropriate model to describe the deformation of central and eastern Asia.

Appendix A: Cosmogenic and Radiocarbon Dating Procedures

[60] The timing of terrace abandonment was determined by and ^{10}Be and ^{26}Al cosmic ray surface exposure dating of both subsurface and partially embedded, surface quartz cobbles (Tables 2, 3, and 4, Figures 6, 12, and 16) and by radiocarbon dating (Table 1). All of the isotopic measurements, ^{14}C, ^{10}Be, and ^{26}Al, were made at the Center for Accelerator Mass Spectrometry at Lawrence Livermore National Laboratory. The chemical separation methods for Be and Al follow *Kohl and Nishiizumi* [1992] and the radiocarbon data are calibrated after *Stuiver et al.* [1998].

[61] Model ages for ^{1B}Be and ^{26}Al were calculated using the following expression in which the concentration of the nuclide, N, is a function of the nuclide production rate at the surface, P_0, exposure time, t, depth below the surface, z, the decay constant (for radionuclides), λ, and the erosion rate, ε [*Lal*, 1991]:

$$N(z,t) = \frac{P_0 e^{-\rho z/\Lambda}}{\lambda + \rho\varepsilon/\Lambda}\left(1 - e^{-(\lambda+\rho\varepsilon/\Lambda)t}\right) \quad \text{(A1)}$$

where Λ is the absorption mean free path, and ρ the material density. For surface samples ($z = 0$) experiencing negligible erosion ($\varepsilon = 0$) this reduces to

$$N(0,t) = (P_0/\lambda)\left(1 - e^{-\lambda t}\right) \quad \text{(A2)}$$

[62] The ^{10}Be and ^{26}Al production rates are based on the work by *Nishiizumi et al.* [1989] recalculated with the revised 13,000 year glacial retreat ages [*Clark et al.*, 1995] and rescaled for geodetic latitude using the correction factors of *Lal* [1991]. Production rates were further modified to include the effects of a reduced muonogenic contribution of ~3%, and a spallogenic contribution of 97% at sea level high latitude (SLHL) as described by *Owen et al.* [2002]. Uncertainties on the concentrations include those from the procedural blank, carrier composition, and counting statistics. Errors on the model ages are calculated propagating the analytical uncertainties together with a 6% error on the production rates [*Stone*, 2000] and 3.3% and 2.8% uncertainties for the decay constants of ^{10}Be and ^{26}Al, respectively [*Gosse and Phillips*, 2001]. To account for the decreased production rates at depth, the ages of subsurface samples are "depth-corrected" using equation (A1) and a density of $\rho = 2.1$ g/cm^3 and an attenuation length of $\Lambda = 175$ g/cm^2. Errors are calculated as above and include additional uncertainties in density and attenuation length of 10%.

[63] **Acknowledgments.** This work was performed under the auspices of the U.S. Department of Energy by University of California Lawrence Livermore National Laboratory under contract W-7405-Eng-48 under the sponsorship of the Laboratory Directed Research and Development program. We benefited from 4 years of financial and logistical support from Institut National des Sciences de l'Univers, Centre National de la Recherche Scientifique (Paris, France), through programs IDYL and IT, and from the China Seismological Bureau and the Ministry of Lands and Resources (Beijing, China). We thank F. Métivier and C. Lasserre for their field assistance. We are grateful to Anne-Claire Morillon for her help with the digitalization of the 1/50,000 topographic Chinese map of Aksay. We appreciate constructive comments by Lewis Owen, an anonymous reviewer, and the Associate Editor Jean Braun. This is IPGP contribution 2050 and University of California UCRL-JRNL-204490.

References

Anderson, R. S., J. L. Repka, and G. S. Dick (1996), Explicit treatment of inheritance in dating depositional surfaces using in situ ^{10}Be and ^{26}Al, *Geology*, *24*(1), 47–51.

Avouac, J. P., and P. Tapponnier (1993), Kinematic model of active deformation in central Asia, *Geophys. Res. Lett.*, *20*(10), 895–898.

Avouac, J. P., P. Tapponnier, M. Bai, H. You, and G. Wang (1993), Active thrusting and folding along the northern Tien-Shan and Late Cenozoic rotation of the Tarim relative to Dzungaria and Kazakhstan, *J. Geophys. Res.*, *98*(B4), 6755–6804.

Ballantyne, C. K. (2002), Paraglacial geomorphology, *Quat. Sci. Rev.*, *21*(18–19), 1935–2017.

Barnard, P. L., L. A. Owen, and R. C. Finkel (2004a), Style and timing of glacial and paraglacial sedimentation in a monsoon-influenced high Himalayan environment, the upper Bhagirathi Valley, Garhwal Himalaya, *Sediment. Geol.*, *165*(3–4), 199–221.

Barnard, P. L., L. A. Owen, M. C. Sharma, and R. C. Finkel (2004b), Late Quaternary (Holocene) landscape evolution of a monsoon-influenced high Himalayan valley, Gori Ganga, Nanda Devi, NE Garhwal, *Geomorphology*, *61*(1–2), 91–110.

Bendick, R., R. Bilham, J. Freymueller, K. Larson, and G. H. Yin (2000), Geodetic evidence for a low slip rate in the Altyn Tagh fault system, *Nature*, *404*(6773), 69–72.

Brown, E. T., R. Bendick, D. L. Bourlès, V. Gaur, P. Molnar, G. M. Raisbeck, and F. Yiou (2002), Slip rates of the Karakorum fault, Ladakh,

India, determined using cosmic ray exposure dating of debris flows and moraines, *J. Geophys. Res.*, *107*(B9), 2192, doi:10.1029/2000JB000100.
Brown, E. T., R. Bendick, D. L. Bourles, V. Gaur, P. Molnar, G. M. Raisbeck, and F. Yiou (2003), Early Holocene climate recorded in geomorphological features in western Tibet, *Palaeogeogr. Palaeoclimat. Palaeoecol.*, *199*(1–2), 141–151.
Bull, W. B. (1991), *Geomorphic Responses to Climatic Change*, 326 pp., Oxford Univ. Press, New York.
Chen, Y., S. Gilder, N. Halim, J. P. Cogné, and V. Courtillot (2002), New paleomagnetic constraints on central Asian kinematics: Displacement along the Altyn Tagh fault and rotation of the Qaidam Basin, *Tectonics*, *21*(5), 1042, doi:10.1029/2001TC901030.
Chen, Z., B. C. Burchfiel, Y. Liu, R. W. King, L. H. Royden, W. Tang, E. Wang, J. Zhao, and X. Zhang (2000), Global Positioning System measurements from eastern Tibet and their implications for India/Eurasia intercontinental deformation, *J. Geophys. Res.*, *105*(B7), 16,215–16,227.
Clark, D. H., P. R. Bierman, and P. Larsen (1995), Improving in situ cosmogenic chronometers, *Quat. Res.*, *44*, 367–377.
DeMets, C., R. G. Gordon, D. F. Argus, and S. Stein (1990), Current plate motions, *Geophys. J. Int.*, *101*(2), 425–478.
Ding, G., J. Chen, Q. Tian, X. Shen, C. Xing, and K. Wei (2004), Active faults and magnitudes of left-lateral displacement along the northern margin of the Tibetan Plateau, *Tectonophysics*, *380*(3–4), 243–260.
England, P., and G. Houseman (1986), Finite strain calculations of continental deformation: 2. Comparison with the India-Asia collision zone, *J. Geophys. Res.*, *91*(B3), 3664–3676.
England, P., and P. Molnar (1997a), Active deformation of Asia: From kinematics to dynamics, *Science*, *278*(5338), 647–650.
England, P., and P. Molnar (1997b), The field of crustal velocity in Asia calculated from Quaternary rates of slip on faults, *Geophys. J. Int.*, *130*(3), 551–582.
Gasse, F., et al. (1991), A 13,000-year climate record from western Tibet, *Nature*, *353*(6346), 742–745.
Gaudemer, Y., P. Tapponnier, B. Meyer, G. Peltzer, S. M. Guo, Z. T. Chen, H. G. Dai, and I. Cifuentes (1995), Partitioning of crustal slip between linked, active faults in the eastern Qilian Shan, and evidence for a major seismic gap, the Tianzhu gap, on the western Haiyuan fault, Gansu (China), *Geophys. J. Int.*, *120*(3), 599–645.
Ge, S., G. Shen, R. Wei, G. Ding, and Y. Wang (1992), *Active Altun Fault Zone*, 319 pp., State Seismol. Bur. of China, Beijing.
Gilder, S., Y. Chen, and S. Sen (2001), Oligo-Miocene stratigraphy and rock magnetism of the Xishuigou section, Subei (Gansu Province, western China), *J. Geophys. Res.*, *106*(B12), 30,505–30,521.
Gosse, J. C., and F. M. Phillips (2001), Terrestrial in situ cosmogenic nuclides: Theory and application, *Quat. Sci. Rev.*, *20*(14), 1475–1560.
Hancock, G. S., R. S. Anderson, O. A. Chadwick, and R. C. Finkel (1999), Dating fluvial terraces with Be-10 and Al-26 profiles: Application to the Wind River, Wyoming, *Geomorphology*, *27*(1–2), 41–60.
Holt, W. E. (2000), Correlated crust and mantle strain fields in Tibet, *Geology*, *28*(1), 67–70.
Holt, W. E., N. Chamot-Rooke, X. Le Pichon, A. J. Haines, B. Shen-Tu, and J. Ren (2000), Velocity field in Asia inferred from Quaternary fault slip rates and Global Positioning System observations, *J. Geophys. Res.*, *105*(B8), 19,185–19,209.
Houseman, G., and P. England (1986), Finite strain calculations of continental deformation: 1. Method and general results for convergent zones, *J. Geophys. Res.*, *91*(B3), 3651–3663.
Hubert-Ferrari, A., G. King, I. Manighetti, R. Armijo, B. Meyer, and P. Tapponnier (2003), Long-term elasticity in the continental lithosphere; modelling the Aden Ridge propagation and the Anatolian extrusion process, *Geophys. J. Int.*, *153*(1), 111–132.
Kohl, C. P., and K. Nishiizumi (1992), Chemical isolation of quartz for measurement of in situ-produced cosmogenic nuclides, *Geochim. Cosmochim. Acta*, *56*(9), 3583–3587.
Lal, D. (1991), Cosmic ray labeling of erosion surfaces: In situ production rates and erosion models, *Earth Planet. Sci. Lett.*, *104*, 424–439.
Lasserre, C., et al. (1999), Postglacial left slip rate and past occurrence of $M \geq 8$ earthquakes on the western Haiyuan fault, Gansu, China, *J. Geophys. Res.*, *104*(B8), 17,633–17,652.
Lasserre, C., Y. Gaudemer, P. Tapponnier, A.-S. Mériaux, J. Van der Woerd, Y. Daoyang, F. J. Ryerson, R. C. Finkel, and M. W. Caffee (2002), Fast late Pleistocene slip rate on the Leng Long Ling segment of the Haiyuan fault, Qinghai, China, *J. Geophys. Res.*, *107*(B11), 2276, doi:10.1029/2000JB000060.
Lin, A. M., B. H. Fu, J. M. Guo, Q. L. Zeng, G. M. Dang, W. G. He, and Y. Zhao (2002), Co-seismic strike-stip and rupture length produced by the 2001 M_s 8. 1 central Kunlun earthquake, *Science*, *296*(5575), 2015–2017.
Mériaux, A.-S., F. J. Ryerson, P. Tapponnier, J. Van der Woerd, R. C. Finkel, X. Xu, Z. Xu, and M. W. Caffee (2004), Rapid slip along the central Altyn Tagh Fault: Morphochronologic evidence from Cherchen He and Sulamu Tagh, *J. Geophys. Res.*, *109*, B06401, doi:10.1029/2003JB002558.
Métivier, F., Y. Gaudemer, P. Tapponnier, and B. Meyer (1998), Northeastward growth of the Tibet plateau deduced from balanced reconstruction of two depositional areas: The Qaidam and Hexi Corridor basins, China, *Tectonics*, *17*(6), 823–842.
Meyer, B., P. Tapponnier, Y. Gaudemer, G. Peltzer, S. M. Guo, and Z. T. Chen (1996), Rate of left-lateral movement along the easternmost segment of the Altyn Tagh fault, east of 96°E (China), *Geophys. J. Int.*, *124*(1), 29–44.
Meyer, B., P. Tapponnier, L. Bourjot, F. Metivier, Y. Gaudemer, G. Peltzer, G. Shunmin, and C. Zhitai (1998), Crustal thickening in Gansu-Qinghai, lithospheric mantle subduction, and oblique, strike-slip controlled growth of the Tibet Plateau, *Geophy. J. Int.*, *135*(1), 1–47.
Molnar, P., et al. (1994), Quaternary climate-change and the formation of river terraces across growing anticlines on the north flank of the Tien-Shan, China, *J. Geol.*, *102*(5), 583–602.
Nishiizumi, K., E. L. Winterer, C. P. Kohl, J. Klein, R. Middleton, D. Lal, and J. R. Arnold (1989), Cosmic ray production rates of ^{10}Be and ^{26}Al in quartz from glacially polished rocks, *J. Geophys. Res.*, *94*(B12), 17,907–17,915.
Owen, L. A., R. C. Finkel, M. W. Caffee, and L. Gualtieri (2002), Timing of multiple late Quaternary glaciations in the Hunza Valley, Karakoram Mountains, northern Pakistan: Defined by cosmogenic radionuclide dating of moraines, *Geol. Soc. Am. Bull.*, *114*(5), 593–604.
Peltzer, G., and F. Saucier (1996), Present-day kinematics of Asia derived from geologic fault rates, *J. Geophys. Res.*, *101*(B12), 27,943–27,956.
Peltzer, G., and P. Tapponnier (1988), Formation and evolution of strike-slip faults, rifts, and basins during the India-Asia collision: An experimental approach, *J. Geophys. Res.*, *93*(B12), 15,085–15,117.
Peltzer, G., P. Tapponnier, Y. Gaudemer, B. Meyer, S. M. Guo, K. L. Yin, Z. T. Chen, and H. G. Dai (1988), Offsets of late Quaternary morphology, rate of slip, and recurrence of large earthquakes on the Chang Ma fault (Gansu, China), *J. Geophys. Res.*, *93*(B7), 7793–7812.
Peltzer, G., P. Tapponnier, and R. Armijo (1989), Magnitude of late Quaternary left-lateral displacements along the north edge of Tibet, *Science*, *246*, 1285–1289.
Peltzer, G., F. Crampe, and G. King (1999), Evidence of nonlinear elasticity of the crust from the M_w 7.6 Manyi (Tibet) earthquake, *Science*, *286*(5438), 272–276.
Peltzer, G., F. Crampe, S. Hensley, and P. Rosen (2001), Transient strain accumulation and fault interaction in the eastern California shear zone, *Geology*, *29*(11), 975–978.
Repka, J. L., R. S. Anderson, and R. C. Finkel (1997), Cosmogenic dating of fluvial terraces, Fremont River, Utah, *Earth Planet. Sci. Lett.*, *152*(1–4), 59–73.
Ritz, J.-F., E. T. Brown, D. L. Bourlès, H. Philip, A. Schlupp, G. M. Raisbeck, F. Yiou, and B. Enkhtuvshin (1995), Slip rates along active faults estimated with cosmic-ray-exposure dates: Application to the Bogd fault, Gobi-Altaï, Mongolia, *Geology*, *23*(11), 1019–1022.
Ritz, J.-F., et al. (2003), Late Pleistocene to Holocene slip rates for the Gurvan Bulag thrust fault (Gobi-Altay, Mongolia) estimated with ^{10}Be dates, *J. Geophys. Res.*, *108*(B3), 2162, doi:10.1029/2001JB000553.
Ritts, B. D., and U. Biffi (2000), Magnitude of post-Middle Jurassic (Bajocian) displacement on the Altyn Tagh fault, NW China, *Geol. Soc. Am. Bull.*, *112*, 61–74.
Roger, F., P. Tapponnier, N. Arnaud, U. Scharer, M. Brunel, Z. Q. Xu, and J. S. Yang (2000), An Eocene magmatic belt across central Tibet: Mantle subduction triggered by the Indian collision?, *Terra Nova*, *12*(3), 102–108.
Ryerson, F. J., G. Peltzer, P. Tapponnier, R. C. Finkel, A.-S. Meriaux, and J. V. d. Woerd (1999), Active slip-rates on the Altyn Tagh fault–Karakax Valley segment: Constraints from surface exposure dating, *Eos Trans. AGU*, *80*(46), Fall Meet. Suppl, F1137.
Shen, F., L. H. Royden, and B. C. Burchfiel (2001a), Large-scale crustal deformation of the Tibetan Plateau, *J. Geophys. Res.*, *106*(B4), 6793–6816.
Shen, Z. K., M. Wang, Y. X. Li, D. D. Jackson, A. Yin, D. N. Dong, and P. Fang (2001b), Crustal deformation along the Altyn Tagh fault system, western China, from GPS, *J. Geophys. Res.*, *106*(B12), 30,607–30,621.
Siame, L. L., D. L. Bourles, M. Sebrier, O. Bellier, J. C. Castano, M. Araujo, M. Perez, G. M. Raisbeck, and F. Yiou (1997), Cosmogenic dating ranging from 20 to 700 ka of a series of alluvial fan surfaces affected by the El Tigre fault, Argentina, *Geology*, *25*(11), 975–978.
Sieh, K. E., and R. H. Jahns (1984), Holocene activity of the San Andreas fault at Wallace Creek, California, *Geol. Soc. Am. Bull.*, *95*(8), 883–896.
Stone, J. O. (2000), Air pressure and cosmogenic isotope production, *J. Geophys. Res.*, *105*(B10), 23,753–23,759.

Stuiver, M., P. J. Reimer, E. Bard, J. W. Beck, G. S. Burr, K. A. Hughen, B. Kromer, G. McCormac, J. van der Plicht, and M. Spurk (1998), INTCAL98 Radiocarbon Age Calibration, 24,000–0 cal BP, *Radiocarbon*, *40*(3), 1041–1084.

Tapponnier, P., and P. Molnar (1977), Active faulting and tectonics in China, *J. Geophys. Res.*, *82*(20), 2905–2930.

Tapponnier, P., et al. (1990), Active thrusting and folding in the Qilian-Shan, and decoupling between upper crust and mantle in northeastern Tibet, *Earth Planet. Sci. Lett.*, *97*(3–4), 382–403.

Tapponnier, P., F. J. Ryerson, J. Van der Woerd, A. S. Meriaux, and C. Lasserre (2001a), Long-term slip rates and characteristic slip: Keys to active fault behaviour and earthquake hazard, *C. R. Acad. Sci., Ser. II*, *333*(9), 483–494.

Tapponnier, P., Z. Xu, F. Roger, B. Meyer, N. Arnaud, G. Wittlinger, and J. Yang (2001b), Oblique stepwise rise and growth of the Tibet Plateau, *Science*, *294*, 1671–1677.

Thompson, L. G., T. Yao, M. E. Davis, K. A. Henderson, E. Mosley-Thompson, P. N. Lin, J. Beer, H. A. Synal, J. ColeDai, and J. F. Bolzan (1997), Tropical climate instability: The last glacial cycle from a Qinghai-Tibetan ice core, *Science*, *276*(5320), 1821–1825.

Van der Woerd, J. W., F. J. Ryerson, P. Tapponnier, Y. Gaudemer, R. Finkel, A. S. Meriaux, M. Caffee, G. G. Zhao, and Q. L. He (1998), Holocene left-slip rate determined by cosmogenic surface dating on the Xidatan segment of the Kunlun fault (Qinghai, China), *Geology*, *26*(8), 695–698.

Van der Woerd, J., F. J. Ryerson, P. Tapponnier, A. S. Meriaux, Y. Gaudemer, B. Meyer, R. C. Finkel, M. W. Caffee, G. G. Zhao, and Z. Q. Xu (2000), Uniform slip-rate along the Kunlun fault: Implications for seismic behaviour and large-scale tectonics, *Geophys. Res. Lett.*, *27*(16), 2353–2356.

Van der Woerd, J., X. Xu, H. B. Li, P. Tapponnier, B. Meyer, F. J. Ryerson, A. S. Meriaux, and Z. Q. Xu (2001), Rapid active thrusting along the northwestern range front of the Tanghe Nan Shan (western Gansu, China), *J. Geophys. Res.*, *106*(B12), 30,475–30,504.

Van der Woerd, J., A.-S. Meriaux, Y. Klinger, F. J. Ryerson, Y. Gaudemer, and P. Tapponnier (2002a), The November 14th, 2001 M_w = 7.8 Kokoshili earthquake in northern Tibet (Qinghai Province, China), *Seismol. Res. Lett.*, *73*, 125–135.

Van der Woerd, J., P. Tapponnier, F. J. Ryerson, A. S. Meriaux, B. Meyer, Y. Gaudemer, R. C. Finkel, M. W. Caffee, G. G. Zhao, and Z. Q. Xu (2002b), Uniform postglacial slip-rate along the central 600 km of the Kunlun fault (Tibet), from Al-26, Be-10, and C-14 dating of riser offsets, and climatic origin of the regional morphology, *Geophys. J. Int.*, *148*(3), 356–388.

Wallace, K., G. Yin, and R. Bilham (2003), Further confirmation of a low slip rate on the Altyn Tagh fault, *Eos Trans. AGU*, *84*(46), Fall Meet. Suppl., Abstract T21D-480.

Wang, Q., et al. (2001), Present-day crustal deformation in China constrained by global positioning system measurements, *Science*, *294*(5542), 574–577.

Washburn, Z., J. R. Arrowsmith, S. L. Forman, E. Cowgill, X. F. Wang, Y. Q. Zhang, and Z. L. Chen (2001), Late Holocene earthquake history of the central Altyn Tagh fault, China, *Geology*, *29*(11), 1051–1054.

Washburn, Z., J. R. Arrowsmith, G. Dupont-Nivet, W. X. Feng, Z. Y. Qiao, and Z. L. Chen (2003), Paleoseismology of the Xorxol segment of the central Altyn Tagh fault, Xinjiang, China, *Ann. Geophys.*, *46*(5), 1015–1034.

Weldon, R. J., and K. E. Sieh (1985), Holocene rate of slip and tentative recurrence interval for large earthquakes on the San Andreas fault, Cajon Pass, southern California, *Geol. Soc. Am. Bull.*, *96*(6), 793–812.

Wittlinger, G., P. Tapponnier, G. Poupinet, J. Mei, S. Danian, G. Herquel, and F. Masson (1998), Tomographic evidence for localized lithospheric shear along the Altyn Tagh fault, *Science*, *282*(5386), 74–76.

Wittlinger, G., J. Vergne, P. Tapponnier, V. Farra, G. Poupinet, M. Jiang, H. Su, G. Herquel, and A. Paul (2004), Teleseismic imaging of subducting lithosphere and Moho offsets beneath western Tibet, *Earth Planet. Sci. Lett.*, *221*(1–4), 117–130.

Xu, X., W. Chen, W. Ma, G. Yu, and G. Chen (2002), Surface rupture of the Kunlunshan earthquake (Ms 8. 1), northern Tibetan Plateau, China, *Seismol. Res. Lett.*, *73*, 884–892.

Yue, Y., B. D. Ritts, S. A. Graham, J. L. Wooden, G. G. Gehrels, and Z. T. Zhang (2004), Slowing extrusion tectonics: Lowered estimate of post-early Miocene slip rate for the Altyn Tagh fault, *Earth Planet. Sci. Lett.*, *217*(1–2), 111–122.

Yue, Y. J., B. D. Ritts, and S. A. Graham (2001), Initiation and long-term slip history of the Altyn Tagh fault, *Int. Geol. Rev.*, *43*(12), 1087–1093.

M. W. Caffee, Physics Department, Purdue University, West Lafayette, IN 47907, USA.

R. C. Finkel, A.-S. Mériaux, and F. J. Ryerson, Lawrence Livermore National Laboratory, P.O. Box 808, L-206, Livermore, CA 94550, USA. (meriaux1@llnl.gov)

Li Haibing, Total Exploration China, Total-Fina-Elf, Beijing, 100004, China.

G. King and P. Tapponnier, Laboratoire de Tectonique, Mécanique de la Lithosphère, Institut de Physique du Globe de Paris, CNRS-UMR 7578, 4 place Jussieu, F-75252 Paris Cedex, France.

J. Van der Woerd, Institut de Physique du Globe de Strasbourg, CNRS-UMR 7516, 5, Rue Rene Descartes, F-67084 Strasbourg Cedex, France.

Chen Wenbin and Xu Xiwei, Institute of Geology, China Earthquake Administration, Beijing, 63 Fuxing Ave., Beijing 100036, China.

Xu Zhiqin, Institute of Geology, Ministry of Land and Resources, Baiwanzhuand Road, Beijing 100037, China.